Characterization of Energy and charge transfer processes by time resolved electronic spectroscopy.

Ph.D. Thesis in

Scienze Chimiche

Scuola di Dottorato in Scienze Chimiche (XXI ciclo)

Author:
Andrea Lapini

Tutor:
Prof. Roberto Righini

Coordinator of the Ph.D. School:
Prof. Gianni Cardini

December 2008

(CHIM02)

Contents

ACKNOWLEDGEMENTS

This PhD thesis has been realized at LENS *European Laboratory for Non Linear Spectroscopy*; I want to thank this institute and its director Prof. *Roberto Righini*.

Thankyou very much to Prof. *Roberto Righini* and Prof. *Paolo Foggi* for their help and for offering me the possibility to work at LENS.

Thanks to prof. Andrea Dei for his help, for his advices and for offering me always an objective point of view on my work.

This thesis contains *ab initio* calculations performed by DFT method. I want to dedicate this small work to the memory of Prof. Alessandro Bencini who taught me the basic strategies of this world.

Since the first moment I joined the LENS laboratory, people told me that this is a great family: they were right. So I want to thank all the *friends* of my group, because this is the right way to define them: *friends*:

Thanks to *Marco* and *Riccardo*; LENS will never have a PhD student's office as ours.

Thanks to *Laura* for the precious discussions about everything.

Thanks to *Agnese* for her patience, for the great organization's capabilities and, above all, for her friendship: you are much more than a colleague, thanks again.

Thanks to *Sandra* and *Patritia*; There are different kind of reasons to thank both of you, essentially for your true friendship.

Thanks to *Jason*: you are an amazing person, you *were* a good scientist (also if you did not think that), you will be a very good journalist and, above all, you are a true friend.

Thanks to my parents *Mario* and *Lisanna* for their support and their continuous help.

Thanks to my brother *Massimo*: there are not enough words to say how much you are important.

I want to thank *Barbara*, to whom this thesis is dedicated, who always agreed with my choices, never interposed my decisions but continuously supported my work with great patience, thanks for everything.

Chapter 1

Introduction

The Phenomena of energy and charge transfer are ubiquitous in natural and artificial photochemically active systems. Energy transfer is present in antenna systems of photosynthetic organisms, in photodynamic therapy in multichromophoric β-cyclodextrins in photomolecular devices and in photochemical synthesis. On the other hand, the charge transfer processes are the basic steps in the functionality of biological systems, in the development of photovoltaic devices and in the identification of different magnetic states of molecular and supramolecular compounds. In this framework, we developed two different field of research. On one hand we studied the energy transfer mechanism in an organic antenna model system, while on the other hand we undertook the study of the optically activated valence tautomerism in a Manganese complex.

The characterization of the energy transfer mechanism has been developed by means of static and time resolved spectroscopy. In particular, UV-Vis ground state absorption and static fluorescence measurements are extremely useful tools for the preliminary characterizations. The aim of the work was the development of a model molecular system in which we could indirectly promote a molecular reaction. For that reason, in collaboration with the organic synthesis research group of prof. Alberto Brandi and Dr. Stefano Cicchi, we begin a preliminary screening of possible donor and acceptor candidates. On the basis of canonical prerequisites that donors

and acceptors chromophores have to meet and with the precise purpose to utilize natural derivatives, the final choice fell on the Umbelliferone as donor molecule and Alizarin as acceptor compound. The Alizarin molecule was particularly indicated for our project since it is characterized by the intramolecular proton transfer reaction in the first singlet excited state. The first part of the work was dedicated to the study of the photophysical properties of the isolated donor and acceptor molecules. In particular, ground state absorption and static fluorescence experiments were utilized in conjunction with *ab initio* calculation to obtain a complete information of the energetic levels involved in the experimentally observed electronic transitions. Concerning the Alizarin molecule we performed a detailed analysis, by means of *ab initio* calculation with *Density Functional* methods, of the excited state intramolecular proton transfer reaction. At the same time transient absorption technique was employed for the characterization of excited state's dynamic. The final part was dedicated to the study of the energy transfer in the bichromophoric compound.

The study of molecular systems whose physical properties can be reversibly changed and controlled following a variation of an external parameter constitute an appealing perspective for the realization of molecular scale electronic devices.[1,2] In particular, molecules showing photoreactivity or photochromic properties are of potential interest as materials for optical data storage. Although undoubtedly attractive, the uncompleted comprehension of the factors affecting the photochromic behavior, has hampered the possibility of designing new systems following a predetermined strategy. This part of the work has been dedicated to the study of the photophysical properties of a Manganese-Dioxolene complex with time resolved spectroscopy. The synthesis and preliminary characterization was performed by prof. Andrea Dei, while transient absorption measurements were carried out with the purpose of characterize the mechanism of the valence tautomerism.

In the second chapter I will propose the fundamental concept of the femtosecond transient absorption experiment. The third chapter deals with the detailed characterization of the photophysics of the Umbelliferone (donor unit). In the fourth

chapter the Alizarin chromophore will be discuss with particular attention to the intramolecular proton transfer process, In the fifth chapter we describe the time resolved characterization of the bichromophore and, in the end, the sixth chapter is dedicated to the characterization of the Manganese-Dioxolene complex. There are also two appendixes where I give a detailed explanation of the data analysis methods for time resolved experiments and of the rotational contribution to the time resolved fluoresce and transient absorption signal.

Chapter 2

Experimental part

In this chapter we'll define the quantities measured in the transient absorption experiment. We will further discuss the effects introduced by the temporal dispersion of the spectral components of the probe pulse on the evolution of the transient spectra.

2.1 Transient Absorption Experiment

The experimental instrumentation for femtosecond time-resolved transient absorption spectroscopy has been described in detail in previous reports.[3,4] Briefly, ultrashort pulses (duration ∼100 fs at 800 nm, repetition rate 1 kHz, energy 700 μJ/pulse) are produced by a regenerative amplified Ti:Sapphire laser system. Tunable excitation pulses are obtained by means of a BBO-based optical parametric generator (OPG-OPA). In the present experiments the excitation wavelength of 325 nm was produced by the FHG (fourth harmonic generation) of the the *signal's* (1.3 μm) pulses, obtaining ∼2 mW average power. The 400 nm wavelength was obtained simply by the frequency doubling of the fundamental (800 nm) frequency by means of a BBO crystal. A small portion (2 μJ/pulse) of the 800 nm beam was focused on a 2.5 mm thick calcium fluoride plate to generate the white-light continuum used for probing. The resulting spectrally broadened laser pulse spanned the entire visible

region and extended in the near UV to roughly 350 nm. The white-light continuum was further split into two parts of equal intensity by a 50/50 fused-silica-Al beam splitter. One part, acting as a probe beam, was spatially overlapped with the excitation beam in the sample. The second part crossed the sample in a different position and always before the interaction of the pump pulse with the sample providing a convenient reference signal. Transient absorption spectra of Umbelliferone, of 2metO-1HAQ with 300 nm excitation wavelength and the spectra of the bichromophore adduct has been acquired by the help of the following detector system: the probe and reference beams were spectrally dispersed in a flat-field 25 cm Czerny-Turner spectrometer, and detected by means of a back illuminated CCD camera with spectral response in the region 300-1000 nm. The acquisition of the transient absorption signal of all the others molecular system has been performed by the help of a different detection system. In this last configuration the pump and probe beams were spectrally dispersed by a jobin-Yvon CP 140-1824 spectrometer and detected by a Hamamatsu double linear-array CCD system. The electric signals, obtained by a home made front-end circuit, were converted by the help of a simultaneous two-channels analog to digital acquisition board (ADLINK DAQ-2010). The last detection system, although characterized by a lower spectral resolution, allowed us to acquire transient spectra with an increased signal to noise ratio.

Sample's solution is usually inserted in a quartz cell (Hellma) with 2mm optical path. The irradiated volume is refreshed by stirring the sample with a micro magnet inside the 2mm cell and transient absorption spectra were recorded reducing the repetition rate from 1KHz to 100 Hz to avoid photo-damage of the sample. All the samples were prepared to have an optical density of approximately 1 at the excitation wavelength. Steady-state absorption spectra of the solutions were measured before and after the experiments to check for possible sample decomposition. All measurements were carried out at room temperature ($22 \pm 1°$).

Two different detection configurations were utilized to obtain the data sets herein presented, which are composed of both transient spectra (Absorbance of the excited

state vs. wavelength at a given pump-probe delay time) and kinetic plots (Intensity of the probe vs. delay time at a fixed wavelength).

2.1.1 Transient Transmittance

In the transient spectra, the transmittance at a given delay time t and wavelength λ, $T(t, \lambda)$, is defined as

$$T(t, \lambda) = \frac{I(t, \lambda)}{I_0(\lambda)} \tag{2.1}$$

where $I(t, \lambda)$ and $I_0(\lambda)$ are the intensities of the white-light continuum components reaching the detector having and having not interacted with the pump pulse, respectively.

In practice is not possible to substitute $I(t, \lambda)$ and $I_0(\lambda)$ with the probe and reference intensities $I_p(t, \lambda)$ and $I_r(t, \lambda)$ because the latter two beams will never have the same spectral content. To obtain the correct value of $T(t, \lambda)$ two measurements were performed: the first without the pump beam, thus acquiring the intensities of the probe $I'_p(\lambda)$ and reference pulses $I'_r(\lambda)$; the second with both excitation and probe beams, thus measuring $I''_p(t, \lambda)$ and $I''_r(\lambda)$. The transient transmittance $T(t, \lambda)$ is then given by

$$T(t, \lambda) = \frac{I''_p(t, \lambda)}{I''_r(\lambda)} * \frac{I'_r(\lambda)}{I'_p(\lambda)} = \frac{I''_p(t, \lambda)}{I'_p(\lambda)} * \frac{I'_r(\lambda)}{I''_r(\lambda)} \tag{2.2}$$

The reference pulse interacts with the sample always before the the pump pulse, hence, $I''_r(\lambda)$ and $I'_r(\lambda)$ are, neglecting little fluctuations, identical quantities and the rate $I'_r(\lambda)/I''_r(\lambda)$ is the normalization function.

When the irradiated sample shows luminescence emission, the intensity acquired by the detector system is not related only to transient phenomena. The detector system collects the light continuously and it is not able to discriminate the light pulses synchronized with the pump excitation from the delayed emissions (fluorescence and phosphorescence). Some part of *static* fluorescence emitted by the sample propagates collinearly with the probe pulse and it is acquired by the detector system, producing a transient spectrum affected by some fluorescence contribution: the

stimulated emission (whose intensity is related to the amount of excited state population and hence to the delay between the pump and probe pulse) and the static fluorescence. To avoid the *static* fluorescence contribution we performed a third acquisition step with the pump beam only. The fluorescence has different intensities on the detection surfaces of the probe and reference beams: F_r and F_s. Hence the three steps concerning the acquisition of a transient spectrum are

1. Pump **off** Probe **on**

$$\begin{cases} S_1 = I'_p(\lambda) \\ R_1 = I'_r(\lambda) \end{cases} \tag{2.3}$$

2. Pump **on** Probe **on**

$$\begin{cases} S_2 = I''_p(t,\lambda) + F_p \\ R_2 = I''_r(\lambda) + F_r \end{cases} \tag{2.4}$$

3. Pump **on** Probe **off**

$$\begin{cases} S_3 = F_p \\ R_3 = F_r \end{cases} \tag{2.5}$$

The transient transmittance, corrected for the fluorescence contribution, is obtained as

$$T(t,\lambda) = \frac{S_2 - S_3}{R_2 - R_3} * \frac{R_1}{S_1} = \frac{[I''_p(t,\lambda) + F_p] - F_p}{[I''_r(\lambda) + F_r] - F_r} * \frac{I'_r(\lambda)}{I'_p(\lambda)} = \frac{I''_p(t,\lambda)}{I'_p(\lambda)} * \frac{I'_r(\lambda)}{I''_r(\lambda)} \tag{2.6}$$

2.1.2 Single Wavelength Measurements

Recording kinetic plots requires narrow bandwidth detection. The desired wavelengths were selected by means of a 5 nm bandwidth interference filters. The intensity of the probe pulse was measured by a silicon differential photodiode and a lock-in amplifier synchronized to a chopper, switching the pump pulse on and off at half the repetition-rate of the laser system (500 Hz). In this way, the reading of the phase-locked amplifier gave the modulation of the probe pulse intensity due to the interaction with the pump pulse.

2.2 Transient Absorption Signal in the Time Domain

The transient absorption signal is proportional to the concentration of excited states which absorbs the photons of the probe beam at wavelength λ. Within the *linear response regime* the signal of a *pump & probe* experiment, in the time domain and at a wavelength λ, is given by the convolution of the *molecular response function* with the functions associated to the pump and probe pulses. If $s(t)$ is the signal, $R(t)$ is the *molecular response function*, $p_1(t)$ and $p_2(t)$ are the functions of the pump and probe pulses, then we can write

$$s(t) = R(t) \otimes p_1(t) \otimes p_2(t) \tag{2.7}$$

where $\otimes$ is the convolution operation defined as

$$a \otimes b = \int_{-\infty}^{+\infty} a(t - t')\, b(t')\, dt' \tag{2.8}$$

Equation 2.7 can be rewritten as

$$S(\tau) = \int_{-\infty}^{+\infty} \int_{-\infty}^{+\infty} p_2(t - \tau)\, p_1(t - t')\, R(t')\, dt\, dt' \tag{2.9}$$

Considering the associative properties for the convolution operation

$$(a \otimes b) \otimes c = a \otimes (b \otimes c) \tag{2.10}$$

we obtain

$$g(t) = p_1(t) \otimes p_2(t) \tag{2.11}$$

$$g(t' - \tau) = \int_{-\infty}^{+\infty} p_2(t - \tau)\, p_1(t - t')\, dt \tag{2.12}$$

The function $g(t' - \tau)$ is the *instrumental function* and, considering the convolution theorem, it is given by the *crosscorrelation function* between the pump and probe pulse. We can rewrite Equation 2.7 as

$$s(t) = R(t) \otimes p(t) \tag{2.13}$$

Hence

$$S(\tau) = \int_{-\infty}^{+\infty} g(t' - \tau)\, R(t')\, dt' \tag{2.14}$$

The *molecular response function* is generally associated with the response of the molecular system to an applied perturbation and, therefore, it contains the information about the temporal evolution of the system itself. Hence, $R(t)$ defines the evolution of the molecular property that we want measure.

Transient absorption provides information about the photophysics and the photochemistry of the sample with a temporal resolution limited by the instrumental function. In this framework let's consider the limiting cases of Equation 2.14

1. If the duration of the applied perturbation is negligible in respect to the response time of the molecular system, then the weight of the instrumental function in the description of the signal's shape will be very low. From a mathematical point of view, this condition is equivalent to substituting the instrumental function $g(t' - \tau)$ with a δ function, obtaining

   $$S(\tau) = \int_{-\infty}^{+\infty} \delta(t' - \tau)\, R(t')\, dt' = R(\tau) \tag{2.15}$$

   The acquired signal is directly the molecular response; this is the condition of maximum accuracy of the transient measure.

2. If the molecular response time is much shorter than the applied perturbation, i.e. R(t) can be approximated to a δ function, we obtain

   $$S(\tau) = \int_{-\infty}^{+\infty} g(t' - \tau)\, \delta(t')\, dt' = g(\tau) \tag{2.16}$$

   The acquired signal is then virtually undistinguishable from the instrumental function and we say that the observed dynamic is instantaneous in relation to the temporal resolution of the apparatus.

When the time constants of photophysical and photochemical processes are comparable with the instrumental function, the molecular response function can be obtained by a de-convolution operation on the acquired signal. The former operation assumes the detailed knowledge of the instrumental function's profile.

2.3 Group Velocity

The characteristics of an ultrashort light pulses can be completely described in the time domain as well as in the frequency domain.[5,6] The pulse spectral properties are directly linked to the temporal properties by the following Fourier relation[7]

$$\widetilde{E}(\omega) = \int_{-\infty}^{+\infty} E(t)\, e^{-i\omega\, t}\, dt = |\widetilde{E}(\omega)|\, e^{\,i\Phi(\omega)} \tag{2.17}$$

where the complex notation has been employed for the representation of the amplitude spectrum: $|\widetilde{E}(\omega)|$ is the amplitude and $\Phi(\omega)$ is the spectral phase. Analogously we can obtain $E(t)$ from $\widetilde{E}(\omega)$ by means of the inverse Fourier transform:

$$E(t) = \frac{1}{2\pi} \int_{-\infty}^{+\infty} \widetilde{E}(\omega)\, e^{\,i\omega\, t}\, d\omega \tag{2.18}$$

Equations 2.17 and 2.18 comprise the existence of negative frequencies which, of course, do not have any physical meaning. In this framework it's helpful to adopt the complex notation also for the electric field $E(t)$:

$$\widetilde{E}^{+}(t) = \frac{1}{2\pi} \int_{-\infty}^{+\infty} \widetilde{E}(\omega)\, e^{\,i\omega\, t}\, d\omega \tag{2.19}$$

Hence, in the frequency domain, we obtain the following power spectrum

$$\widetilde{E}^{+}(\omega) = |\widetilde{E}(\omega)|\, e^{\,i\Phi(\omega)} = \begin{cases} \widetilde{E}(\omega) & \omega \geq 0 \\ 0 & \omega \leq 0 \end{cases} \tag{2.20}$$

The complex electric field $\widetilde{E}(t)$ can be expressed as the product of the amplitude profile and the phase term; assuming that the spectrum is centered around the frequency ω_l, called the *carrier* frequency, we have

$$\widetilde{E}^{+}(t) = \frac{1}{2}\, E(t)\, e^{\,i\,(\varphi(t)+\omega_l t)} \tag{2.21}$$

The complex envelope of the electric field varies with time with the *carrier* frequency; the latter modulated by the time fluctuations of the phase term $\varphi(t)$. The

instantaneous oscillation frequency is given by the first derivative of the exponential argument of Equation 2.21:

$$\omega = \omega_l + \frac{d}{dt}\,\varphi(t) \tag{2.22}$$

If the *carrier* frequency varies with time, then the pulse is frequency modulated; this effect is called *chirping effect*.

The frequency modulation of the pulse is due to the interaction with dispersive media, such as, for example, lenses or absorption and interference filters. Usually the high frequency (low wavelength) spectral components of the pulse experiences a higher refractive index than the low frequency ones. The frequency dependence of the phase difference can be expressed by the Taylor expansion of the phase term around the *carrier* frequency ω_l:

$$\varphi(\omega) = \varphi(\omega_l) + \frac{d\,\varphi(\omega)}{d\omega}\bigg|_{\omega_l} (\omega - \omega_l) + \frac{1}{2}\,\frac{d^2\,\varphi(\omega)}{d\omega^2}\bigg|_{\omega_l} (\omega - \omega_l)^2 + \ldots \tag{2.23}$$

The first derivative of the phase-difference in respect to the frequency ω has the dimension of a time ($[sec]$) and can be expanded in Taylor series around the *carrier* frequency:

$$\tau(\omega) = \frac{d\,\varphi(\omega)}{d\omega} = \frac{d\,\varphi(\omega)}{d\omega}\bigg|_{\omega_l} + \frac{d^2\,\varphi(\omega)}{d\omega^2}\bigg|_{\omega_l} (\omega - \omega_l) + \ldots \tag{2.24}$$

The first term of Equation 2.24 is associated to a constant delay for all the pulse spectral components. The second term is related the value of the second derivative of the phase-difference in respect to the frequency and, if the value is positive, it implies a delay which linearly grows as a function of the frequency of the pulse's spectral components within the pulse envelope. This kind of pulse is called *upchirped*. The relation between the temporal profile and the spectral content of a linearly *chirped* pulse can be written as:

$$\widetilde{E}(t) = E_0\, e^{-(1+ia)(t/\tau)} \tag{2.25}$$

where

$$\tau = \sqrt{2\ln 2} \quad FWHM \tag{2.26}$$

is obtained by the Fourier relation:

$$\widetilde{E}(\omega) = K\ \exp[i\,\varphi(\omega)]\ \exp[(\omega^2\tau)/4(1+a^2)]^2 \tag{2.27}$$

where K is a constant. The profile of the spectral intensity is given by the square module of the electric field:

$$I(\omega) = K\ \exp[(\omega^2\tau)/4(1+a^2)]^4 \tag{2.28}$$

The *Full Width at Half Maximum* ($FWHM$) of the pulse, in the frequency domain, is given by

$$2\pi\Delta\nu = \frac{1}{\tau}\sqrt{8\,(1+a^2)\,ln2} \tag{2.29}$$

The product between the temporal and frequency widths $FWHM$ of the pulse is given by

$$2\pi\Delta\nu \cdot FWHM = \frac{2\,ln2}{\pi}\sqrt{1+a^2} = 0.441\sqrt{1+a^2} \tag{2.30}$$

In the limiting case of *no* frequency modulation ($a = 0$) the pulse duration and the pulse spectral width are related by a constant and the pulse is *Transform Limited*. When the pulse is affected by the *chirping* effect (positive or negative), the spectral content is enlarged and, consequently, the intensity temporal profile is broadened.

2.3.1 Group Velocity Dispersion

The propagation velocity of a pulse, whose spectral content is continuous within a given frequency range, is different from the propagation velocity of the individual monochromatic spectral components which compose the pulse itself. If we assume that the spectral content of the pulse is centered around the *carrier* frequency ω_l, then the pulse propagation velocity (called *group velocity*) is given by the first derivative of the frequency in respect to the wavevector k:

$$v_g = \left|\frac{d\omega}{dk}\right|_{\omega_l} \tag{2.31}$$

The propagation trough a dispersive medium involves a frequency dependent phase-difference of the chromatic components of the pulse itself. The effect of such phase-difference is described as *group velocity dispersion* (GVD):

$$k_l = -\frac{1}{v_g^2}\frac{dv_g}{d\omega}\bigg|_{\omega_l} \tag{2.32}$$

the dispersion parameter, k_l, is then proportional to the first derivative of the group velocity calculated on ω_l with respect to the frequency. If the spectral and temporal amplitudes of the pulse are negligible in respect to the central value of the wavevector and of the frequency, i.e. the spatial and temporal variation of the pulse is slow, and if the variation of the dielectric constant as a function of the frequency is negligible, we can rewrite the wave equation for the propagation in a dispersive medium as:

$$\frac{\partial}{\partial\zeta}\widetilde{E}(\eta,\zeta) - \frac{I}{2}K_l\frac{\partial^2}{\partial\eta^2}\widetilde{E}(\eta,\zeta) = 0 \tag{2.33}$$

where

$$\eta = t - \frac{z}{v_g} \tag{2.34}$$

This equation is valid for a wave-packet propagating in the direction $\zeta = z$ in a delayed reference system which travels at the group velocity. If the group velocity variation in respect to the frequency is negligible, the pulse profile is obviously not affected.

The solution for Equation 2.33 in the frequency domain is given by:

$$\widetilde{E}(\omega,z) = \widetilde{E}(\omega,0)\,e^{-\frac{i}{2}k_l\,\omega^2 z} \tag{2.35}$$

This means that an initially *transform limited* pulse acquires, traveling trough a dispersive media, a spectral phase which is a quadratic function of the frequency: the result is a *chirped* pulse.

2.3.2 Group Velocity Mismatch

The modification of the pulse duration due to the *chirp* effect can be minimized by a suitable choice of the optical components and avoiding the crossing of dispersive

media. Anyway, the increase of the pulse duration and, therefore, of the instrumental function (due to GVD) is negligible in respect to the effect of the *group velocity mismatch* (GVM). The "zero timing" of the experiment, i.e. the zero on the experimental temporal scale, is associated to the temporal coincidence of the pump and probe pulses and to the fact that they travel trough the sample with the same phase velocity. In practice the beams travel trough a finite thickness of dispersive materials (the sample and the cell's window) and then the above mentioned condition is verified for the whole optical path (defined by the length of the spatial overlap between the pump and the probe beam within the sample) only when the probe wavelength equals that of the pump wavelength. For probe wavelengths different from that of the pump, the temporal coincidence condition is verified only for one point of the optical path; in fact the refractive index causes a different delays at different wavelengths and then the pulses propagate with different velocity. The effect of the *group velocity mismatch* (GVM), in the time domain, is an enlargement of the instrumental function which is proportional to the difference between the pump and probe wavelength. The GVM effect can be analytically evaluated writing the relative delay between the pump and the spectral component of the probe beam as:

$$\Delta\tau(\lambda) = \frac{x}{c}\,\Delta n(\lambda) \tag{2.36}$$

where x is the position within the sample and $\Delta n(\lambda)$ is the difference between the refraction indexes experienced by the two beams.

The cross-correlation integral can be calculated by assuming a gaussian profile for the pump and probe beams, then we obtain

$$g(\tau) = \frac{c}{a\Delta n(\lambda)}\left\{ erf\left[a\left(\tau + \frac{l}{c}\,\Delta n(\lambda) \right) \right] - erf(a\,\tau) \right\} \tag{2.37}$$

where erf indicates the error function. The a constant is given by

$$a = 2\sqrt{\frac{ln2}{\Delta\tau_{pump}^2 + \Delta\tau_{probe}^2}} \tag{2.38}$$

where $\Delta\tau$ indicates the *FWHM* of the pulse. The temporal resolution of the experiment is limited not only by the duration of the pump and probe pulses, but also by the difference between their wavelength.

2.4 Instrumental Function and Group velocity Characterization

In this section we'll describe the procedure for the characterization of the spectral and temporal properties of the white pulses in conditions which are set as close as possible to those utilized in TAS experiment. A possible method is that of measuring TAS on a fast responding sample, possibly with broad transient absorption band in order to cover the spectral range of interest. However, a better suited method consists in making use of *Optically Heterodyne Detected Optically Kerr Effect* (OHD-OKE) or, to a lesser extent, of a *Stimulated Raman Gain* (SRG) experiment. These technique have the same content of information regarding the instrumental function $g(t)$ of Equation 2.12.

2.4.1 Optical Kerr Effect OHD-OKE

OKE is generally a non-resonant process, therefore one has the possibility to obtain information about dispersion, position of zero delay and cross-correlation time without the need of changing the excitation wavelength that is going to be utilized in the TAS experiment. In a transient OKE experiment an intense linearly polarized pulse (pump) induces a birefringence in an isotropic sample. A second pulse, linearly polarized at 45° in respect to the pump, probes at a delay τ the transient birefringence. The response function of the Kerr medium is due to the third order susceptibility $\chi^{(3)}$. Two major contributions to $\chi^{(3)}$ can be identified: an instantaneous contribution due to the third order electronic hyperpolarizability and a retarded one due to nuclear motions. By choosing a medium whose nuclear response is negligible or

absent the cross-correlation function between pump and probe can be measured.

From the experimental point of view, one polarizer (analyzer), crossed with respect to the probe polarization and placed immediately after the sample, is needed to measure the transient anisotropy induced by the pump pulse. The modifications applied to the transient absorption set-up are, then, limited to inserting a thin polarizer after the sample and to rotate the pump polarization to 45° with respect to the probe polarization direction, simply adjusting the universal rotator(specification). The sheet polarizer, having an extinction ratio worse than $1:10^3$, is not as efficient as the calcite polarizers usually utilized in a typical OKE experiment (extinction ratio $1:10^6$). A residual signal is hence detected through the crossed analyzer also in the absence of the pump pulse. This fields plays the role of local field that, by beating with the Kerr field on the detector, gives rise to the heterodyne detection of the signal.

The Kerr polarization is given by

$$P(t-\tau)_{KERR} = E(t-\tau)_{probe} \int_{-\infty}^{\infty} \chi(t')^{(3)}\, I(t-t')_{pump}\, dt' \tag{2.39}$$

Provided that the $\chi(t)^{(3)}$ response is instantaneous in comparison to the pulse duration (the nuclear contribution is negligible) the signal is directly proportional to the cross-correlation of the two pulses

$$\begin{aligned} S(\tau)_{OHD-OKE} &\propto \int_{-\infty}^{\infty} P(t-\tau)_{KERR} \cdot E(t-\tau)_{loc}\, dt \\ &= \int_{-\infty}^{\infty} I(t-\tau)_{probe} I(t)_{pump}\, dt \end{aligned} \tag{2.40}$$

where E_{loc} is proportional to E_{probe} as both derive from the same pulse.

The light seen by the detector is the result of three contributions

$$I(\tau) = I(\tau)_{KERR} \pm S(\tau)_{OHD-OKE} + I_{probe} \tag{2.41}$$

where the first two contributions in the r.h.s term depend respectively quadratically and linearly on the pump intensity. The sign and the weight of the second term

depend on the rotation angle, both in size and direction (clockwise or counterclockwise), of the preparing polarizer. In the present case the experiment is performed with a high and uncontrollable local field. In a typical OHD-OKE experiment the intensity of local field is about $10^{-5} - 10^{-4}$ times lower than the probe, that's to say at least an order of magnitude weaker than that of the present case. This means that in the experimental conditions described in section 2.1 there is no possibility to controlling the phase of the local field in respect to that of the OKE field: a small rotation of few degrees of the preparing polarizer is not enough to change the sign of the phase of the local field.

It has been experimentally verified that in liquids with small Kerr response and at low intensities of the pump pulses ($\leq 2\mu J$), the first contribution to the r.h.s. term of Equation 2.41 is negligible. In this conditions, introducing Equation 2.41 into Equation 2.2: it is possible to obtain the form of the Kerr signal transmitted through the analyzer:

$$T(\tau)_{KERR} \approx 1 \pm \frac{S(\tau)_{OHD-OKE}}{I_{probe}} \tag{2.42}$$

Therefore at any delay the intensity is proportional to the cross-correlation between pump and probe.

2.4.2 Stimulated Raman Gain SRG

In a Transient Stimulated Raman Gain (SRG) experiment pump and probe pulses interact via $\chi^{(3)}$ resonant at the frequency of a Raman active mode.

If ω_{pump} is the central frequency of the pump pule, components of the continuum will be amplified or absorbed (inverse Raman effect) at frequencies equal to $(\omega_{pump} - \Omega)$ and $(\omega_{pump} + \Omega)$, respectively, Ω being the frequency of a Raman active mode. In the cases of diluted solutions the signal derives only from the solvent. Strong signals mainly due to C-H stretching modes (for example cyclohexane around 3000 cm^{-1}) and to vibrational modes like C-N stretching $\sim 1500\ cm^{-1}$ (as acetonitrile) are easily observed (Figure 2.1). As in the case of OHD-OKE , by plotting the intensity of SRG

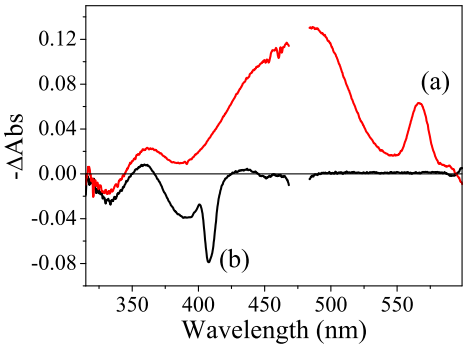

(a) (a) Stokes Stimulated Raman Gain SRG band (shift = 2932 cm^{-1}) (b) anti-Stokes Stimulated Raman Loss SRL band (shift = 3430 cm^{-1}) of water with excitation pulse at 475 nm.

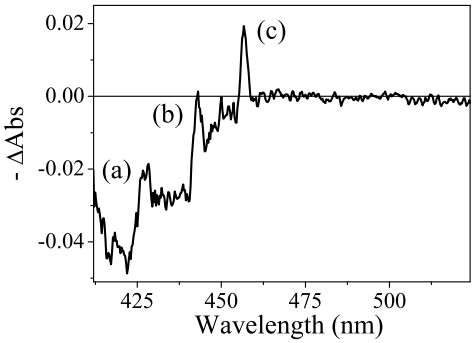

(b) Stokes Stimulated Raman Gain SRG bands of acetonitrile solution of 2metO-1HAQ with excitation pulse at 400 nm (a) shift = 1580 cm^{-1}, (b) shift = 2430 cm^{-1}, (c) shift = 3120 cm^{-1}.

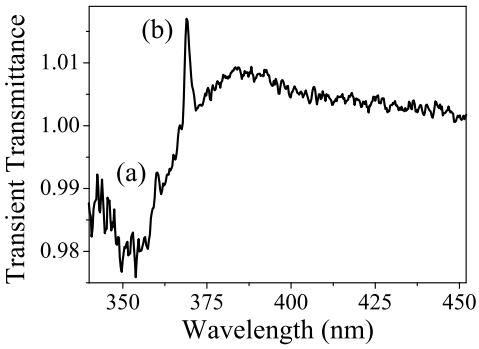

(c) Stokes Stimulated Raman Gain SRG bands of acetonitrile solution of Umbelliferone with excitation pulse at 330 nm. (a) shift = 2450 cm^{-1}, (b) shift = 3129 cm^{-1}

Figure 2.1: Stimulated Raman Scattering Band in water and acetonitrile

signal versus delay τ the cross-correlation between pump and probe is obtained (the same result is achieved if the area under the SRG band is considered). This second arrangement has the limitation that the instrumental function can be measured in a narrow spectral range in which the raman bands show-up (typically 1500-3000 cm^{-1} from ω_{pump}), i.e quite close to the excitation wavelength.

2.4.3 Characterization of the Continuum

The OHD-OKE experiment described in section 2.4.1, in which the broadband continuum acts as the probe, is utilized to measure the cross-correlation function of the apparatus at various probe wavelengths and to characterize the temporal dispersion of the probe pulse over its very broad spectral width. In fact, if the spectral components of the continuum are all coincident in time (no chirp), the Kerr or SRG signal will appear at the same time delay, whatever the probe wavelength selected. On the contrary, if a positive chirp is present, the transient signal will show up at increasingly delay with increasing probe wavelength. This effect produces an artificial time evolution of the transient spectra as shown in Figure 2.2.

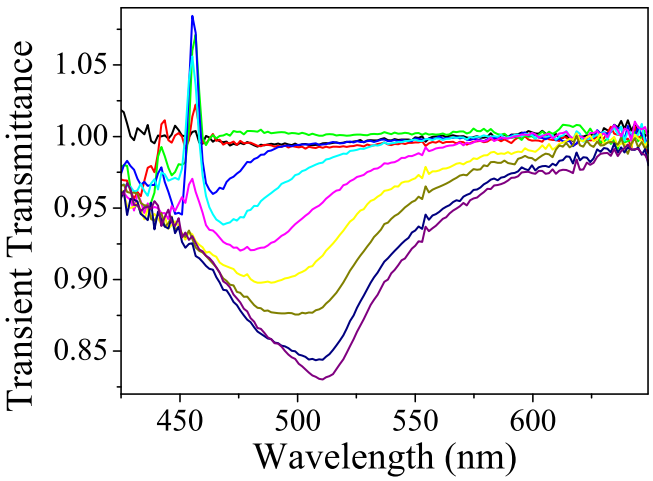

Figure 2.2: Evolution of transient absorption band of 2metO-1HAQ in acetonitrile following 400 nm excitation.

The measurement of the peak to peak temporal offset within the spectral width of the probe defines the temporal dispersion of the white pulse. The plot in Figure 2.3 a plot show a typical dispersion curve obtained with the method described in section 2.4.1. It is worth to notice that the extent of the dispersion itself might undergo day by day fluctuations of the order of 15% due to specific conditions (as,

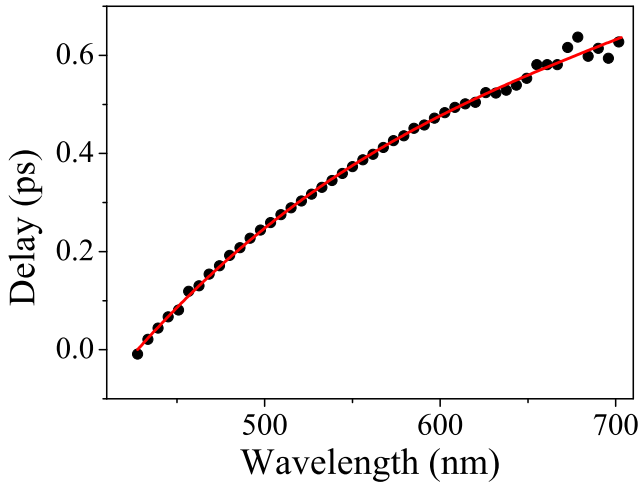

Figure 2.3: Group velocity dispersion of the white light continuum pulse, measured by OKE (*circles*), of an acetonitrile solution of 2metO-1HAQ; $\lambda_{pump} = 400$ nm . The *red* curve has been obtained by polynomial fitting procedure.

for example, the focal position inside the fluorite plate of the white light generator) which happen to be the aftermath of the continuum stabilization procedure.

Chapter 3

7-Hydroxycoumarin

3.1 Introduction

7-Hydroxycoumarin or *Umbelliferone* is one of the most investigated coumarin and its schematic structure is shown in Fig.3.1. Just to introduce this compound and to

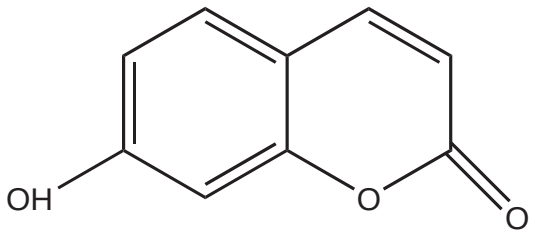

Figure 3.1: Umbelliferone structure

give a general overview of its applications we can directly cite the description given by the famous free on-line encyclopedia *Wikipedia*:

"Umbelliferone or 7-hydroxycoumarin is a widespread natural product of the coumarin family. It occurs in many familiar plants from the Apiaceae (Umbelliferae) family such as carrot, coriander and garden angelica, as well plants from other families such as the mouse-ear hawkweed. It is a yellowish-white crystalline solid which has a slight solubility in hot water, but high solubility in ethanol. Despite several indications that this chemical is photomutagenic it is used in sunscreens.

Umbelliferone absorbs strongly at 300, 305 and 325 nm, with logε values of 3.9, 3.95 and 4.15 respectively, and it fluoresces blue in both ultraviolet and visible light. The powerful absorption at three different wavelengths, coupled with the fact that the energy is dissipated safely as visible light, make umbelliferone a useful sunscreen agent. The ultraviolet activity of umbelliferone lead to its use as a sunscreen agent, and an optical brightener for textiles. It has also been used as a gain medium for dye lasers. Umbelliferone can be used as a fluorescence indicator for metal ions such as copper and calcium. It acts as a pH indicator in the range 6.5-8.9." [8–10]

This is nothing more than a nice introduction, but it's useful to understand that Umbelliferone is widely employed by industries and it is an easy-available product.

3.2 Proton Dissociation Equilibria

Derivatives of hydroxycoumarin are known to be characterized by large frequency shift of emission and absorption bands in dependence of the solution's pH. Particular attention has been devoted to the characterization of 7-Hydroxy-4-methylcoumarin (7H4MC) and 7-Hydroxycoumarin (7HC) in the ground singlet S_0 and first singlet S_1 excited states. Several authors investigated the behavior of this compounds in different solvents and pH conditions by means of static [11–33] and time resolved [27,28,34,35] spectroscopic techniques.

Fink *et al.* [16] found that the Umbelliferone's absorption spectrum in acid solution (pH<6) has a maximum of absorbance at $\sim 325nm$; but at higher pH (pH>8) the band maximum shifts to $370nm$. At the same time, the emission spectrum is characterized by a blue fluorescence in the pH range $2.2 \leq pH \leq 11.2$, with maximum around $460nm$. When the pH is lowered till 1.2, a red shift is observed and the band's maximum moves around $480nm$.

A large number of papers have been published on the spectroscopic properties of 7H4MC, and strong analogies have been found between 7H4MC and 7HC. This allowed us to follow the results obtained for 7H4MC to rationalize the absorption

and emission spectra of 7HC.[30]

In the next section we present a detailed analysis of the changes of absorption and emission spectra in dependance to the solution's pH for 7H4MC.

3.2.1 Absorption Spectra

Hoshiyama *et al.*[30] measured the ground state absorption of 7H4MC in MeOH-water mixture, because solvents with excellent hydrogen-bonding affinities are able to support dissociation equilibria. The results can be extended also to water, but in different pH conditions.[27]

Titration curve of 7H4MC (inset of Fig.3.2) shows that in alkaline solutions (pH=11) the absorption maximum shifts from $320nm$ to $360nm$.

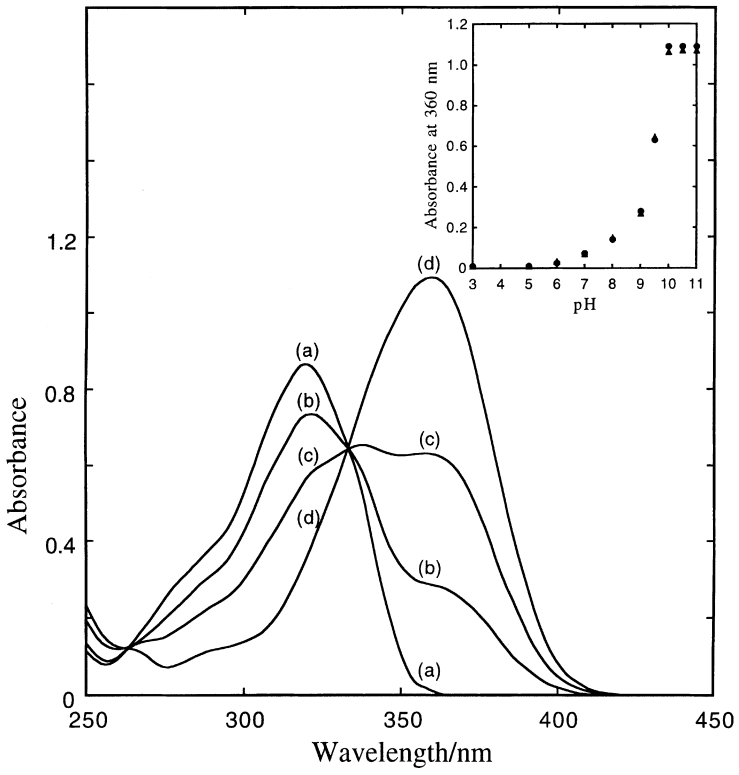

Figure 3.2: pH dependence of the UV absorption spectrum of 7H4MC (5.0×10^{-5} mol dm^{-3}) in 2% vol. MeOH H_2O containing KCl (0.1 mol dm^{-3}) at 24 $\pm$1 C°. pH: (a) 5.0; (b) 9.0; (c) 9.5; (d) 10.5.

This shift is related to the presence of anionic species in the ground state and Hoshyama *et all.*[30] show that the anionic form undergoes to the following tautomeric equilibrium:

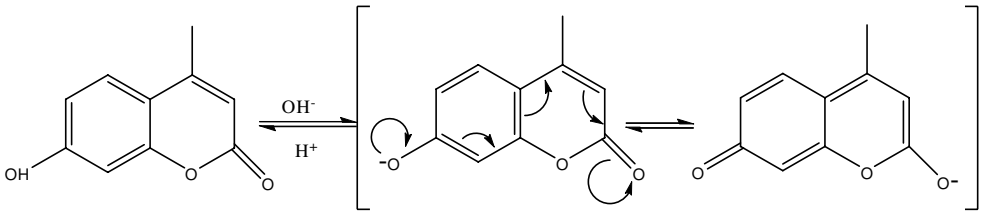

Figure 3.3: Ground state tautomeric equilibrium in alkaline solutions.

The ground state species is the neutral form from pH=1 to pH=4.5, while in strong acid media the protonated species prevail.

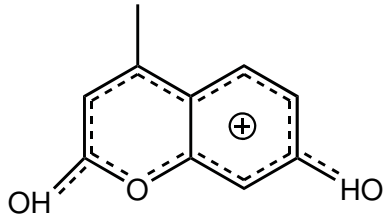

Figure 3.4: Protonated form of 7H4MC.

The distribution, as a function of pH, of the absorbing species can be summarized as follow:

- **pH>10.0** ⇒ Tautomeric equilibrium between anionic forms; absorbance maximum at **360nm**.
- **5.0<pH<10** ⇒ Equilibrium between the neutral and anionic form.
- **1.0<pH<5** ⇒ Neutral form with absorbance maximum at **322nm**.
- **pH<1** ⇒ Cationic Form with absorbance maximum at **345nm**.[17]

3.2.2 Emission Spectra

We can rationalize the behavior in the S_1 excited state of 7H4MC with the help of the spectrofluorimetric titration curve obtained by Hoshyama *et all.*[30] (Figure 3.5) and taking into account the results of Yakatan *et al.*.[17]

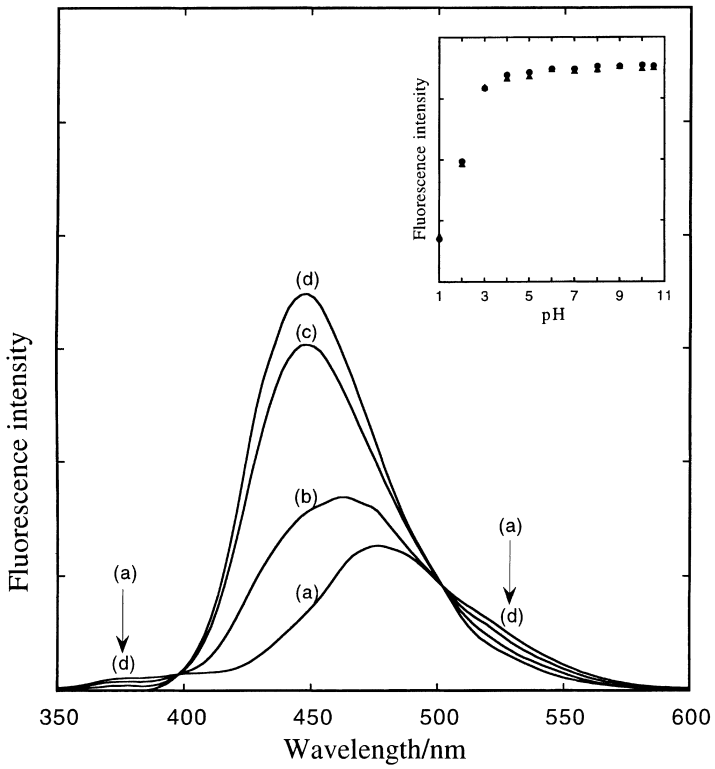

Figure 3.5: pH dependence of the fluorescence spectrum of 7H4MC (5.0×10^{-5} mol dm^{-3}) in 2% vol. MeOH H_2O containing KCl (0.1 mol dm^{-3}) at 24 ± 1 C°. Excitation wavelength (λ_{exc}): 333 nm. pH: (a) 1.0 (0.1 mol dm^{-3} HCL); (b) 2.0; (c) 3.0; (d) 10.5. Inset: spectrofluorimetric titration curve for 7H4MC.

We divided the whole pH range in four intervals to better define the spectral features of a particular species.

1. Strong alkaline solutions (**pH>10**)

   For $[H^+]$ lower than 10^{-10} the fluorescence maximum is around **450 nm** and both ground and excited state species are in the anion form: *the tautomeric*

pair. In this range of pH the absorption and emission spectra are well described by the potential well scheme of Fig.3.6.

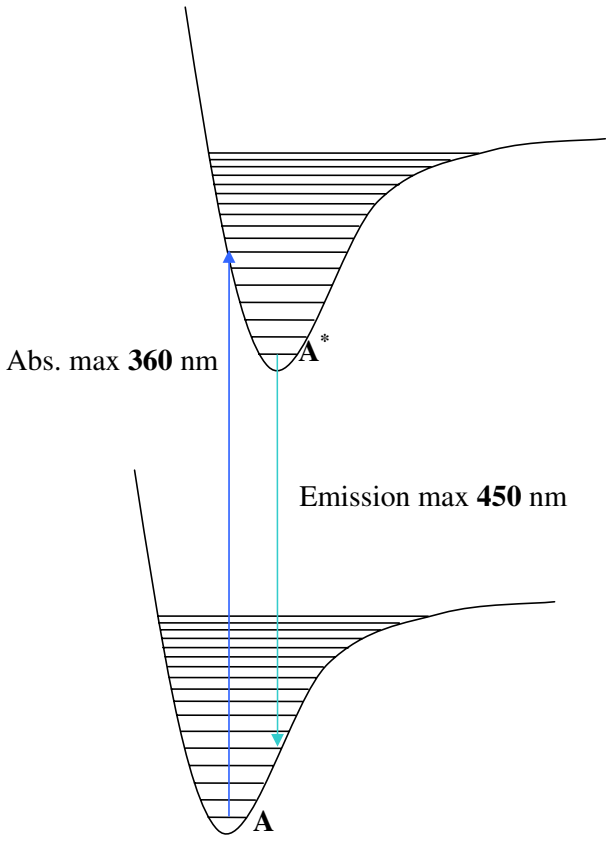

Figure 3.6: Potential well scheme of 7H4MC in strong alkaline solutions.

2. Alkaline solutions **6<pH<10**

   When the pH is gradually lowered, a different behavior of the absorption and emission spectra is observed.

   Until pH= 3 the fluorescence spectrum shows a band centered at **450 nm**, meaning that the emitting species is the anionic tautomer pair.

   On the contrary, the ground state species is not well defined. The titration absorption curve (Fig.3.2) shows that the anion tautomer pair is the main ground state species only at pH>10. Then, in this pH range the ground S_0

state is characterized by the equilibrium between the anionic pair and the neutral form. The absorbing and emitting species are schematically represented in Fig.3.7.

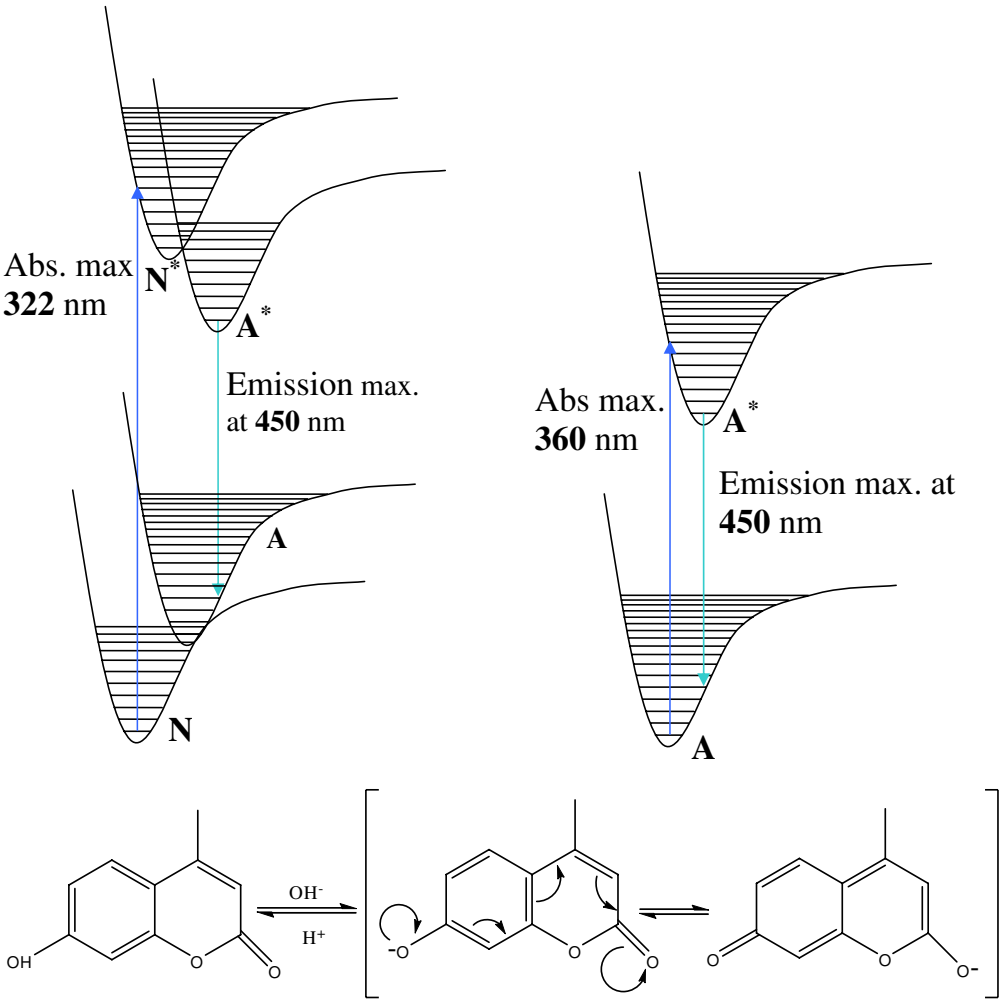

Figure 3.7: Ground and excited state species of 7H4MC in alkaline solutions.

3. Acid solutions **1<pH<6**

Neutral form is the main absorbing species in this pH region, as confirmed by the comparison between the absorption maximum in Methanol-Water mixtures[30] (322 nm) and the absorption in polar non-protic[33] solvent (320 nm), and the fluorescence spectrum is characterized by three bands (Fig.3.5).

(a) 480 band is attributed to the protonated C* species because this band disappears increasing the pH and because the basicity of the ester carbonyl group increases in the singlet excited state of 7HC.

(b) 450 nm band is related,as stated before, to the tautomer anion form.

(c) 380 nm band (very low intensity in this 2% MeOH - Water mixture) is related to the emitting excited neutral form N*. The assignment of this band is made by comparison of fluorescent measurements in pure polar non-protic or low-protic solvents: 384 nm (pure ethanol or chloroform). [36]

The various spectral features can be schematically correlated as shown in Figure 3.8.

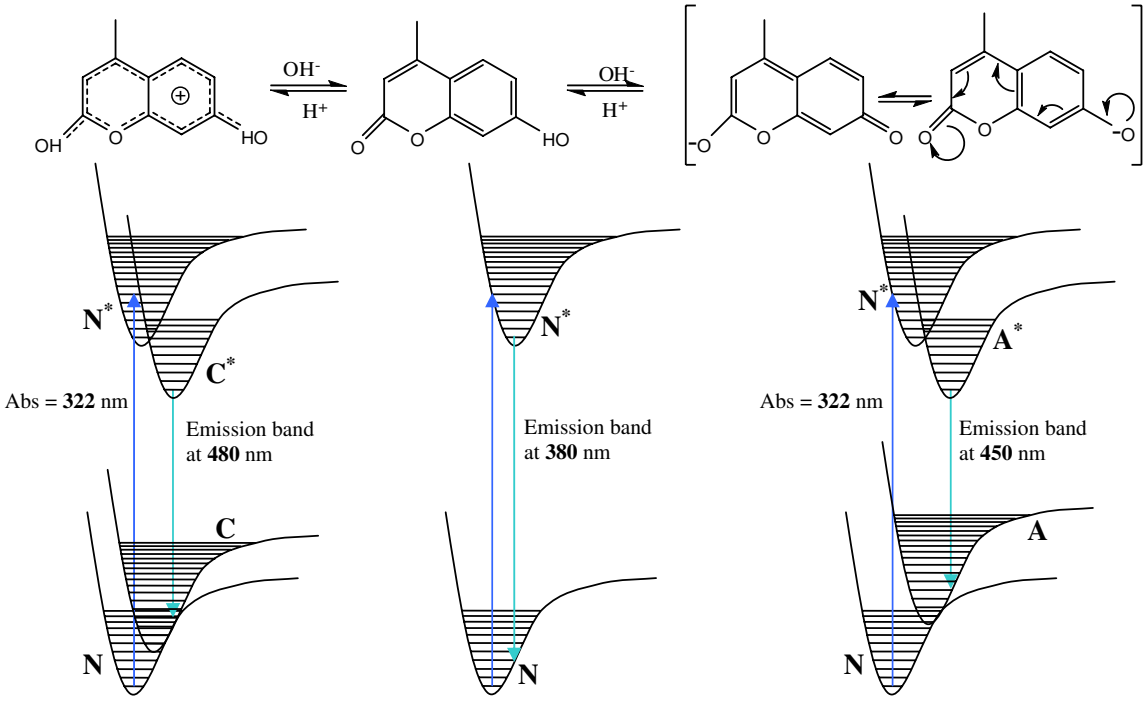

Figure 3.8: Ground and excited state species of 7H4MC in acid solutions.

4. Strong acid solution **-10<H_0-pH<1**

This pH range, for both absorption and fluorescence spectra, is dominated by the protonated form of 7H4MC. This is the result that Yakatan *et al.*[17] reported in their work. The maximum of absorption band is at 345 nm, while the fluorescence emission is centered around 412 nm. Hence, the spectra are consistent with the model depicted in Fig.3.9.

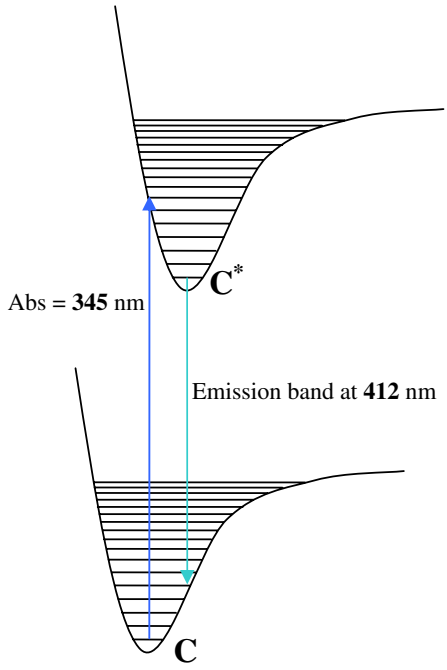

Figure 3.9: Ground and excited state species of 7H4MC in strong acid solutions.

3.3 Absorption and Emission spectra

Fluorescence and absorption spectra of Umbelliferone have been recorded in pure acetonitrile. The absorption spectrum, shown in Figure 3.10, consists of an intense band centered at 320 nm: $\varepsilon \simeq 13000\ l * mol^{-1}$ and oscillator strength $f = 0.3 \pm 0.02$. Acetonitrile is an aprotic solvent of low polarity, so that no tautomeric equilibrium is observed in the S_0 ground state. As discussed above, we can associate the absorption spectrum to the Neutral form N. The fluorescence spectrum ($\lambda_{exc} =$

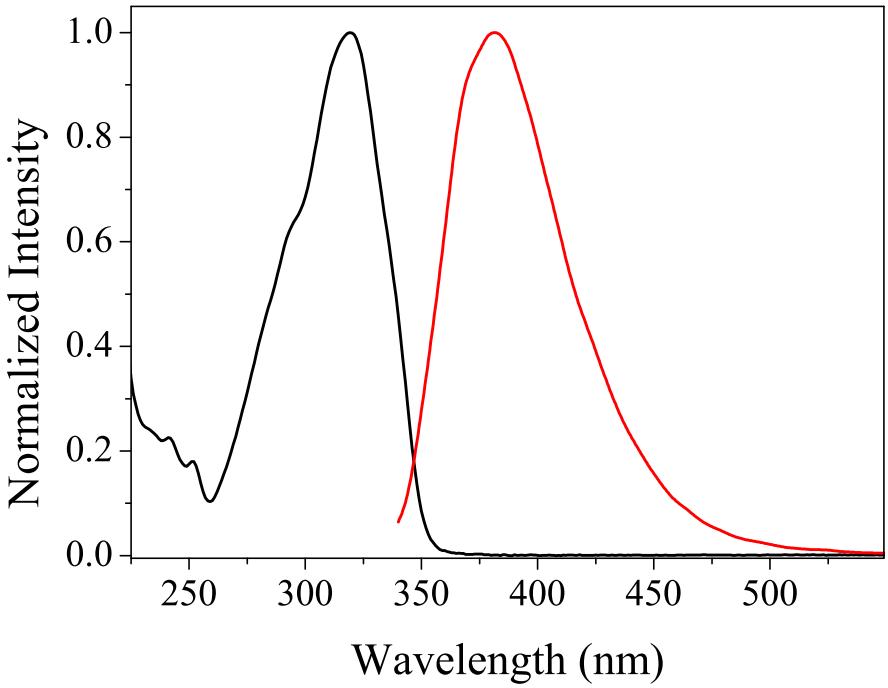

Figure 3.10: Ground state absorption and fluorescence (λ_{exc} = 325 nm) spectra of 7HC in acetonitrile.

325 nm) is characterized by a broad and not structured band centered at 380 nm (Φ= 0.0035 $\pm$ 0.0005). This indicates that also the emitting species is in its neutral form. We noticed some modification of the fluorescence spectrum during the various measurement sessions. In particular, after one day of measurement, we observed an enhancement of the fluorescence at 450 nm while the absorption spectrum is not affected (Figure 3.11). As stated before, Hoshyama *et al.*[30] found that Umbelliferone, in ethanol-water mixture, undergoes proton dissociation equilibria; when the pH is gradually increased (from pH=5 to pH=10), they observed an intensity enhancement of the 450 nm band. Therefore, the observed modifications can tentatively be associated to the formation of anionic form in the S_1 excited state due to the presence of a very small percentage of water molecules in the solvent. Then, all measurements have been performed with particular care of avoiding air exposure of

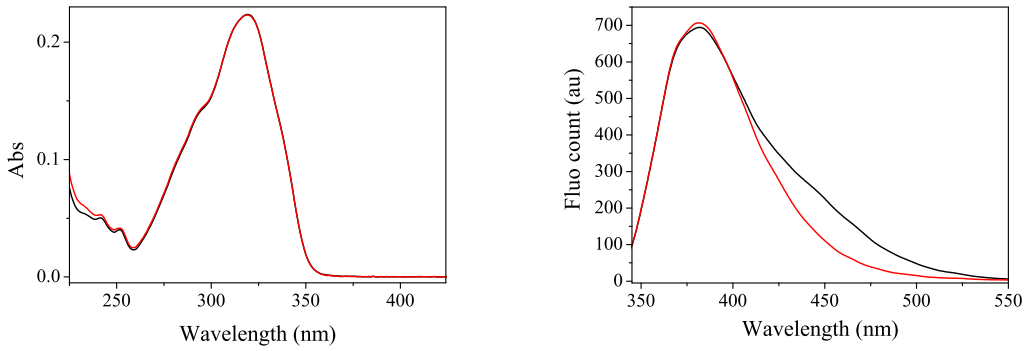

Figure 3.11: Modifications of Umbelliferone's absorption and emission spectra: (*black*) altered solution and (*red*) just prepared solution.

solid 7HC and acetonitrile.

3.4 Electronic structure characterization

In the previous chapter we emphasized that 7HC and 7H4MC have a peculiar behavior in aqueous and protic solvent for the ground and excited state spectroscopic properties. This is the main reason for the characterization of electronic transitions (Absorption and Fluorescence) and electronic structure by means of *ab initio* methods. Georgieva *et al.*[37–39] performed a detailed analysis of the ground and excited state properties of 7H4MC in the gas phase and in water, while Adamo *et al.*[40,41] presented an investigation of the fluorescence and absorption spectra of 7HC and 7H4MC in the gas phase and in protic solvents (water, Methanol and Ethanol). On the basis of these works we can state that *DFT* for the ground state and *TD-DFT* for the excited state represent good theoretical approaches for coumarins, well reproducing the experimental data at a low computational cost. The purpose of this part of the work is to calculate the geometric parameters and the vertical transitions in the solvent reaction field (acetonitrile) with the perspective of extending the *ab initio* calculation to the bichromophore. Hence, particular attention has been payed to compare the results obtained by different basis sets in order to choose the least ex-

pensive, from the computational point of view, level of theory without compromising the accuracy of the calculation.

3.4.1 Computational procedure

All calculation were performed with the GAUSSIAN03 program package.[42] In all cases the self-consistent field (SCF) convergence criteria have been tightened to, at least, 10^{-9} a.u. and all geometry optimizations have been performed until the residual mean force is smaller than 1.0×10^{-5} a.u. (tight threshold in Gaussian). The calculations has been performed with the 6-31+G(d,p) and, further, to verify the reliability of the obtained results, larger basis set, 6-311++G(2df,2pd) was used to calculate geometry optimization and vertical transitions. Pople style basis set. The non local three-parameter hybrid exchange B3LYP density functional,[43,44] as implemented in the Gaussian03 package, was employed. The frequencies associated to the vertical ground-to-excited state transitions have been calculated by means of the *TD-DFT* method with the above mentioned density functional and basis sets. The bulk solvent effects are evaluated by means of the PCM (polarizable continuum model) in its integral equation formalism form.[45]In continuum models, one divides the model into a solute part, the dye, lying inside a cavity, surrounded by the solvent part: acetonitrile in our study. The PCM-TD-DFT calculations have been performed with the linear response method and the absorption maxima computed in the presence of the solvent reaction field have been determined with the so called non-equilibrium solutions.[46]

3.4.2 Ground state properties and geometry optimization

As emphasized in section 3.3, the absorbing and emitting species are the neutral form of 7HC due to the low polar and aprotic character of the solvent (acetonitrile). This allowed us to limit the calculation only to the neutral *enol* species. A detailed *ab initio DFT* calculation concerning the properties of the various species that compose

the ground state equilibrium, was performed by *Georgieva et al*[37] for the 7H4MC chromophore.

The crystal structure of 7HC was determined by *Ueno*[47]; a schematic *"ball and stick"* representation, with atoms numbering, is given in Figure 3.12. Crystals of 7HC were obtained from an aqueous ethanol solution and the diffraction pattern revealed the presence of some crystallization's water molecules. *Ueno*[47] found that the molecule was nearly planar, the $H(18)-O(12)-C(6)-C(1)$ torsion angle being 177.3(7)°, and that the various molecules were stacked along the a axes of the crystal. 7HC molecules formed inter-molecular hydrogen-bonds $O(12)-H(18)....O(11)$ giving rise to a ribbon along the c axis and stabilizing the crystal packing.

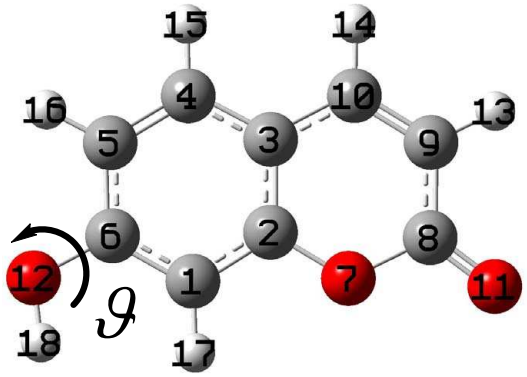

Figure 3.12: *"Ball and Stick"* representation of α conformer (ϑ=0°) of Umbelliferone.

Before going in a detailed analysis of the calculated geometric parameters, we have to consider that the experimental data were obtained from crystals in which each molecule is involved in inter-molecular hydrogen bonds. The hydrogen bonds constrain the molecule in a fixed conformation: the one which allows the molecular system to form a chain and to maintain the crystal's symmetry. We performed a conformational analysis on the rotation angle along the C(6)-O(12) bond in order to get information about the conformational rigidity and to compare these results with the experimental structure. The structure found by *Ueno*[47] was nearly planar,

Table 3.1: Relative energy (corrected with ZPVE Kcal*mol-1) between α and β conformer.

	B3LYP/6-31+G(d,p)		*B3LYP/6-311++G(2df,2pd)*	
Conformer	*gas phase*	*solution*	*gas phase*	*solution*
α	0	0	0	0
β	0.46	0.05	0.29	0.009

what led us to consider only two possible conformers: one with the torsion angle $\vartheta \sim 0°$ (showed in Figure 3.12) that we denoted as α, and the second one with $\vartheta \sim 180°$ that we denoted as β. We optimized the geometry of both the conformers at the *B3LYP/6-31+G(d,p)* and *B3LYP/6-311++G(2df,2pd)* level of theory in gas phase and in the solvent reaction field (acetonitrile). All the optimized structures were minima of the hyper-potential well, as confirmed by the absence of imaginary vibrational frequencies, all belonging to the C_s symmetry group. The experimental and calculated geometric parameters are collected in Table 3.2 and 3.4. The average deviations of the calculated bond length were in the range of $0.7\% - 1.3\%$, while the standard deviation for the calculated bond valence angles were in the range $0.45\% - 1.7\%$.

We found the conformer α having the lowest energy in the gas phase and in the presence of the solvent, and we obtained the same energy ordering with the two employed basis set. The computed energy differences (corrected for the *Zero Point Vibrational Energy* ZPVE) are listed in Table 3.1. Adopting a larger basis set not only improved the calculated geometric parameters, as we can see from the standard deviation's values reported in Table 3.2 and Table 3.4, but also reduced the energy difference between the two conformers.

The obtained results are in contrast with the experimental structure: in fact, *Ueno*[47] found that the stable structure is characterized by the ϑ torsional angle $\sim$ 180°. Nevertheless, the calculated energy differences between the two conformations

Table 3.2: Calculated and experimental selected bond length (Å) for the conformer $\alpha(\vartheta = 0°)$ and $\beta(\vartheta = 180°)$ [(1)]in gas phase and [(2)]in acetonitrile. [(3)]Atom numbering is given in Figure 3.12 .

		B3LYP/6-31+G(d,p)				*B3LYP/6-311++G(2df,2pd)*			
Name definition[(3)]	*Exp.*[47]	$\beta^{(1)}$	$\beta^{(2)}$	$\alpha^{(1)}$	$\alpha^{(2)}$	$\beta^{(1)}$	$\beta^{(2)}$	$\alpha^{(1)}$	$\alpha^{(2)}$
O(7)-C(8)	1.367(2)	1.400	1.386	1.402	1.387	1.396	1.381	1.398	1.382
O(7)-C(2)	1.382(2)	1.365	1.373	1.364	1.373	1.358	1.367	1.358	1.366
C(8)-C(9)	1.433(3)	1.457	1.446	1.456	1.445	1.453	1.441	1.452	1.441
C(8)-O(11)	1.224(2)	1.210	1.226	1.211	1.226	1.201	1.217	1.201	1.217
C(9)-C(10)	1.341(2)	1.355	1.361	1.356	1.361	1.347	1.353	1.348	1.353
C(10)-C(3)	1.424(2)	1.438	1.433	1.438	1.433	1.433	1.428	1.432	1.428
C(4)-C(5)	1.368(3)	1.387	1.385	1.384	1.383	1.380	1.378	1.377	1.376
C(4)-C(3)	1.411(2)	1.407	1.411	1.410	1.413	1.401	1.405	1.404	1.406
C(5)-C(6)	1.396(3)	1.408	1.412	1.408	1.412	1.402	1.405	1.401	1.406
C(6)-C(1)	1.393(2)	1.395	1.398	1.395	1.398	1.388	1.392	1.389	1.391
C(6)-O(12)	1.351(2)	1.364	1.357	1.363	1.357	1.359	1.352	1.359	1.352
C(1)-C(2)	1.376(2)	1.392	1.390	1.395	1.393	1.386	1.384	1.389	1.386
C(2)-C(3)	1.398(2)	1.412	1.410	1.409	1.409	1.405	1.404	1.403	1.402
stdv		**0.018**	**0.013**	**0.018**	**0.013**	**0.016**	**0.009**	**0.016**	**0.009**
stdv%		**1.28%**	**0.95%**	**1.28%**	**0.95%**	**1.17%**	**0.67%**	**1.17%**	**0.69%**

Table 3.3: Calculated and experimental selected bond angles (A-valence) (degrees) for the conformer $\alpha(\vartheta = 0°)$ and $\beta(\vartheta = 180°)$ $^{(1)}$in gas phase and $^{(2)}$in acetonitrile. $^{(3)}$Atom numbering is given in Figure 3.12 .

		B3LYP/6-31+G(d,p)				*B3LYP/6-311++G(2df,2pd)*			
Name definition$^{(3)}$	*Exp.*[47]	$\beta^{(1)}$	$\beta^{(2)}$	$\alpha^{(1)}$	$\alpha^{(2)}$	$\beta^{(1)}$	$\beta^{(2)}$	$\alpha^{(1)}$	$\alpha^{(2)}$
C(2)O(7)C(8)	121.9(1)	123.0	122.8	122.9	122.8	123.0	122.9	122.9	122.9
O(7)C(8)C(9)	118.2(2)	116.1	117.1	116.0	117.0	115.9	116.9	115.8	116.8
O(7)C(8)O(11)	115.9(2)	117.5	116.5	117.4	116.4	117.6	116.6	117.5	116.6
C(9)C(8)O(11)	125.9(2)	126.4	126.5	126.6	126.5	126.5	126.5	126.7	126.6
C(8)C(9)C(10)	120.6(2)	121.4	120.9	121.4	120.9	121.5	121.0	121.5	121.0
C(9)C(10)C(3)	121.0(2)	120.9	120.9	121.0	120.9	121.0	121.0	121.0	121.0
C(5)C(4)C(3)	120.7(2)	121.1	121.0	121.3	121.0	121.1	121.0	121.3	121.0
C(4)C(5)C(6)	120.3(2)	119.5	119.7	119.4	119.7	119.6	119.7	119.4	119.8
C(5)C(6)C(1)	120.6(2)	120.9	120.8	120.9	120.8	120.8	120.7	120.8	120.7
C(5)C(6)O(12)	122.0(2)	122.2	122.3	116.7	116.7	122.1	122.2	116.9	116.9
C(1)C(6)O(12)	117.4(2)	116.9	116.9	122.4	122.5	117.1	117.1	122.3	122.5
C(6)C(1)C(2)	118.0(2)	118.7	118.4	118.8	118.3	118.8	118.5	118.9	118.5
O(7)C(2)C(1)	117.0(2)	117.1	117.1	117.0	117.0	117.2	117.2	117.2	117.2
O(7)C(2)C(3)	120.0(1)	121.0	120.5	121.2	120.5	121.0	120.5	121.2	120.6
C(1)C(2)C(3)	123.0(2)	121.9	122.4	121.7	122.4	121.8	122.2	121.6	122.2
C(10)C(3)C(4)	124.5(2)	124.5	124.5	124.6	124.5	124.5	124.5	124.6	124.5
C(10)C(3)C(2)	118.2(2)	117.6	117.8	117.4	117.8	117.5	117.7	117.4	117.7
C(4)C(3)C(2)	117.3(2)	117.9	117.7	117.9	117.8	118.0	117.8	118.0	117.8
stdv		**0.9**	**0.5**	**2.0**	**1.9**	**1.0**	**0.6**	**2.0**	**1.9**
stdv%		**0.75%**	**0.44%**	**1.68%**	**1.55%**	**0.80%**	**0.49%**	**1.66%**	**1.55%**

are very low and the geometry optimizations were performed in gas phase and in acetonitrile, where hydrogen-bonding interactions are not present (gas phase) or not explicitly considered (solvent reaction field simulated with PCM method).

In order to calculate the energy barrier for the rotation around ϑ we performed a geometry optimization of the *transition state structure* followed by an *intrinsic reaction path* (IRC) calculation. By definition a transition state is identified as a

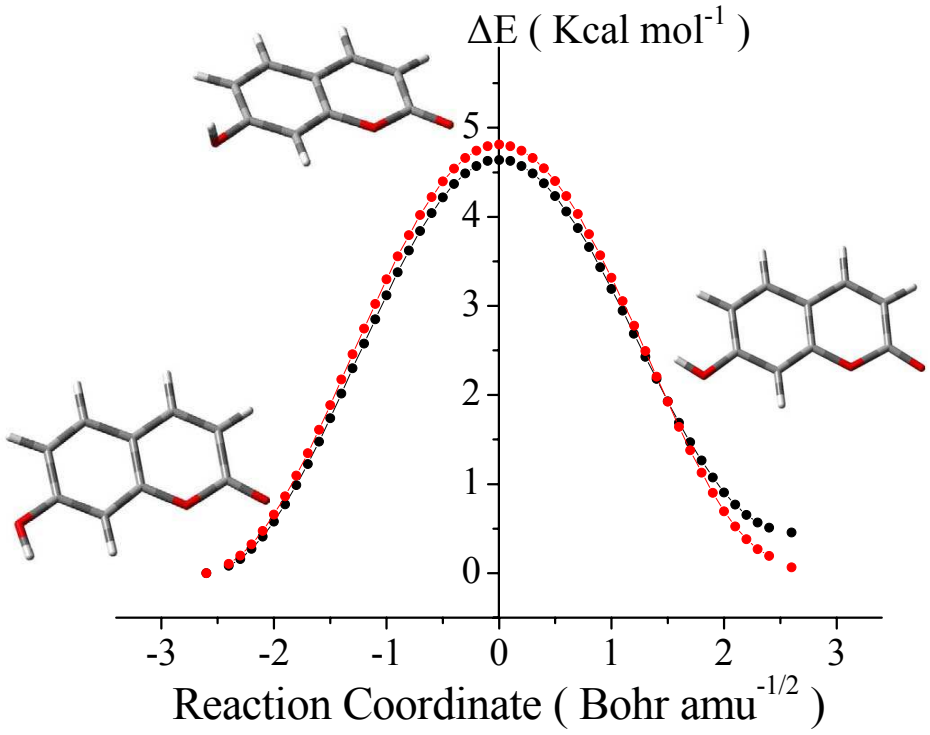

Figure 3.13: *Intrinsic Reaction Path*, along the reaction coordinate, in gas phase (*black* bullet) and in the solvent reaction field *red bullet*

first order-saddle point on the potential energy surface: a maximum in the reaction coordinate direction and a minimum along all the other coordinates. In the normal coordinate system this is equivalent to say that the transition state (TS) is characterized by the presence of one and only one negative eigenvalue of the dynamical matrix, which corresponds to an imaginary frequency. At the transition state the eigenvector for the imaginary frequency is the reaction coordinate and the

reaction path can be followed taking small steps along the TS eigenvector. The calculation was performed in the gas phase and in the solvent reaction field with the $6-31+G(d,p)$ basis set only. The path along the reaction coordinate connecting the two conformers is shown in Figure 3.13, where the reported energies were not corrected for the ZPVE. The inclusion of solvent effect, through the PCM method, causes only a small increase of the energy barrier going from 4.64 $Kal * mol^{-1}$ (gas phase) to 4.81 $Kal * mol^{-1}$ (solvent). Hence, due to the low energy barrier of the $\alpha - \beta$ interconversion, both the conformers can be present in solution at room temperature. Since the obtained results for the two conformers are virtually identical, hereafter we decide to consider only the conformer α.

To select an efficient basis set, which reliably describes the geometrical parameters in the ground state, we considered a reduced list of bond lengths, and compared our data with the results obtained by Georgieva *et al.*[38] for 7H4MC and by Adamo *et al.*[41] for 7HC. In the gas phase, the calculated bond lengths with B3LYP/6-31+G(d,p) set are characterized by similar percent standard deviation, in respect to the experimental data, similarly to the results obtained by Adamo[41] and Georgieva[37,38]. Extending the basis set does not bring any a sensible improvement of the calculated bond lengths and the percent standard deviation is comparable with the B3LYP/6-31+G(d,p) method.

Better agreement in respect to the experimental data is obtained introducing the solvent effect. The main consequences of the interaction between molecule and the solvent reaction field are the elongation of the carbonyl double bond (C(8)-O(11)) and the shortening of single C-O bond (C(6)-O(12)) and O-H bond (O(12)-H(18)).

We conclude that the introduction of diffuse functions on the hydrogen atoms and the triple-ζ description of the valence orbitals does not result in an improvement of the geometric parameters; hence, from this perspective, the B3LYP/6-31+G(d,p) level of theory seems to be a reasonable balance of accuracy/computational time.

Table 3.4: Selected calculated and experimental bond lengths (Å) for the conformer $\alpha(\vartheta = 0°)$: [(1)]Adamo *et al.*[41] PBE0/6-31+G(d), Gas Phase and Ethanol (PCM); [(2)]Georgieva *et al.*[38] B3LYP/SVPD, Gas Phase and Water (PCM); [(3)]Georgieva *et al.*[37] B3LYP/6-31G(d), Gas Phase; [(3)]Atom numbering is given in Figure 3.12 .

							B3LYP/6-31+G(d,p)		*B3LYP/6-311++G(2df,2pd)*	
Name definition[(3)]	exp	Gas[1]	Ethanol[1]	Gas[2]	Water[2]	Gas[3]	Gas	acetonitrile	Gas	acetonitrile
C(8)-O(11)	1.224	1.207	1.222	1.206	1.222	1.208	1.211	1.226	1.201	1.217
O(7)-C(8)	1.367	1.389	1.375	1.334	1.377	1.401	1.402	1.387	1.398	1.382
C(6)-O(12)	1.351	1.354	1.347	1.357	1.350	1.361	1.363	1.357	1.359	1.352
O(12)-H(18)				0.965	0.987	0.970	0.967	0.988	0.962	0.983
stdv%		**1.51%**	**0.48%**	**2.02%**	**0.53%**	**2.05%**	**2.07%**	**1.07%**	**2.12%**	**0.89%**

3.4.3 Calculation of Vertical Transitions

Vertical excitation energies have been calculated at the TD-B3LYP /6-31+G(d,p) and /6-311++G(2df,2pd) level of theory both in the gas phase and in the solvent. Values obtained for the first singlet transitions, along with the estimated oscillator strength, are reported in table 3.5

Within the Kohn-Sham approach the character of the various transitions can be estimated from the coefficients of the orbitals involved in the electron excitation process. Under this assumption, we obtain that the first vertical transition is $(\pi\pi^*)$ in character, being essentially due to the promotion of one electron from the HOMO to the LUMO orbital. The extension of the basis set, brings to a systematic increase of the excitation energy, especially for the first $(n\pi^*)$ transition ($\sim$ 0.04 eV).

The solvent effect has been estimated on the basis of the PCM model. In general, a bathochromic solvent shift is calculated for the $(\pi\pi^*)$ excitation energies and an hypsochromic shift is found for the $(n\pi^*)$ transitions. The gas phase $^1(\pi\pi^*)$ excitation energies (4.11 eV and 4.13 eV) are higher than the experimental one (3.82 eV) by 0.29 eV and 0.31 eV. The calculated PCM solvent shift decreases the $^1(\pi\pi^*)$ excitation energies and brings them into better agreement with the experiment.

We conclude that for the calculation of the ground state parameters and for the vertical excitation energies, there are not sensible improvements by extending the basis set. On the contrary, the inclusion of solvent effect is of great relevance to obtain a better description of the molecular system.

3.5 Transient Absorption Spectra

Transient spectra of Umbelliferone have been recorded following the excitation at 325 nm. The excitation wavelength has been obtained by (fourth harmonic generation) *FHG* of the output of a BBO-based OPA (section 2.1). The spectra are characterized by an excited state absorption *(ESA)* band centered at 355 nm and a stimulated emission *(SE)* band at 405 nm (Figure 3.14(a)). There is also evi-

Table 3.5: TDDFT Vertical excitation energies, in eV and cm^{-1}, and Oscillator strength for the first five singlet excited states of Umbelliferone. .

	B3LYP/6-31+G(d,p)						*B3LYP/6-311++G(2df,2pd)*					
	Gas			Acetonitrile			Gas			Acetonitrile		
state	ΔE (eV)	ΔE (cm^{-1})	f	ΔE (eV)	ΔE (cm^{-1})	f	ΔE (eV)	ΔE (cm^{-1})	f	ΔE (eV)	ΔE (cm^{-1})	f
2^1A'($\pi\pi^*$)	4.11	33160	0.30	3.95	31851	0.45	4.13	33302	0.30	3.97	32023	0.44
3^1A'($\pi\pi^*$)	4.48	36126	0.03	4.36	35186	0.00	4.50	36273	0.02	4.39	35428	0.00
1^1A"($n\pi^*$)	4.49	36202	0.00	4.61	37162	0.00	4.51	36364	0.00	4.65	37470	0.00
4^4A'($\pi\pi^*$)	4.53	36498	0.04	4.83	38988	0.05	4.57	36855	0.05	4.87	39254	0.05
2^2A"($n\pi^*$)	4.98	40156	0.00	4.87	39317	0.02	5.01	40419	0.00	4.91	39571	0.00

dence of an absorption band on the low frequency side of the *SE* band. We have two sets of Umbelliferone's transient spectra, recorded with two different detector systems. The spectra shown in Figure 3.14(a) have been recorded with an UV-enhanced CCD 1100×330 pixels (Princeton-Instrument), while the spectra shown in Figure 3.14(b) were obtained with a home-made acquisition system based on two silicon arrays (256 channels each) as photosensible surface (section 2.1). The shape of the long wavelength spectral feature is better appreciated in the transient spectra recorded with the second detector. This band is broad compared to the *blue ESA* (350 nm) and it is probably peaked at low frequency. The temporal behavior in the first picosecond is shown in Figure 3.14(a) and Figure 3.14(b). The spectra in the figures are not corrected for the group velocity dispersion of the probe beam. Once corrected for the dispersion, we observe that the three bands grow-up with the same rise time: they appear simultaneously. This means that they are associated to transitions from the same excited state. In Figure 3.14(a) the band associated to the solvent's stimulated raman gain (*SRG*) is evident (peaked around 370 nm); the *SRG* is a parametric and coherent effect that is observed only when the pump and probe pulses are temporally coincident and it is one of the commonly employed internal standard for determining the instrumental function (cross-correlation function between pump and probe pulses) in transient absorption experiments. The *ESA* and *SE* bands grow-up in the same temporal interval of the *SRG* signal's evolution, meaning that for our instrumental resolution they are instantaneous. The observed bands are then associated to transitions from the state directly populated by the excitation pulse. The qualitative analysis of the transient spectra lead us to conclude that the photoexcitation of the Umbelliferone with $\lambda_{exc} = 325nm$ involves the direct transfer of electron population from the ground state (S_0) towards the first singlet excited state (S_1). The S_1 state is characterized by two *ESA* bands (centered at $355nm$ and $600nm$), associated to transitions towards higher energy excited states, and the *SE* band (centered at $405nm$).

The temporal evolution of the main spectral features has been inspected by

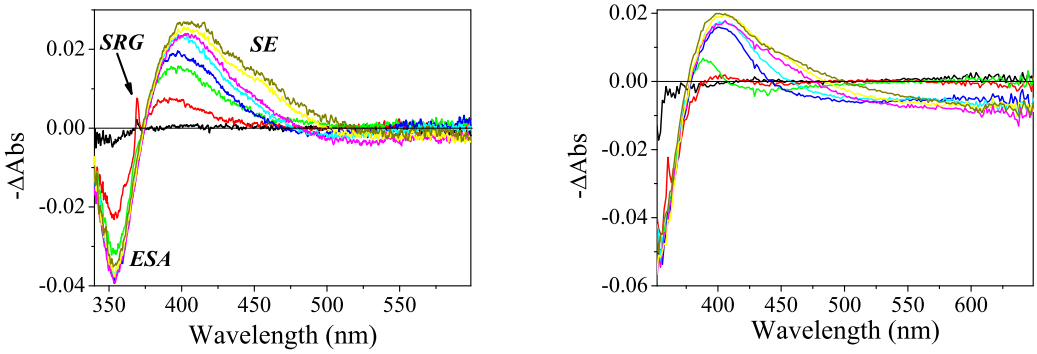

(a) Early evolution (delay in ps): -0.4 (*black*); 0 (*red*); 0.2 (*green*); 0.3 (*blue*); 0.4 (*cyan*); 0.6 (*magenta*); 0.8 (*yellow*); 0.9 (*D.yellow*).

(b) Early evolution (delay in ps): -0.5 (*black*); 0 (*red*); 0.3 (*green*); 0.5 (*blue*); 0.6 (*cyan*); 0.8 (*magenta*); 0.9 (*yellow*); 1 (*D.yellow*).

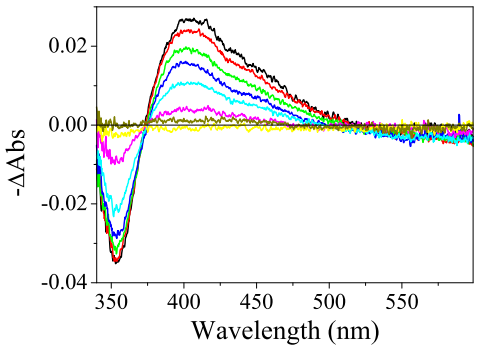

(c) Long time evolution (delay in ps): 0.9 (*black*); 2 (*red*); 5 (*green*); 10 (*blue*); 20 (*cyan*); 50 (*magenta*); 200 (*yellow*); 500 (*D.yellow*).

Figure 3.14: Transient absorption spectra, following 325 nm excitation with ~ 0.8 μJ/pulse, of a solution of Umbelliferone (*solvent*=CH_3CN) with $Abs_{325nm} \simeq$=0.95.

means of single wavelength measurements (section 2.1.2). We choose four different wavelengths: 405, 450, 500 and 550 nm and the acquisition was performed in the same experimental conditions as the transient spectra. We were not able of recording the temporal evolution of the *ESA* band on the blue side of the *SE* band because the interference filter, employed to select the probe wavelength, has spectral range limitation (at high frequencies) at about 370 nm. All the kinetics have been recorded during the same measurement session without changing the spatial overlap between

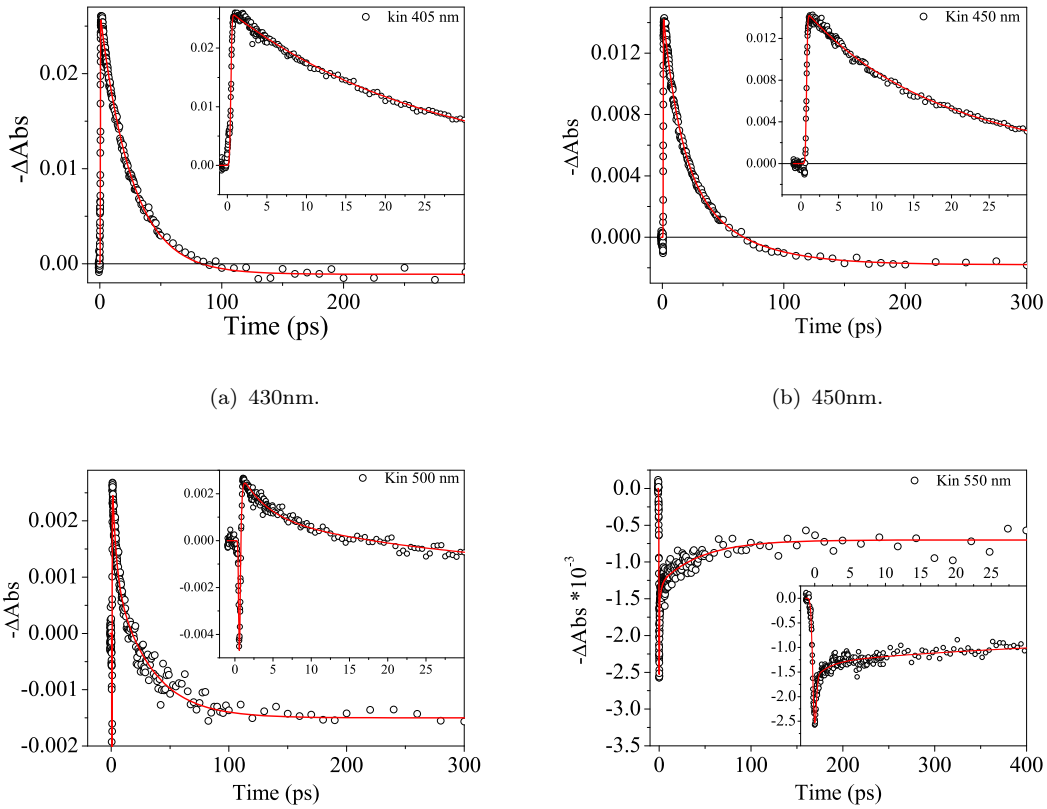

(a) 430nm.

(b) 450nm.

(c) 500nm.

(d) 550nm.

Figure 3.15: Single wavelength measurements following 325 nm excitation with $\sim$ 0.8 μJ/pulse, of a solution of Umbelliferone (*solvent*=CH_3CN) with $\text{Abs}_{325nm} \simeq$=0.95.

the pump and probe beams. The measurement was repeated on different days and on different samples in order to guarantee the reproducibility of data. The maximum intensity $I(t)$ of each kinetic trace was normalized to the value of $-\Delta Abs(t)$ at the same wavelength. This quantity was obtained from the transient absorption experiment; the various traces are shown, along with their fitting curves, in Figure 3.15. The transient signal in the time domain was analyzed with the help of a home developed *global fitting* program. As described in section 2.2, the time domain signal can be reproduced, within the linear response approximation, by the convolution of the instrumental function with the suited molecular response function (Equation

2.14). The instrumental function (cross-correlation between pump and probe pulses) was measured as described in section 2.4.2; the fitting procedure yields a gaussian shape function with 300 fs $FWHM$. The model assumed for the molecular response in the global fitting program, is shown in equation (3.1). The λ subscript means that a different response function for each probed wavelength is considered: all the $R_\lambda(t)$ have the same time constants but they are characterized by different pre-exponential factors and by different values for the *konst* parameter. The strategy of *global fitting* methods is, indeed, the simultaneous simulation of multiple decay traces, usually spread on the spectral range of interest, with the same kinetic model.

$$R_\lambda(t) = \sum_{i=1}^{3} A_{\lambda i}\, exp^{-t/\tau_i} + konst \tag{3.1}$$

Therefore the temporal evolution of all the main spectral features can be simultaneously simulated. This method improves the accuracy for the estimate of the various decay constants because the number of equations available is substantially larger than the number of time constants to be determined.

In order to properly apply the fitting procedure we have to correct the temporal shift between the various kinetics, introduced by the group velocity dispersion. Each single wavelength measurement is, by definition, not affected by the GVD artefact. Nevertheless, when multiple traces at different wavelengths are considered, a temporal shift between them is present.

In single wavelength experiments, the "zero time" is obtained by an initial measurement session of transient spectra in which the delay associated to the maximum of the SRG is identified. Thus we obtain the absolute delay value at which we have temporal coincidence between the pump and the portion of the probe pulse whose wavelength corresponds to the maximum of the SRG. Any portion of the probe pulse peaked at higher wavelengths, will overlap the pump pulse at longer delay. Once the "zero" has been found, the position is kept fixed for the whole single wavelength experiment. Hence the temporal shift between the various kinetics is given by the GVD curve, which has been obtained by means of an *optical kerr effect* experiment

(section 2.4.1).

Table 3.6: Fitting results of single wavelength measurements.

λ_{probe} *(nm)*	$A_2 * 10^{-3}$	τ_2 *(ps)*	$A_3 * 10^{-3}$	τ_3 *(ps)*	*konst* $* 10^{-3}$
405	1.3 ± 0.3 (4.5%)	3 ± 0.5	26.4 ± 0.4 (91.7%)	27 ± 3	-1.1 ± 0.1 (3.8%)
450	1.9 ± 0.3 (10.3%)		14.9 ± 0.4 (80.1%)		-1.8 ± 0.1 (9.7%)
500	1.8 ± 0.2 (29.6%)		2.7 ± 0.3 (45.3%)		-1.5 ± 0.1 (25.1%)
550	–		-0.81 ± 0.2 (53.6%)		-0.7 ± 0.1 (46.4%)

The kinetics traces, corrected for the *GVD*, was then fitted with the *global fitting* method; the results are shown in Table 3.6. In the table only the parameters related to the second and the third exponential function and the value for the *konst* parameter are reported. The first exponential function is indeed associated to the temporal evolution that takes place during the first few hundreds femtoseconds: the delays till $\sim$ 1 ps are affected by the *cross-phase modulation* (XPM) artefact.[48–50] So we did not take into account the transient signal's evolution in this temporal interval for the discussion about the relaxation of excited state population.

3.6 Conclusions

From qualitative analysis of the transient spectra we conclude that the S_1 excited state is directly populated by the excitation pulse. The fluorescence emission shows that a radiative channel, associated to the deactivation of this excited state, is present. The time evolution of the *SE* band is therefore directly related to the depopulation of the S_1 excited state. With the help of the *global fitting* analysis we

found that both the *SE* band and the lower energy *ESA* band have the same temporal evolution and that the kinetic traces are characterized by two main temporal components:

- The faster temporal component ($\tau_2 = 3ps$) is associated with vibrational relaxation in the S_1 potential energy surface.
- The second temporal component ($\tau_3 = 27ps$) is directly related to the depopulation of the S_1 excited state.

So the S_1 is completely depopulated 200 ps after the excitation, but, as shown in figure 3.15, the transient signal does not go to zero (baseline) on the time scale experimentally accessible (maximum delay $\sim 1.8ns$). All the kinetics are indeed characterized, for delays greater than 200 ps, by a constant transient absorption signal (negative values of $-\Delta Abs$). We were not able to appreciate the evolution of this transient absorption: its intensity is constant in the whole inspected temporal window. For this reason we introduced a constant in the molecular response function to account for this contribution.

This behavior can be explained by the presence of a lower energy excited state which is populated during the decay of the S_1 excited state. This means that two channels for the S_1 depopulation are present: a radiative channel, given by the fluorescence emission, and a non-radiative channel. Static and time resolved studies[26,34,35] were carried-out to characterize the behavior of $7H4MC$ and 7-methoxy-4-methylcoumarin ($7Met4MC$) on long time scales (microseconds up-to seconds). All the authors agree that both chromophores are characterized by an excited triplet T_1 state which is populated after the decay of the population from the S_1 excited state.

In particular, De Melo *et al.*[35] performed transient absorption experiment on the microseconds time scale of dioxane solutions of $7H4MC$ and $7Met4MC$. They obtained transient spectra characterized by a broad absorption band which covers the spectral region between 350 525 nm. In Figure 3.16 we show the comparison

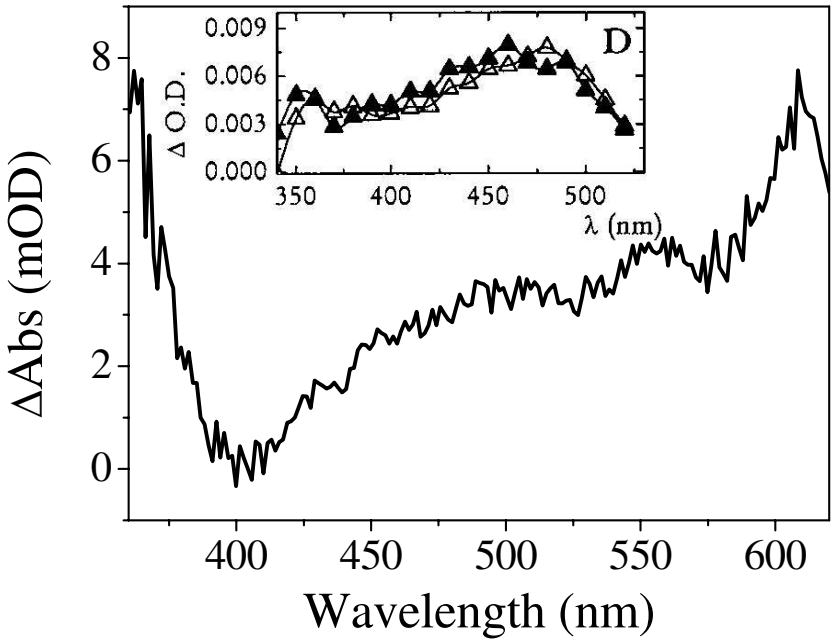

Figure 3.16: (*Full*) Transient spectra of 7HC (*solvent*=CH_3CN) recorded 500 ps after 325 nm excitation with $\sim 0.8\ \mu J$/pulse. (*Inset*) Transient spectra of 7H4MC in dioxane ($-\blacktriangle-$) collected 8 μs and ($-\ \triangle\ -$) 1.5 μs after pump excitation.[35]

between the transient spectrum recorded for 7HC in acetonitrile solution 500 ps after the pump pulse, and the transient spectra recorded by de Melo *et al.*[35] on 7H4MC in dioxane solution 1.5 and 8 μs after excitation. The intensity and the shape of the spectra are quite similar but the 7HC transient spectra is slightly red shifted. $7HC$ and $7H4MC$ belong to the Umbelliferones's family and they are known to be characterized by similar behavior in the ground and exited singlet states.[31] This led us to conclude that the S_1 excited state of 7HC is rapidly ($\tau_3 = 27ps$) depopulated by fluorescence emission (radiative transition) and by inter-system crossing *ISC* towards the first triplet excited state T_1. The evolution of the S_1 excited state is schematically depicted in Figure 3.17, where the vibrational relaxation in the S_1 potential surface is shown.

Now we can calculate the fluorescence lifetime: we know the S_1 lifetime and the fluorescence quantum yield. We know also that the relaxation pathway involves the

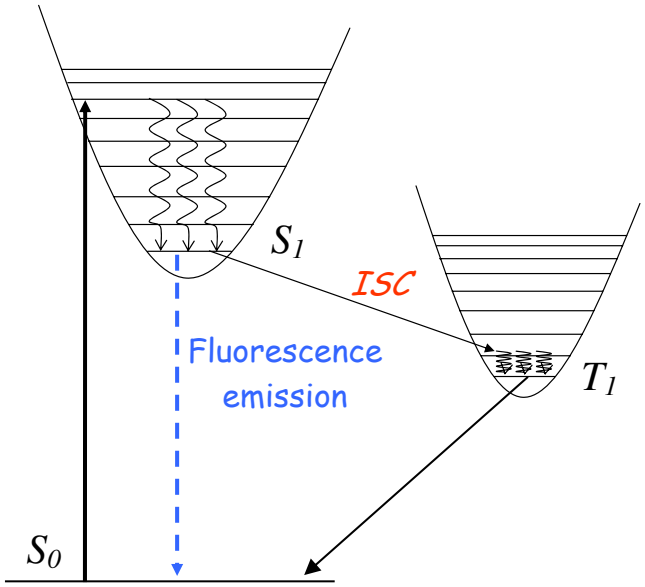

Figure 3.17: Jablonski diagram of 7HC after 325nm pump excitation.

radiative decay (fluorescence emission), the internal conversion (IC) towards S_0 and the inter-system crossing (ISC) towards the T_1 excited state. We can write then the following equation:

$$\Phi_f = \frac{K_f}{K_f + K_{IC} + K_{ISC}} \tag{3.2}$$

where Φ_f is the fluorescence quantum yield, K_f is the rate constant for the spontaneous emission and $K_f + K_{IC} + K_{ISC}$ is the global rate constant for the decay of the emitting S_1 state. We can rewrite equation 3.2 as

$$\Phi_f = \tau_{S_1} * K_f \tag{3.3}$$

where τ_{S_1} is defined as

$$\tau_{S_1} = \frac{1}{K_f + K_{IC} + K_{ISC}} \tag{3.4}$$

and is expressed in *sec*. From equation 3.3 we obtain the following values for K_f

$$K_f = \frac{\Phi_f}{\tau_{S_1}} = \frac{0.0035 \pm 0.0005}{(27 \pm 3) \times 10^{-12}} = (1.3 \pm 0.3) \times 10^8 \, sec^{-1} \tag{3.5}$$

and the fluorescence lifetime given by

$$\tau_f^0 = \frac{1}{K_f} = 8 \pm 1 \, ns \tag{3.6}$$

Once obtained the value of K_f, we can calculate the rate constant associated to the non radiative relaxation channels $K_{nr} = K_{IC} + K_{ISC}$. It is given by

$$K_{nr} = K_{IC} + K_{ISC} = K_f \frac{1 - \Phi_f}{\Phi_f} = (3.7 \pm 0.8) \times 10^{10}\, sec^{-1} \tag{3.7}$$

Chapter 4

1-Hydroxy-2-Methoxy-9,10-Anthraquinone

In this chapter we will focus our attention on the Acceptor unit of the bichromophore compound. The isolated acceptor is virtually an *alizarin* or 1,2-Dihydroxy-Anthraquinone molecule. However, when the acceptor molecule is inserted in the bichromophore unit, it is linked to the molecular bridge by 2-hydroxyl group. Hence, to reproduce the molecular structure that the acceptor has in the bichromophore molecule a modified *alizarin* molecule has been synthesized, substituting the 2-hydroxyl group with the 2-methoxy group.

4.1 Introduction

Anthraquinone and its derivatives are well known chromophores and are employed in many fields due to their optical properties.

Dihydroxyanthraquinones have important applications as a prominent family of pharmaceutically active and biologically relevant chromophores: they are the chromophores of anthracyclines, which are widely used as antibiotics and antitumor drugs.[51–54] In particular 1,2-Dyhydroxyanthraquinone (*Alizarin*-AZ) is the core moiety of adriamycin, an important anti-tumor drug.[55]

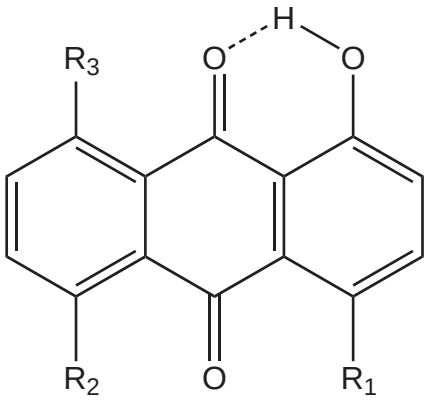

R1= H	R2= H	R3= H	1-HAQ
R1= OH	R2= H	R3= H	1,4-HAQ
R1= H	R2= OH	R3= H	1,5-HAQ
R1= H	R2= H	R3= OH	1,8-HAQ

Figure 4.1: HydroxyAnthraquinone's derivatives

Recently the interests for this class of organic dyes moved also towards other applications: dyes for liquid-crystal displays and sensitizer for titanium dioxide. Huber *et al.*[56] recorded transient absorption spectra of the Alizarin chromophore directly attached to the surface of titanium-doixide (TiO_2) nanoparticles; the goal of this study was the characterization of the Alizarin system as sensitizer for wide band gap semiconductors. Duncan *et al.*[57,58] performed theoretical analysis of the electron injection process from the Alizarin chromophore to the TiO_2 surface; they investigated the coupling by *ab initio* electronic structure calculations and by *ab initio* molecular dynamics simulations.

The context in which we studied and characterized the photophysical properties of the 1-Hydroxy-2-Methoxy-9,10-Anthraquinone derivative is its use in the antenna-like system that we are investigating. We need a full characterization of the photophysical properties of the isolated acceptor molecule if we want to fully understand the efficiency and the temporal evolution of the energy transfer process in the donor-acceptor compound.

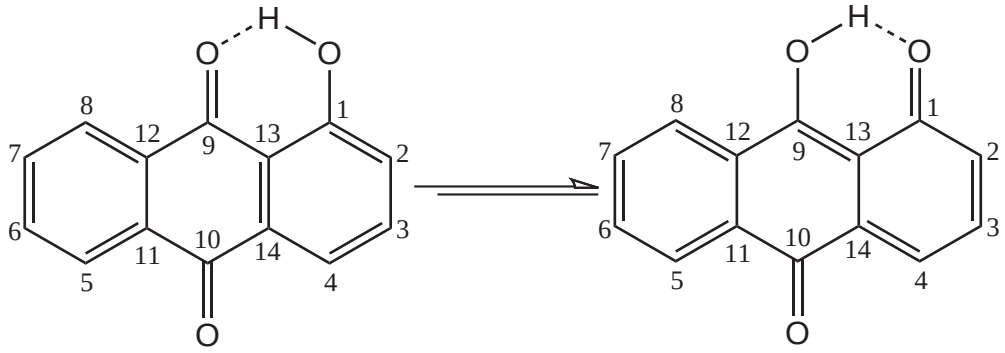

Figure 4.2: Proton transfer reaction for 1-Hydroxyanthraquinone

4.2 Absorption and Emission Spectra

Steady state properties of Hydroxyanthraquinone (HAQ) derivatives has been investigated by several authors with different spectroscopic techniques. One of the most important properties associated to the HAQ is its ability to give rise to intramolecular proton transfer in the excited state. The tautomeric reaction takes place in the S_1 electronic state and only the 9,10 -CO and 1,4,5,8 -OH functional groups are involved in the process (Fig.4.2). The *excited state intramolecular proton transfer* (ESIPT) reaction induces a large change of the electronic configuration of the molecule resulting in dual (normal and tautomeric) emission that, since Weller's studies on methyl salicylate,[59,60] has been used as a marker to identify the ESIPT process. Owing to the ESIPT in the excited singlet-state, an *enol*-tautomer is converted to a *keto*-one (Fig.4.2), and consequently a largely Stokes-shifted fluorescence is observed. The dual emission of some HAQ derivatives in Shpolskii matrix, supersonic jet and solution has been reported by several authors[61–75] and it has been interpreted on the basis of an ESIPT process. A dual emission was observed for 1,5-dihydroxyanthraquinone (1,5-DHAQ)[67,70] and 1,8-dihydroxyanthraquinone (1,8DHAQ *Chrysazin*)[66,71] but not for 1,4-dihydroxyanthraquinone (1,4-DHAQ);[61,69] this is probably due to the greater stability of the six-membered ring formed by the two intramolecular hydrogen bonds respect to the proton-transferred configu-

ration. The dual emission has been observed also for 1-Hydroxyanthraquinone and the presence of ESIPT reaction is confirmed by steady state[68,70] and time resolved measurements.[76,77]

The photophysics and photochemistry of anthraquinone and of its derivatives show interesting features that vary with the substituent group. First, the lowest electronically excited state of the unsubstituted anthraquinone lies in the near UV region ($\sim$ 400 nm) and is of $n\pi^*$ character, with a $\pi\pi^*$ state lying above it. When a substituent group is inserted such as -OH or -NH_2 that donate electrons to the aromatic π system, the energy ordering of these states is reversed so that the $\pi\pi^*$ state becomes the lowest excited state and the absorption edge moves to the visible region. This red shift of the $\pi\pi^*$ transition is commonly attributed to the electron transfer from the electron donating substituent to the π ring, which leaves the $n - \pi^*$ transition virtually unaffected. The optical absorption of substituted anthraquinones progressively shifts to the red as the electron donating capability of the substituent increases. Second, when an -OH group is substituted at a position that allows the formation of an intramolecular hydrogen bond, the excited-state lifetime is considerably reduced. The normalized absorption and fluorescence spectra are shown in

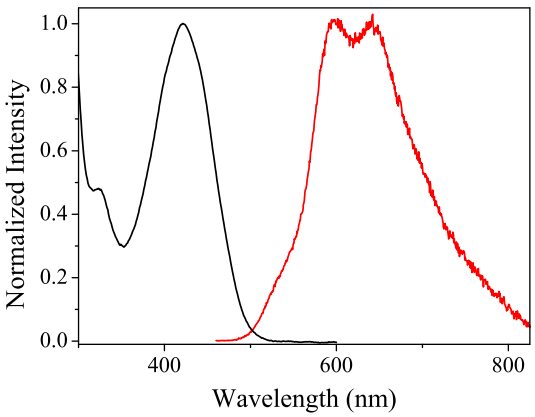

Figure 4.3: Absorption (*black*) and Emission (*red*) spectra (λ_{exc}=400 nm) of 2-metO-1HAQ in acetonitrile.

figure 4.3. The absorption maximum is located at 420 nm with $\varepsilon = 5950\ l * mol^{-1}$ and oscillator strength f=0.113 ± 0.003. The fluorescence emission, following 420 nm excitation, is centered at 620 nm and is characterized by a quantum yield Φ= 0.02 ± 0.003.

4.3 Electronic Structure Characterization

The characterization of ultrafast intramolecular proton transfer reactions by means of *ab initio* calculations allows understanding and to rationalizing the mechanisms of the ultrafast process. Several authors investigated this phenomenon either combining ultrafast transient absorption measurements and *ab initio* calculations,[78,79] with a theoretical approach only[80–87]. It is well known that the proton transfer reaction takes place on a sub-100 fs time scale for hydroxyanthraquinones derivatives;[88,89] the characterization of the excited states potential well is of primary importance to understand this ultrafast process.

4.3.1 Computational Procedure

All calculations were performed with the GAUSSIAN03 program package.[42] In all cases the self-consistent field (SCF) convergence criteria were tightened to, at least, 10^{-9} a.u. and all geometry optimizations were performed until the residual mean force was smaller than 1.0×10^{-5} a.u. (tight threshold in Gaussian). Generally the calculations were performed with the 6-31+G(d,p) basis set; in order to verify the reliability of the obtained results, a larger basis set, 6-311++G(2df,2pd), was used for geometry optimization and to calculate the vertical transitions. The non local three-parameter hybrid exchange B3LYP density functional,[43,44] as implemented in the Gaussian03 package, was employed. The frequencies associated to the vertical ground-to-excited state transitions were calculated by means of the *TD-DFT* method with the above mentioned density functional and basis sets.

For the characterization of the ground state potential surface we employed the

"relaxed (potential energy surface) PES scan" method. The PES scan gives an idea of the shape of the potential well along one particular coordinate (internal or Cartesian). This calculation is based on the choice of a coordinate that is allowed to vary, on the definition of the amplitude of its variation, and the number of steps to be considered. During each step this coordinate is kept fixed (frozen) while the others are free and constitute the variables along which the minimization of the internal and Cartesian gradient is performed. In this way for each step along the selected coordinate the free variables (valence angles, bond distances and dihedral angles) of the molecule are adjusted (relax) to minimize the internal forces with the imposed constraints. The simulation of the reaction coordinate for the proton transfer process was assumed coincident with the distance $R\ H_2 - O_1$ (Figure 4.4). There exist

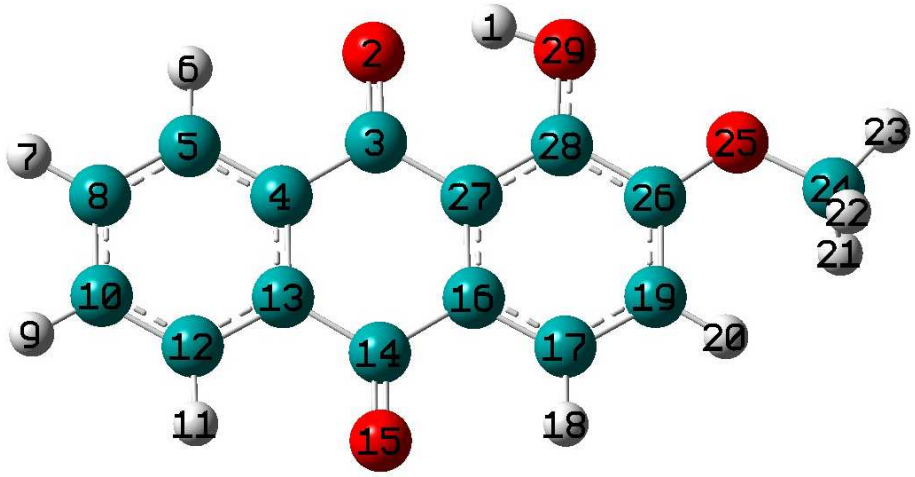

Figure 4.4: *"Ball and Stick"* representation of 2-metO-1HAQ and atom numbering.

a number of different theoretical methods, such as CASSCF, CASPT2, CCSD and TDDFT, which in principle are capable of dealing with proton transfer in a given excited state. However, the large size of the systems precludes an advanced theoretical characterization (CASSCF, CCSD and CASPT2) of the potential energy surfaces of ESIPT. Fortunately, recent calculations[78,79,81,83–85] showed that TDDFT (in partic-

ular with the B3LYP functional) can reliably predict the potential energy surface of ESIPT. In this work, we constructed the potential energy surface (PES) of ESIPT by TD-DFT theoretical calculations of the Franck-Condon vertical transitions for each point of the ground state potential surface.

4.3.2 Ground state properties and Geometry Optimization

Ground state geometry, for the *Enol* form, has been optimized at the DFT B3LYP level of theory with 6-31+G(d,p) and 6-31++G(2df,2pd) basis sets. Selected geometric parameters are collected in table 4.1. The molecule, being essentially composed of the 9,10-Anthraquinone aromatic skeletal, is planar with two of the hydrogen atoms of the methyl group symmetrically disposed above and below the molecular plane. The optimized structures for the *Enol* form correspond to min-

Table 4.1: Calculated selected bond length (Å) and bond angles (A-valence) (degrees) for the ground state geometry (*Enol* form) of 2metO-1HAQ. [(1)]Atom numbering is given in Figure 4.4 .

Name definition[(1)]	*6-31+G(d,p)*	*6-311++G(2df,2pd)*
O(2)-C(3)	1.248	1.239
C(14)-O(15)	1.230	1.220
C(3)-C(27)	1.466	1.463
C(27)-C(28)	1.411	1.405
C(28)-O(29)	1.336	1.331
O(29)-H(1)	0.995	0.991
H(1)...O(2)	1.656	1.655
O(2)-C(3)-C(27)	121.3	121.4
C(3)-C(27)-C(28)	119.1	119.1
C(27)-C(28)-O(29)	122.9	122.9
C(28)-O(29)-H(1)	106.3	106.3
O(29)-H(1)-O(2)	148.0	147.9

ima of the potential surface, as confirmed by the absence of imaginary vibrational

frequencies. Extension of basis set brings in general to the shortening of the bond lengths; in particular, the two carbonyl double bonds are shortened by ~ 0.01 (Å), while the distance O(2)...H(1) is virtually unchanged. The potential energy curve for the proton transfer reaction (GSIPT) in the ground state was calculated by fixing the H(1)...O(2) distance and imposing a constant variation of -0.05 Å starting from the equilibrium values: 1.656 Å *6-31+G(d,p)* and 1.655 Å *6-311++G(2df,2pd)*. For each value of the distance H(1)...O(2) the geometry was optimized by minimizing the gradient in respect to all the "free" geometric parameters. Results are collected in Figure 4.5. The calculation provides the ground state intramolecular

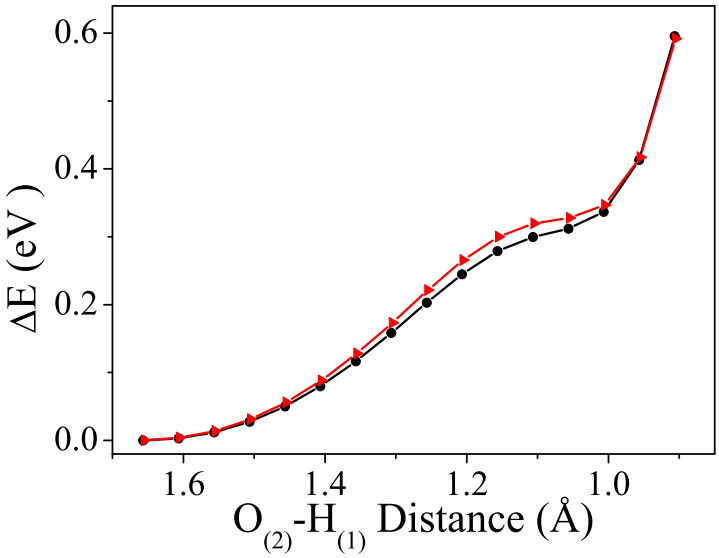

Figure 4.5: GSIPT curves obtained from B3LYP/6-31+G(d,p) (*black*) and B3LYP/6-311++G(2df,2pd) (*red*) optimized structures.

proton transfer curves with a single minimum; the *Keto* form (H(1)...O(2) $\simeq 0.95$ Å) is found about 4 eV ($\sim$9.6 kcal/mol) above the enol form. Extension of the basis sets results in a small increase of the "curvature" of the first part of the potential well, while the relative energy of the keto form is unchanged from the calculation with the 6-31+G(d,p) basis set. The PES curves show the presence of an inflection

at H(1)...O(2)$\simeq$ 1.1 Å; this could indicate the presence of a minimum, unidentified because of the high amplitude of the sampling step. Then we tried to optimize the geometry of a possible intermediate structure, starting from the the keto geometry in the ground state, without any constraint. We performed the calculation with both basis sets and in all cases we obtained the same result: the calculations diverged from the keto form and converged into the enol form. This led us to conclude that there is no intermediate minimum structure between the keto and enol form in the ground state. The only stable structure is the enol form.

4.3.3 Calculation of Vertical Transitions and ESIPT Curve

The vertical excitation energies were calculated at the B3LYP/6-31+G(d,p) and B3LYP/6-311++G(2df,2pd) level of theory. The values obtained for the first singlet transitions of the *enol* form, along with the estimated oscillator strengths, are collected in table 4.2. Extension of the basis set involves an increase of the transition energies (up to $\sim$ 0.06 eV) except for the last excited state, for which a lowering of $\sim$ 0.02 eV is observed. Within the Kohn-Sham approach, the character of each tran-

Table 4.2: TDDFT Vertical excitation energies, in eV and cm^{-1}, and Oscillator strength for the first six singlet excited states of the enol form of 2metO-1HAQ. .

	6-31+G(d,p)				*6-311++G(2df,2pd)*		
state	ΔE (eV)	ΔE (cm^{-1})	f	state	ΔE (eV)	ΔE (cm^{-1})	f
2^1A ($\pi\pi^*$)	2.80	22589	0.14	2^1A ($\pi\pi^*$)	2.83	22833	0.13
3^1A ($n\pi^*$)	2.97	23971	–	3^1A ($n\pi^*$)	2.99	24076	–
4^1A ($\pi\pi^*$)	3.44	27731	0.01	4^1A ($n\pi^*$)	3.48	28069	–
5^1A ($n\pi^*$)	3.46	27918	–	5^1A ($\pi\pi^*$)	3.49	28124	0.01
6^1A ($\pi\pi^*$)	3.83	30911	0.07	6^1A ($\pi\pi^*$)	3.89	31375	0.08
7^1A ($\pi\pi^*$)	3.99	32177	0.03	7^1A ($\pi\pi^*$)	3.97	32029	0.02

sition can be estimated from the coefficient of the orbitals involved in the electron

excitation process. We found that the lowest singlet excited state is of $\pi\pi^*$ character with both basis sets, the transition from the ground to the first singlet excited state being associated to the promotion of one electron from the occupied HOMO (Figure 4.6) to the unoccupied LUMO (Figure 4.7). This is in agreement with the

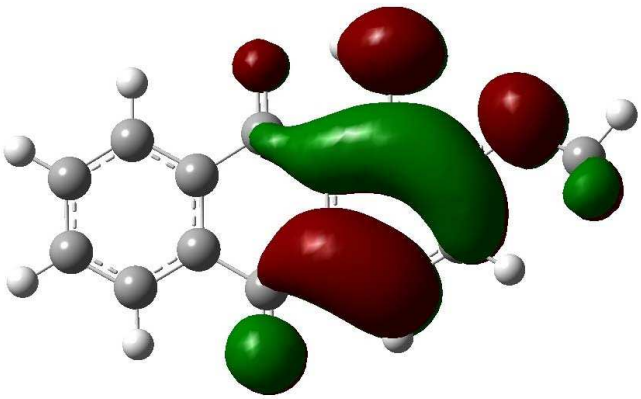

Figure 4.6: HOMO (π) of the *Enol* form of 2metO-1HAQ.

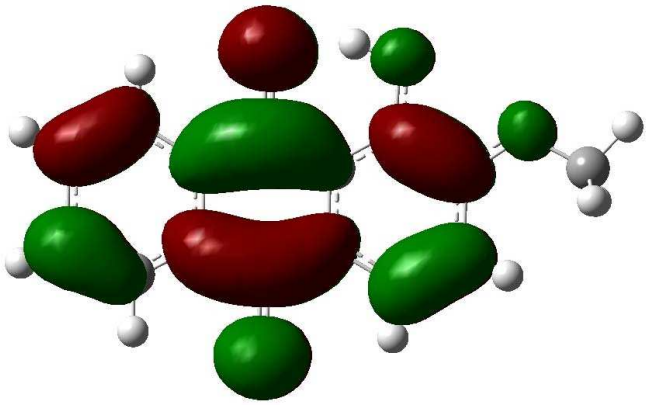

Figure 4.7: LUMO (π^*) of the *Enol* form of 2metO-1HAQ.

findings of Diaz *et al.*[90], who predict a $\pi\pi^*$ character for the first singlet excited state with transition energy in the visible range. Concerning the ordering of higher energy excited states, we observe an inversion between the calculation performed

with 6-31+G(d,p) and with 6-311++G(2df,2pd): 6-31+G(d,p) calculation predicts that the third singlet excited state is a $\pi\pi^*$ state, while 6-311++G(2df,2pd) predicts a $n\pi^*$ state. This is related to the low energy difference between the third and the fourth excited state ($\sim$ 0.01 eV) according to the two calculations. The calculated excitation energies were directly compared with the experimental absorption spectrum recorded in acetonitrile solution. The second derivative of the spectrum allows to better appreciate the maxima of the absorption bands. In Figure 4.8 we reported

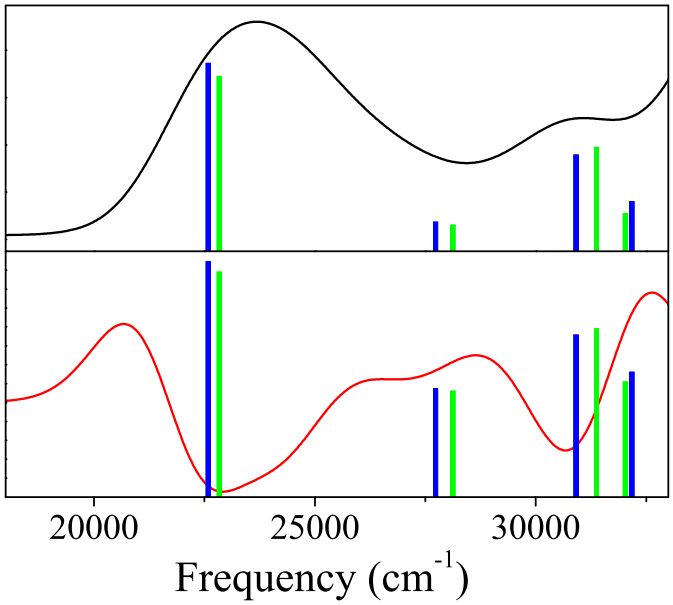

Figure 4.8: Ground state absorption spectrum (*black*), Second derivative of the absorption spectrum (*red*), vertical excitation energies associated to ($\pi\pi^*$) states calculated at B3LYP/6-31+G(d,p) (*blue* bar) and B3LYP/6-311++G(2df,2pd) (*green* bar) level of theory of the *Enol* form of 2metO-1HAQ.

only the ($\pi\pi^*$) transitions, obtaining an excellent agreement with the experimental spectrum. Not significant improvement for the vertical excitation energies of the equilibrium structure of the *Enol* form of 2metO-1HAQ is obtained by extending the basis set. The B3LYP/6-31+G(d,p) method then is to be preferred as it offers a better balance of accuracy and computational time.

We calculated the potential energy curve for the ESIPT reaction in the S_1 excited

state by computing the vertical excitation energies at each point of the GSIPT curves, and by adding the computed values to the relative (in respect to energy of the ground state *Enol* form) energy of each point. We employed 6-31+G(d,p) and 6-311++G(2df,2pd) basis set to further characterize the effect of the basis extension. Results are collected in Figure 4.9, where the ESIPT curves obtained with the

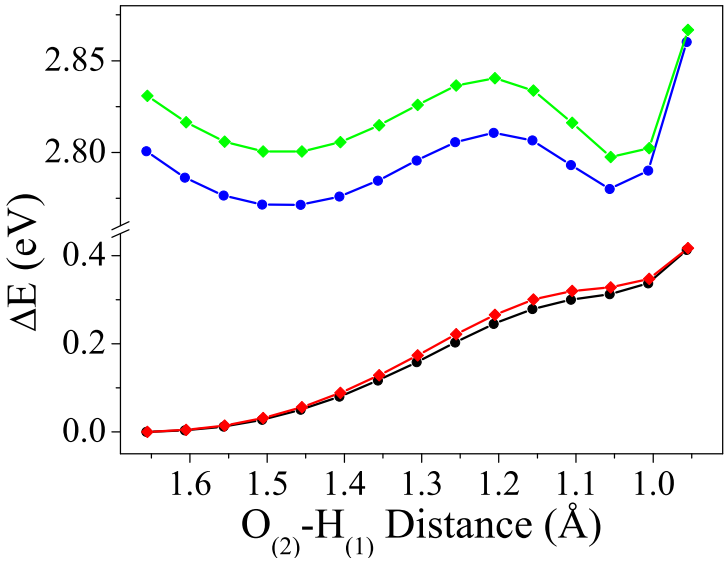

Figure 4.9: GSIPT curves obtained from B3LYP/6-31+G(d,p) (*black*) and B3LYP/6-311++G(2df,2pd) (*red*) and ESIPT curves obtained from TD-B3LYP/6-31+G(d,p) (*blue*) and TD-B3LYP/6-311++G(2df,2pd) (*green*).

two different basis sets are shown. ESIPT curves exhibit a double minimum: the *Enol* excited form has its lowest energy value for H(1)...O(2) $\simeq$ 1.46 Å, while the minimum for the excited *Keto* form is located between 1.06 and 1.01 Å. The calculation with TD-B3LYP/6-31+G(d,p) predicts an ESIPT curve characterized by two minima having almost the same energy (ΔE$\sim$ 0.009 eV) and barrier energy of $\simeq$ 0.04 eV ($\simeq$ 0.91 Kal/mol) in respect to the excited *Enol* form. The ESIPT curve calculated with TD-B3LYP/6-311++G(2df,2pd) is characterized by a global shift towards higher energy. The calculated shift (ΔE $\sim$ 0.03) is comparable, for

values of H(1)...O(2) lower than 1.21 Å, with the shift observed for the excitation energies calculated at the equilibrium *Enol* geometry.

The ESIPT curve calculated with TD-B3LYP/6-31+G(d,p) has two minima, the *Enol* excited form being the lower one. On the contrary, the curve calculated with TD-B3LYP/6-311++G(2df,2pd) exhibits two minima, the *Keto* form being the lower. Also in this case the energy difference between the minima is not so high (ΔE $\sim$ 0.003 eV) and the energy barrier is $\simeq$ 0.04 eV. From this point of view, extension of the basis improves the description of the excited state properties. Indeed, according to the TD-B3LYP/6-31+G(d,p) calculation, the excited *Enol* form is the most stable structure, so that no proton transfer reaction should take place. However, it is necessary to stress that only qualitative results should be expected from calculation of this type. There are two main reasons for this:

1. The GSIPT curve is not the true reaction path, because we impose the reaction coordinate. A better approach should involve the identification of the transition structure and should follow the appropriate reaction coordinate towards the minimum structure. This is not possible in this case, since the ground state *Keto* form is not a minimum and the standard procedure for searching a transition structure fails.

2. The ESIPT curve is calculated from the vertical excitation energies, so that molecular relaxation in the excited electronic state is not allowed.

Anyway, the calculated curves for the excited state proton transfer reaction predict a small ($\simeq$ 0.91 Kal/mol) energy barrier for the transfer process. Furthermore, considering that the calculations were performed in the gas phase and that the energies are not corrected for the ZPVE and for the thermal contribution, the calculated value for the energy barrier is consistent with an ultrafast proton transfer process.

4.4 Transient Absorption Spectra

In this section the transient spectra of 1-hydroxy-2methoxy-anthraquinone will be discussed. We will focus our attention on the temporal evolution of the transient signal and we will extract the main temporal components with the help of Singular Value Decomposition (SVD) analysis. Our goal is the characterization of the temporal evolution of the excited state's population when the acceptor system is directly excited. In order to isolate the temporal dynamics related to the energy transfer process in the bichromophoric compound, we excited the acceptor molecule with two different wavelengths: 400 nm and 325 nm.

400 nm This excitation wavelength is associated with the lowest energy band in the ground state absorption spectrum and promotes the $S_0 \rightarrow S_1$ transition. This is the transition towards the excited state which is directly involved in the proton transfer reaction. The ESIPT is the fundamental event which, in the bichromophoric system, is indirectly promoted by the energy transfer process. Therefore, the characterization of the spectral features related to the ESIPT process in the isolated molecule, along with their temporal evolution, is a fundamental step.

325 nm This excitation wavelength promotes the $S_0 \rightarrow S_1$ transition of the isolated umbelliferone molecule and the transition localized on the donor subunit in the bichromophore. It is essential to characterize the response of the isolated acceptor to this excitation wavelength because this allows us to extrapolate the contribution of the direct excitation in the bichromophoric molecule.

4.4.1 Excitation with 400 nm Wavelength

Ultrafast ESIPT reactions have been studied at femtosecond up to picosecond time scales.[88,89,91–94] The ESIPT process, in this class of compounds, is known to occur within a time scale of few hundreds of femtoseconds or less. For example, the

proton transfer time-constant of 1,8-dihydroxyanthraquinone (1,8-DHAQ) has been reported as shorter than 50 fs[88]. Besides the very fast temporal components (few hundreds of femtoseconds) related to the proton transfer process, additional decay components are frequently reported in the range of several picoseconds and, few tens of picoseconds.[88,93–96] These components are attributed to intramolecular vibrational relaxation and vibrational cooling processes, respectively. Vibrational relaxation is considered to take place in few picoseconds or even sub-picoseconds time scales[93,97–101] meanwhile, the vibrational cooling process proceeds with a time constant of 10-20 ps.[102] The transient signal is also affected by *rotational diffusion* dynamics. A detailed description of the rotational diffusion's effects on time resolved fluorescence and transient absorption signal is reported in appendix B, while below we'll briefly describe the behavior of the chromophore following laser excitation.

Polarized excitation pulse produces orientational selection of the excited molecule (photoselection),depending on the scalar product between the polarization direction and the orientation of the chromophore transition dipole. During the delay time between the absorption of the pump's photons and the absorption of probe's photons, the molecules in solution are subjected to translations and then collisions between molecules, including the solvent ones and to vibrational and rotational dynamics. Molecular rotations (*rotational diffusion*) modify the component of the electric dipole moment projected onto the electric field of the probe pulse. If the scalar product between the molecular dipole moment and the electric field changes then the transition probability rate will change too. Equation B.30 is the *Fermi golden rule* and it is valid also for absorption and stimulated emission from an excited state. The intensity of the transient signal is therefore related to the mutual orientation between the molecular dipole moment of the excited state and the probe's electric field.

Let's consider for a moment the distribution probability function depicted in Figure B.6. This distribution function tell us that the highest transition probability, for a single immobile molecule, is associated to the molecules whose transition

dipole moments are oriented parallel to the excitation beam's polarization. If the dipole moment of the excited state was identical to the ground state one, then this function would represent the distribution of excited state's electric dipole moments (as a function of angle θ and ϕ). The result would be a symmetrical distribution around z-axes. The probability distribution function is a randomly oriented solution is obtained by weighting the transition probability distribution by the probability that the orientation of the transition dipole moment of a molecule is comprised between θ and $\theta + d\theta$. The result (Equation B.35) is the distribution function of the molecules excited by a vertically polarized infinitely short pulse (δ-type pulse). This distribution probability is again symmetrical around the z-axes. Both distribution functions well represent the case of a molecule, whose ground and excited state electric dipole moment are parallel, inside a rigid medium like a vitrified solution.

In general, the dipole of the excited state is not parallel to that of the ground state. Therefore the distribution function for the excited state dipole moment will not be symmetrical around the z-axes, the axes of symmetry will be tilted respect to the z-axes of an angle α, where α is the angle between the ground and the excited state electric dipole moment.

In solution the molecules are subjected, as already noticed, to random rotational motions. If the molecules can rotate freely during the excited state lifetime the symmetrical distribution of the orientation of the electric dipole moments is lost. The preferred orientation of molecules resulting from photoselection at time zero is indeed gradually lost due to the rotational Brownian motion. This process eventually causes the complete loss of preferential orientation, resulting in a randomly oriented excited state population. In section B.3.1 we derive equation B.46 which describes the effect of the rotational diffusion on the anisotropy r, showing that $r(t)$ depends on the *orientation autocorrelation function* (Equation B.47).

The description of the events which follow the excitation of the sample by the pump beam is fundamental to understand the initial temporal evolution of the transient signal. In general the parallel ($\parallel$) and the perpendicular ($\perp$) transient signal

have differen intensities and different time evolutions. Usually the parallel component has a greater intensity respect to the perpendicular one. This is because the pump photoselection results in a higher excited state population of molecules whose dipole moments are oriented close to the pump polarization (see section B.2.3). The parallel component initially decays more rapidly than the horizontal component. This occurs because the population of vertically oriented excited chromophores decays by two mechanisms: the excited state population decay (lifetime τ) and the rotational randomization (angular correlation time τ_c). The same processes act in opposite directions on the decay of the horizontal component: the repopulation of the horizontally oriented excited molecules compensate the energy decay, making the overall decay slower.

Hereafter we define $A_{\parallel}(\lambda, t)$ as the transient absorbance acquired when pump and probe are parallel, while $A_{\perp}(\lambda, t)$ the transient absorbance for perpendicular pump and probe.

4.4.1.1 Parallel and Perpendicular Transient Spectra

Following the same strategy of Choi *et al.*[76] we recorded the transient absorption spectra for parallel ($\parallel$) and perpendicular ($\perp$) polarization geometry of the the 400 nm pump and the white light probe pulses. The 400 nm pump wavelength was obtained from second harmonic generation of the regenerative amplifier's output (frequency = 800 nm and power $\sim$ 600 mW). The pump polarization was controlled by a $\lambda/2$ waveplate, and that of the white light probe was established by means of a suitably oriented polarizer (vertical polarization). Transient spectra of 2metO-1HAQ are characterized, both in parallel and perpendicular polarization configurations, by an excited state absorption (*ESA*) and a stimulated emission (*SE*) band centered at 508 nm and 600 nm respectively. The spectra were corrected for the *group velocity dispersion (GVD)* of the probe pulse and the *GVD* curve has was obtained from an *optical Kerr effect* experiment on the same 2metO-1HAQ solution employed in the transient absorption experiment. The *GVD* corrected spectra are

shown in Figure. 4.10 and 4.11. In the following we will discuss separately the evolution of the transient spectra during the first hundreds of femtoseconds after the photo-excitation, and that in the picosecond time scale.

The spectrum recorded at the temporal coincidence of pump and probe pulses (the red spectrum in the *left* panel of Figure 4.10 and 4.11) shows, for the parallel and perpendicular configuration, the presence of the stimulated raman gain (*SRG*) bands and a broad absorption band.

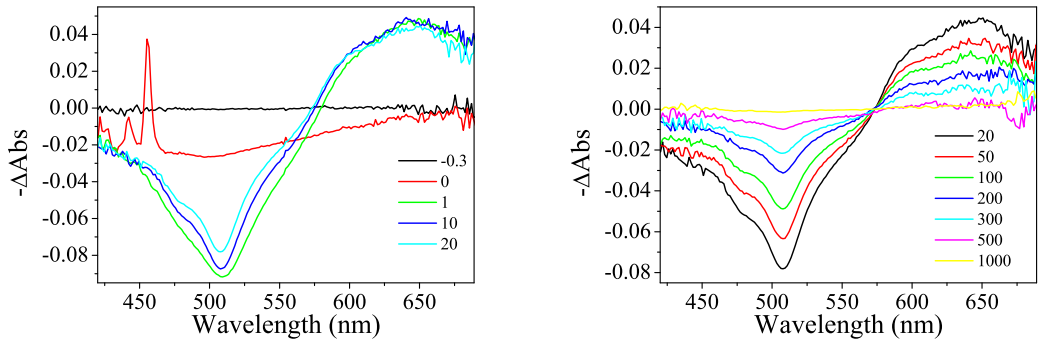

Figure 4.10: Transient spectra recorded after 400 nm pump excitation ($\sim$ 0.5 μJ pulse), with $\parallel$ polarization (delays in ps), of a solution of 2metO-1HAQ (*solvent*=CH_3CN, $Abs_{400nm} \simeq 1$).

The stimulated raman scattering process (*SRS*) involves vibrational levels of the solvent and it is observed only at the temporal coincidence between the pump and the probe pulses. The SRG bands of the transient spectrum of figure 4.10 and figure 4.11, corresponding to the *C-H stretching* of Acetonitrile are centered around 455 nm and 440 nm. The *SRS* effect was employed for the characterization of the instrumental function (cross-correlation function between pump and probe pulse) and for the determining the "zero time" of the experiment, by evaluating the area under the 455 nm *SRG* band of the transient spectra. The delay of the spectrum corresponding to largest area was then identified and taken as the "zero time" of the experiment. The instrumental function was estimated by fitting, with a gaussian-type function, the curve obtained by plotting the area of the SRG band versus the

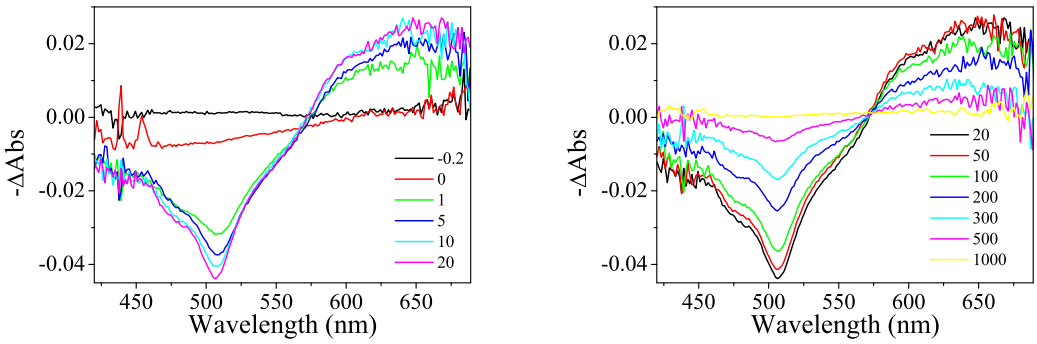

Figure 4.11: Transient spectra recorded after 400 nm pump excitation ($\sim$ 0.5 μJ pulse), with $\perp$ polarization (delays in ps), of a solution of 2metO-1HAQ (*solvent*=CH_3CN, $Abs_{400nm} \simeq 1$).

delay time. The resulting instrumental function has a *FWHM* of 200 fs.

The broad absorption band is the result of the sum of two different contributions:

- the *cross-phase modulation (XPM)* effect[48–50]
- the growth of the *ESA* (508 nm) and *SE* (600 nm) bands.

The artefact introduced by cross-phase modulation is represented, in the frequency domain, by spectral features having a dispersive shape. Lorenc *et al.*[50] described and analyzed the spectral features associated to the *XPM*. The spectra were obtained by 400 nm excitation with a $\sim$ 100 fs FWHM pulse of a 2.5 mm thick cell containing pure acetonitrile. They reported the spectra recorded at increasing delay times without any correction for the group velocity dispersion. The intensity of the spectral features is greater in the absorption direction (negative values of $-\Delta Abs$) and for high frequencies. If the correction for the group velocity dispersion is applied to the signal, the result is a broad absorption band (because the intensity in the direction of negative $-\Delta Abs$ values is greater) whose intensity decreases in the direction of long wavelengths. The presence of the *XPM* is a limiting factor in the analysis of the temporal evolution of the transient spectra, that prevents us from extracting

the real evolution of the excited state population during the first few hundreds of femtoseconds after the photo-excitation.

In the first thirty picoseconds a different time evolution for $A_{\parallel}(\lambda, t)$ and $A_{\perp}(\lambda, t)$ is evident from Figures 4.12 and 4.13. The transient signal $A_{\perp}(\lambda, t)$ is characterized by a slower rise-time respect to $A_{\parallel}(\lambda, t)$. During this time interval the decay of $A_{\parallel}(\lambda, t)$ is already appreciable, while the transient signal $A_{\perp}(\lambda, t)$ is still growing-up. This effect can not be related only to the contribution of the rotational diffu-

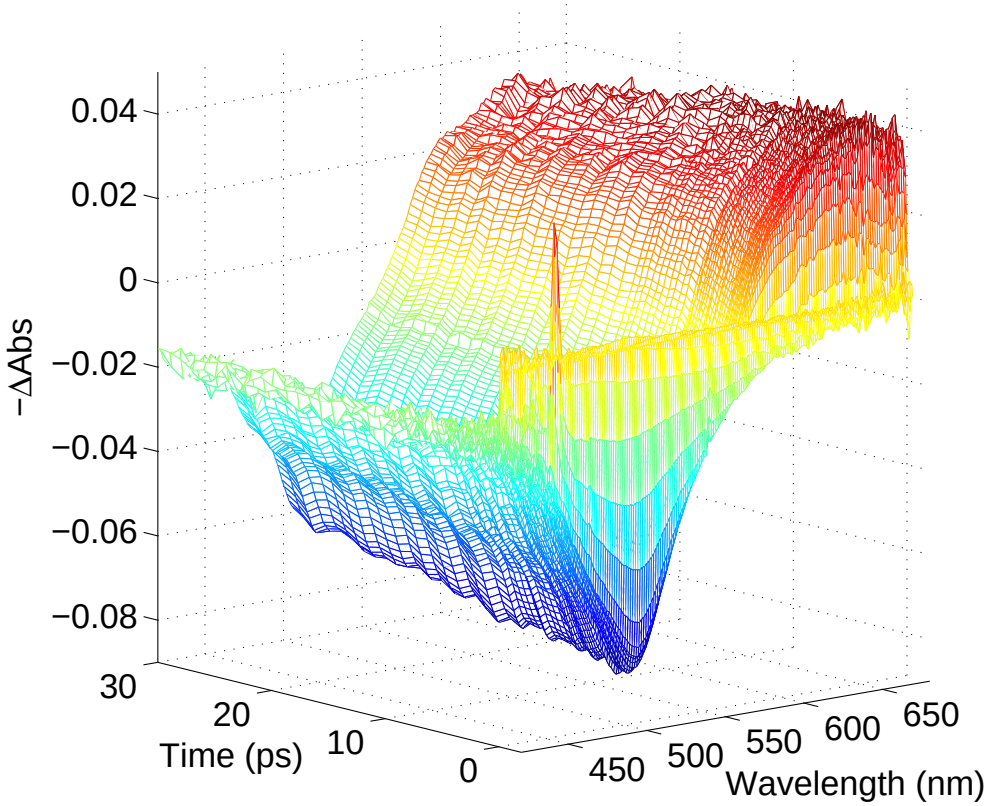

Figure 4.12: Transient spectra (the first thirty picoseconds) recorded after 400 nm pump excitation ($\sim 0.5\ \mu$J pulse), with $\parallel$ polarization, of a solution of 2metO-1HAQ (*solvent*=CH_3CN, $Abs_{400nm} \simeq 1$).

sion. In the introduction section we noticed that $I_{\perp}(\lambda, t)$ usually decays slower than $I_{\parallel}(\lambda, t)$ because of the repopulation of the perpendicular orientation. The evolution

of $A_{\perp}(\lambda, t)$ is, instead, characterized by a slow rise-time. This means that another contribution is superimposed to the rotational diffusion dynamic. The *left* panel of Figure 4.10 and Figure 4.11 shows a different shape of the *ESA* band between the transient spectra recorded 1 ps and 20 ps after pump excitation. The *ESA* band

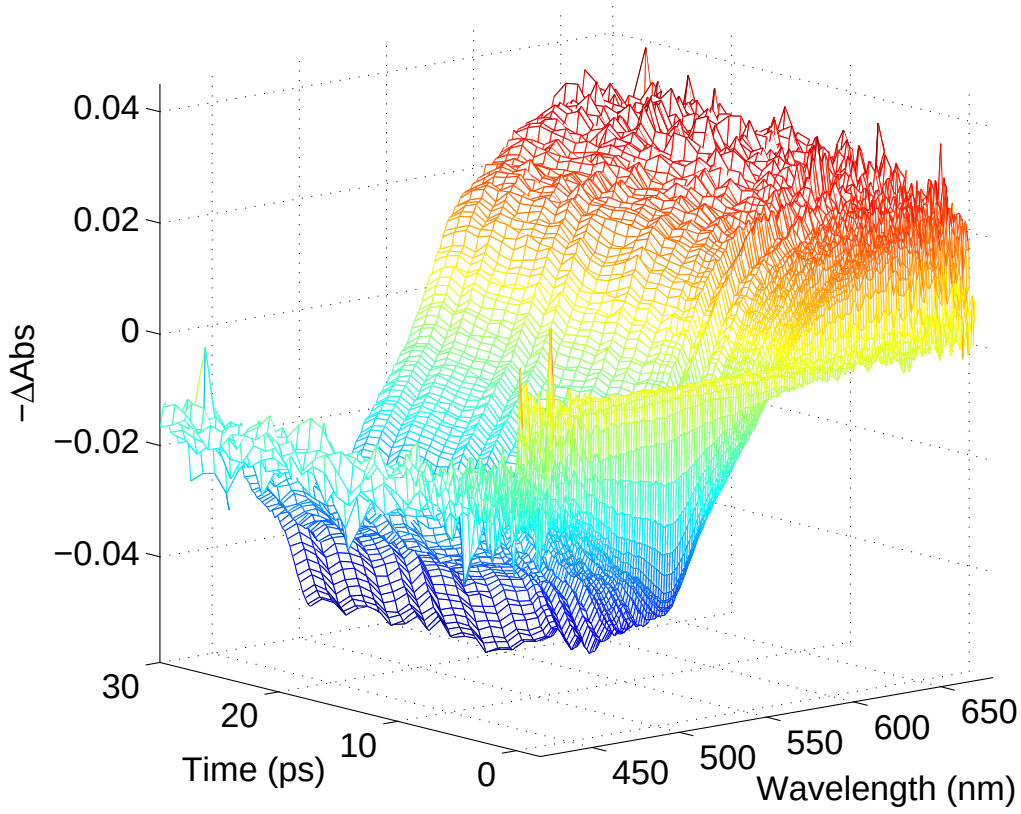

Figure 4.13: Transient spectra (the first thirty picoseconds) recorded after 400 nm pump excitation ($\sim 0.5\ \mu$J pulse), with $\perp$ polarization, of a solution of 2metO-1HAQ (*solvent*=CH_3CN, $Abs_{400nm} \simeq 1$).

is broader and its structure is less pronounced in the spectra recorded at 1 ps respect to the spectra recorded at 20 ps. This is the consequence of the vibrational relaxation. The electronic population is localized on excited vibrational levels of the S_1 state after the excitation event (Franck-Condon principle). The excess of vibrational energy is then redistributed on the various normal modes or dissipated

trough collisions with the solvent molecules. The final result of vibrational relaxation is anyway the Boltzman distribution of vibrational population centered on the lowest vibrational level of each normal mode.

The vibrational relaxation involves changing of the Franck-Condon factors associated to the transitions from the excited state and, consequently, of the intensity and the shape of the bands of the transient spectrum. Typical effects of the vibrational relaxation are narrowing and intensity increase of the transient absorption and stimulated emission bands; a *blue shift* of the band maximum is commonly observed too. The spectra reported in the *left* panel of Figures 4.10 and 4.11 are characterized by this behavior, even if the global evolution is affected by the rotational contribution.

The spectra recorded at higher delay time are shown in Figures 4.14, 4.15 and in the *right* panel of Figures 4.10 and 4.11. The decay of the transient signal in this temporal region is mainly due to the electronic relaxation, and the difference between the parallel and perpendicular evolution is not appreciable in a qualitative analysis of the transient spectra.

In order to extrapolate the temporal components related to the rotational diffusion, we evaluated the anisotropy evolution $r(t)$ and the transient absorbance evolution for the magic angle condition $A_{ma}(\lambda, t)$ by means of the following relations (Appendix B.2.2.1)

$$r(\lambda, t) = \frac{A_{\parallel}(\lambda, t) - A_{\perp}(\lambda, t)}{A_{\parallel}(\lambda, t) + 2A_{\perp}(\lambda, t)} \tag{4.1}$$

$$A_{ma}(\lambda, t) = \frac{1}{3}(A_{\parallel}(\lambda, t) + 2A_{\perp}(\lambda, t)) \tag{4.2}$$

4.4.1.2 Anisotropy Evolution

The first hundreds of femtoseconds after pump excitation are characterized by the *XPM* effect and then we disregarded the evolution of anisotropy during this time interval.

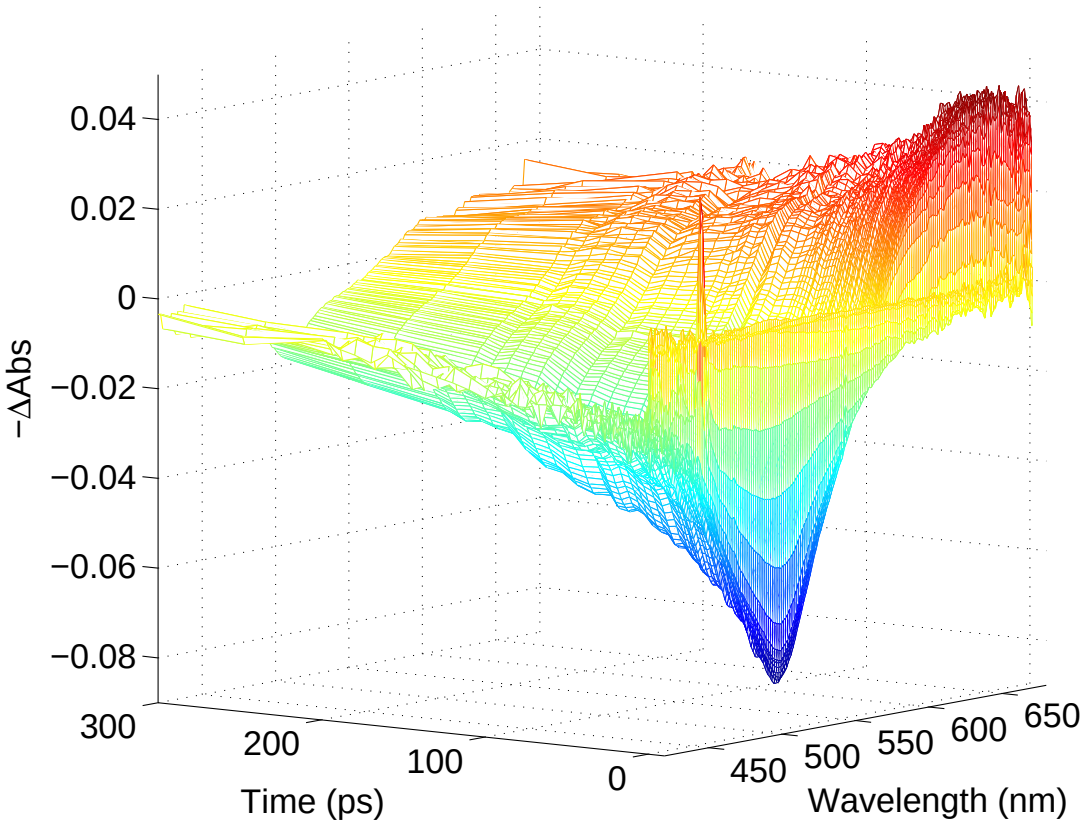

Figure 4.14: Transient spectra (the first three-hundred picoseconds) recorded after 400 nm pump excitation ($\sim$ 0.5 μJ pulse), with $\parallel$ polarization, of a solution of 2metO-1HAQ (*solvent*=CH_3CN, $Abs_{400nm} \simeq 1$).

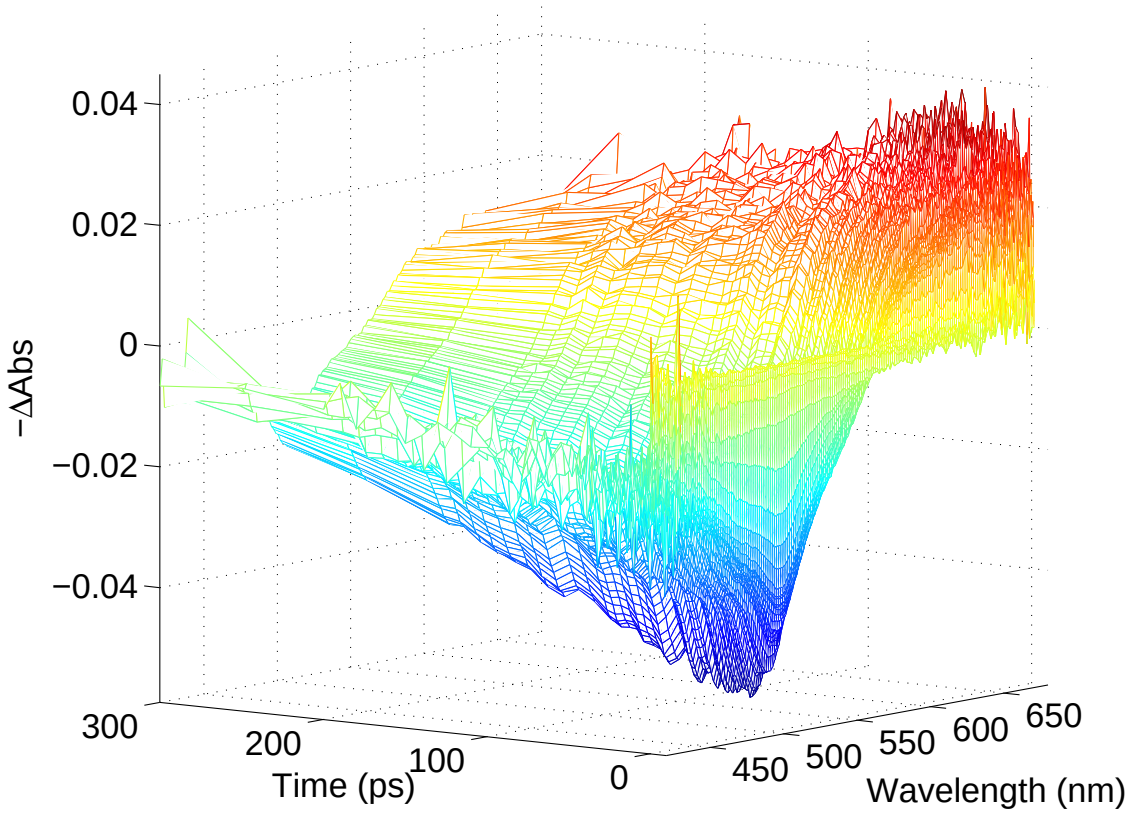

Figure 4.15: Transient spectra (the first three-hundred picoseconds) recorded after 400 nm pump excitation ($\sim$ 0.5 μJ pulse), with $\perp$ polarization, of a solution of 2metO-1HAQ (*solvent*=CH_3CN, $Abs_{400nm} \simeq 1$).

The evolution of anisotropy, shown in Figure 4.16, is reproduced by a single exponential functio:

$$r(t) = r_0\, e^{-t/\tau} \tag{4.3}$$

The fitting procedure gives a time constant $\tau = 18 \pm 2\, ps$ and $r_0 = 0.34 \pm 0.01$. As described in Appendix B, the time dependence of fluorescence and transient absorption anisotropy is related to the rotational motions of molecules. Under condition of "free rotation" (no constraints imposed by the surrounding medium) the time dependence of the orientational autocorrelation function (Equations B.46 and B.47) can be calculated with the Brownian rotational diffusion model. This model was developed originally by Debye and later reconsidered in a hydrodynamic approach by other authors.[103–111] In section B.3.1.1 the equation for Brownian diffusion of a spherical particle is solved. The result is that the rotational correlation time τ is related to the diffusion coefficient D by the relation

$$\tau = (6\, D)^{-1} \tag{4.4}$$

In the hydrodynamic framework, according to the *Debye-Stokes-Einstein* relation, the diffusion coefficient for a spherical particle is inversely proportional to the shear

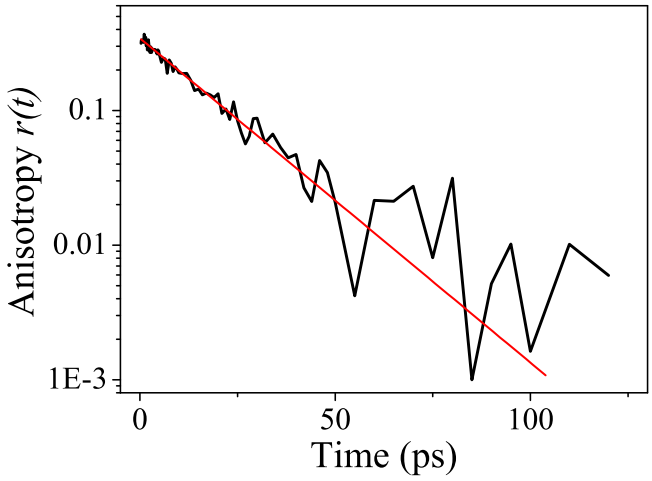

Figure 4.16: 2met-1HAQ anisotropy decay.

viscosity η and to the volume V of the particle:

$$D = \frac{K\,T}{6V\eta} \tag{4.5}$$

where K is the Boltzmann constant and T is the absolute temperature. A general rotating molecule is usually not symmetric about any axes. Such a totally unsymmetric shape can only be described by the shape itself. In order to simplify the treatment of such systems a usual assumption is to describe the molecules as a *general ellipsoid*. The *inertia* of a general ellipsoid is described by the second-rank tensor $\mathbb{I}$. A suitable choice of the reference system (*inertia reference system*) reduces the tensor to diagonal form and the *principal axes* intersect in the center of mass. The *principal inertia moment*, calculated along the three axes of the *inertia reference system*, are the diagonal value of the reduced inertia tensor I: I_a,I_b and I_c. For a generic ellipsoid we have $I_a \neq I_b \neq I_c$ and, by convention, $I_a \leq I_b \leq I_c$. Hence a general ellipsoid has three unequal axes a, b, c and the length of these axes is proportional to the inverse square root of the inertia moment for the rotation about that axes:

$$I_\alpha = \sum_i m_i r_{\alpha i}^2 \Rightarrow L_\alpha \propto \frac{1}{\sqrt{I_\alpha}} \tag{4.6}$$

Under the assumptions of this models the complete reorientation process can be characterized by a diffusion tensor $\mathbb{D}$. In the most general case it can be reduced to a diagonal form, with three independent diagonal elements D_a, D_b, and D_c, characterizing the orientational motion around the three principal axes. The solution of the diffusional equation for a general ellipsoid (complete asymmetric rotor), within the framework of hydrodynamic theory, leads to an autocorrelation function which decays with five apparent correlation times. The correlation times are obtained from appropriate combinations of the diagonal elements of the diffusion tensor $\mathbb{D}$.

$$\tau_{1,2,3} = \frac{1}{3D + 3D_{a,b,c}} \qquad \tau_4 = \frac{1}{6D + 2\Delta} \qquad \tau_5 = \frac{1}{6D - 2\Delta} \tag{4.7}$$

where

$$D = (D_a + D_b + D_c)/3 \qquad \Delta = (D_a^2 + D_b^2 + D_c^2 - D_aD_b - D_aD_c - D_bD_c)^{1/2} \tag{4.8}$$

If the absorption and emission transition dipole moments are directed along one of the principal axes, the number of correlation times reduces to three.

Often the molecules are not treated as completely generic ellipsoid but as axially symmetric ellipsoid (or *ellipsoid of revolution*). The *true symmetric top* molecules are characterized by two equal moment of inertia; this property is shared by all the molecules having at least three-fold rotation symmetry or two-fold rotation axes. There are two types of symmetric tops:

Prolate: The unique moment of inertia is the smallest: $I_a < I_b \equiv I_c$

Oblate: The unique moment of inertia is the largest: $I_a \equiv I_b < I_c$

The *Prolate* and *Oblate* ellipsoid are, usually, characterized by their axial ratio ρ defined as the ratio between the length of the semi-axes of symmetry (unique axes) and the length of the perpendicular semi-axes; hence $\rho > 1$ for a Prolate ellipsoid and $\rho < 1$ for an Oblate ellipsoid.

Because the diagonal elements of the diffusion tensor along the axes perpendicular to the unique axes are equal, the equations for the correlation times reduce to three (regardless the orientation of the transition dipole moments):

$$\tau_1 = \frac{1}{D_\parallel + 5D_\perp} \qquad \tau_2 = \frac{1}{4D_\parallel + 2D_\perp} \qquad \tau_3 = \frac{1}{6D_\perp} \tag{4.9}$$

The evolution of anisotropy $r(t)$ can be expressed as the sum of three exponential decays:

$$r(t) = r_1 \exp(-t/\tau_1) + r_2 \exp(-t/\tau_2) + r_3 \exp(-t/\tau_3) \tag{4.10}$$

The amplitudes of the exponential functions, $r_i(t)$, are given by:

$$r_1 = 0.3 \, \sin 2\beta_A \, \sin 2\beta_E \, \cos \xi \tag{4.11}$$

$$r_2 = 0.3 \, \sin^2 \beta_A \, \sin^2 \beta_E \, \cos 2\xi \tag{4.12}$$

$$r_3 = 0.1 \, (3\cos^2 \beta_A - 1) \, (3\cos^2 \beta_E - 1) \tag{4.13}$$

where β_A and β_E are, respectively, the angle formed by the absorption transition dipole moment and the emission transition dipole moment in respect to the unique

axes; ξ is the angle between the projections of the two former vectors in the plane perpendicular to the symmetry axes.[112]

Several theories[103–109] have been developed to link the orientational diffusion coefficients $D_{\parallel}$ and $D_{\perp}$ to few solvent's parameter. Starting from the *Debye-Stokes-Einstein* relation for a spherical particle, the first step is the introduction of suitable coefficients which take into account the non spherical shape of the molecule and the interaction of the tagged molecule with the "solvent" (in neat liquids the "solvent" consists of the non tagged molecules). The simplest way is to define an *effective Volume* of the molecule:

$$V_{eff} = (f \cdot C)V_m \tag{4.14}$$

where V_m is the real molecular volume, f is the *friction coefficient* (its value is defined by the molecular shape), and C depends on the interaction of the probe molecule with the solvent (boundary conditions). In this way we can rewrite the Einstein relation as:

$$(D_\alpha)^{-1} = \frac{6\,\eta\,V_m\,(f_\alpha\,C)}{KT} \tag{4.15}$$

When $f \cdot C$=1, the hydrodynamic theory reduces to the *Debye-Stokes-Einstein* model. The simplest approach to determine the values of f and C assumes the solvent as a hydrodynamic continuum. The solute molecule moves in a uniform, unstructured medium, characterized by the shear viscosity η. For molecules that can be described as an *ellipsoid of revolution*, characterized by an axial ratio ρ, Perrin[103,113,114] proposed the "stick" boundary conditions $C = 1$ and $f_{stick} = f(\rho)$. The model was adapted by Hu-Zwanzig[105] to the "slip" boundary conditions, by the simple relation $(f \cdot C)_{slip} = (f \cdot C)_{stick} \cdot H(\rho)$. A detailed description of the two limit boundary conditions is given in appendix B.3.2. According to the Perrin's model, the friction coefficients can be determined as:

$$f^{\parallel}_{stick} = \frac{2}{3}\,\frac{(\rho^2-1)}{\rho(\rho - S)} \tag{4.16}$$

$$f^{\perp}_{stick} = \frac{2}{3}\,\frac{(\rho^4-1)}{\rho[(2\rho^2-1)S - \rho]} \tag{4.17}$$

where the value of parameter S depends on the type of ellipsoid:

Prolate: $\rho > 1$

$$S = (\rho^2 - 1)^{-1/2}\ ln[\rho + (\rho^2 - 1)^{1/2}] \tag{4.18}$$

Oblate: $\rho < 1$

$$S = (1 - \rho^2)^{-1/2}\ tan^{-1}[(1 - \rho^2)^{1/2}/\rho] \tag{4.19}$$

Dote and Kivelson[109] introduced the following empirical relation for the friction coefficient $f^{\perp}$ of ellipsoids of revolution, under "slip" boundary conditions:

$$f^{\perp}_{slip} = f^{\perp}_{stick}\,[1 - (f^{\perp}_{stick})^{-2/3}] \tag{4.20}$$

In this model the empiric formula is applied only for the diffusion around the perpendicular axes, i.e for pure *tumbling* diffusion. They found that, for prolate ellipsoids, the diffusion coefficients around the symmetry axes, i.e. pure *spinning* diffusion, can be reasonably approximated by the Perrin's formula (Equation 4.16) with stick boundary conditions.

We performed our anisotropy measurement, we utilized $\eta = 0.38 \times 10^{-3}\ Kg\, m^{-1}\, s^{-1}$ as shear viscosity parameter for acetonitrile. We evaluated the molecular volume and the axial ratio ρ by means of an *ab initio* DFT calculation at B3LYP/6-31+G(d,p) level of theory. We obtained $V_m \simeq 301\text{Å}^3$ and, approximating the molecule to a *Prolate* ellipsoid of revolution, we obtained $\rho \simeq 2$. In figure 4.17 the "tube" representation of 2metO-1HA, along with the cartesian axes used for the *ab inito* calculation, is shown. The orientation of the calculated inertia reference system has been obtained by the following diagonalization matrix:

$$\begin{pmatrix}\mathbf{a} & \mathbf{b} & \mathbf{c}\end{pmatrix} = \begin{pmatrix}\mathbf{X} & \mathbf{Y} & \mathbf{Z}\end{pmatrix} \cdot \begin{pmatrix} 0.99992 & -0.01288 & 0.00000 \\ 0.01288 & 0.99992 & 0.00000 \\ 0.00000 & 0.00000 & 1.00000 \end{pmatrix} \tag{4.21}$$

The symmetry axes **a** forms an angle of $\sim 1^{\circ}$ in respect to the x axes represented in figure 4.17. Absorption transition dipole moment was calculated by means of the

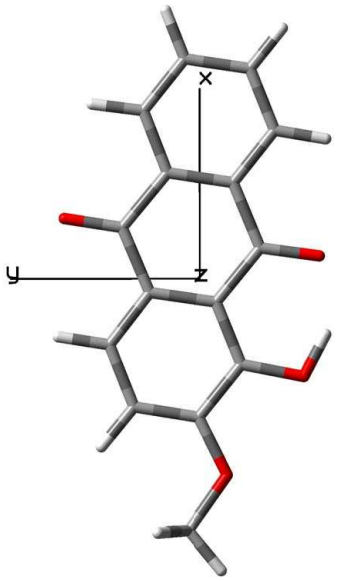

Figure 4.17: Reference axes.

Time Dependent Density Functional Theory method at the B3LYP 6-31+G(d,p) level of theory. A detailed discussion about the results obtained by this calculation are presented in section 4.3.3. The coordinates of the transition dipole moment, in respect to the reference axes shown in figure 4.17, are

$$\mu_{if}^{Abs} = \begin{pmatrix} -1.4299 \\ -0.2237 \\ 0.0000 \end{pmatrix} \tag{4.22}$$

The absorption transition dipole moment lies in the xy plane, it is oriented in the negative x direction with an angle in respect to the inertia axes **a** is of $\sim 8°$. We were not able to perform the geometry optimization in the S_1 excited state. Indeed the *TDFT* algorithm implemented in the GAUSSIAN03 package[42] did not include *analytic gradients* and the numeric solution of the *minimum search problem* is constrained to a limited number of geometric parameters. Hence we could only calculate the terms in respect to β_A in equation 4.13, obtaining the following estimate for the

parameters r_i:

$$r_1 \simeq (8.42 \times 10^{-2}) \sin 2\beta_E \cos \xi \tag{4.23}$$

$$r_2 \simeq (6.08 \times 10^{-3}) \sin^2 \beta_E \cos 2\xi \tag{4.24}$$

$$r_3 \simeq (0.2)\,(3\cos^2 \beta_E - 1) \tag{4.25}$$

Within the "slip" boundary conditions, we used Equation 4.15 for the calculation of $D_\parallel$ and $D_\perp$. We evaluated the friction coefficient for the spinning motion by means of equation 4.16, while the friction coefficient for the tumbling motion, obtained from equation 4.17, was corrected for the slip-type boundary condition making use of equation 4.20. The correlation times were calculated from equations 4.9:

$$\tau_1 = \frac{1}{D_\parallel + 5D_\perp} \simeq 16\,ps$$
$$\tau_2 = \frac{1}{4D_\parallel + 2D_\perp} \simeq 20\,ps$$
$$\tau_3 = \frac{1}{6D_\perp} \simeq 16\,ps$$

We can reasonably assume that the calculated evolution of the anisotropy decay is dominated by the third term of equation 4.25; this means that the loss of anisotropy is mainly determined by an almost pure *tumbling* motion and that the calculated correlation time ($\tau_3 \simeq 16\,ps$) is in good agreement with the experimental one.

4.4.1.3 Magic-Angle Transient Spectra

In figure 4.18 we report the transient spectra obtained by means of Equation 4.2 and corrected for the group velocity dispersion. The *left* panel shows the spectral evolution during the first twenty picoseconds. The spectrum associated to the "zero" of the experiment is characterized by the same shape as the spectra acquired, at the same delay, in parallel and perpendicular polarization. The first hundreds of femtoseconds are indeed dominated by the *XPM* dynamics.

In the following twenty picoseconds the contribution due to the vibrational relaxation is clearly detected. The 20 ps spectrum (Fig. 4.18, *left* panel) shows the

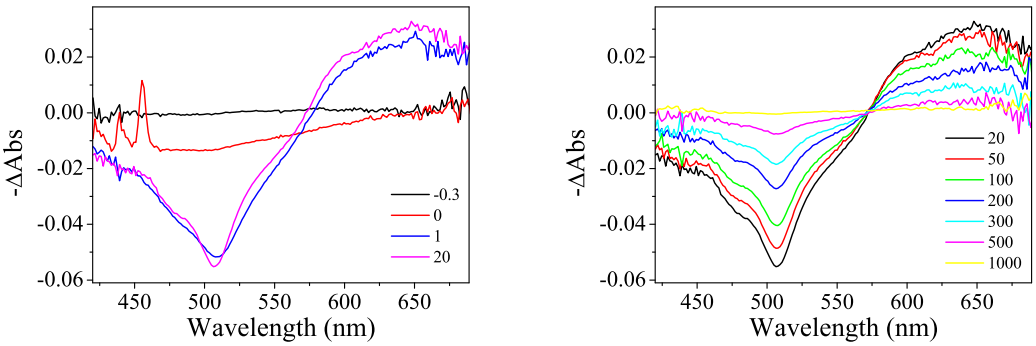

Figure 4.18: 2metO-1HAQ magic-angle transient spectra (delay in ps).

narrowing and the intensity increase of the *ESA* band in respect to the 1 ps spectrum. We observe a small *blue* shift of the *ESA* maximum and a more pronounced vibronic structure. This spectral evolution is the evidence of the vibrational relaxation in the excited state potential well. , The complete elimination of the rotational components is guaranteed by the absence of any pronounced intensity variation during the first twenty picoseconds (Figure 4.19). The temporal evolution of $A_{ma}(\lambda, t)$ at larger delays (Figure 4.20) is governed by the electronic population relaxation.

Once applied the *GVD* correction, we performed a decomposition of the family of spectra taken at different delay times with the help of the *singular value decomposition* (*SVD*) method (section A.0.4.1). The standard *SVD* algorithm, which uses the *LAPACK* routines to compute matrix decomposition, was implemented in a home-made program. *SVD*, combined with a subsequent *target analysis* (section A), is a powerful procedure which allowed us to extrapolate the spectra and the temporal evolution of the vibrational and electronic (decay of excited state population) relaxation. We performed the *SVD* analysis on the matrix associated to the spectra at the magic angle condition (Equation 4.2) according to the relation:

$$A(\lambda, t)_{ma} = U \cdot S \cdot V^T \tag{4.26}$$

The decomposition procedure gave two main components characterized by singular values $S_1 = 3.7$ and $S_2 = 0.3$. The normalized basis spectra (first two columns of

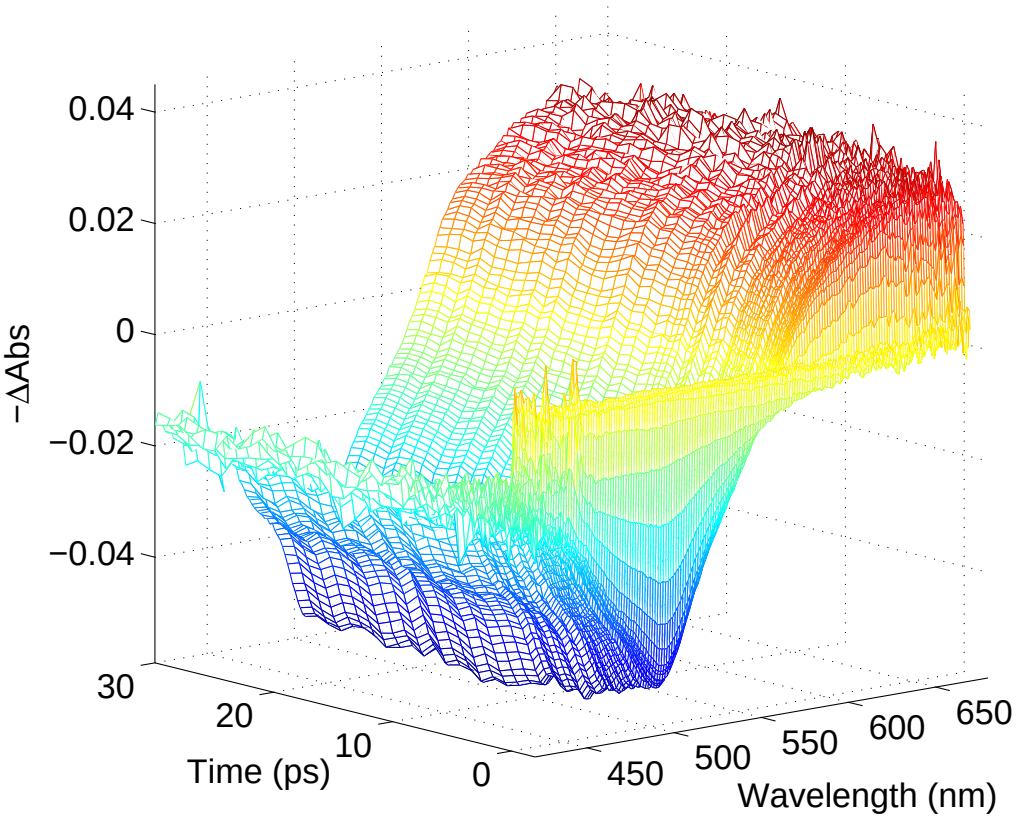

Figure 4.19: 2metO-1HAQ magic-angle transient spectra: The first thirty picoseconds.

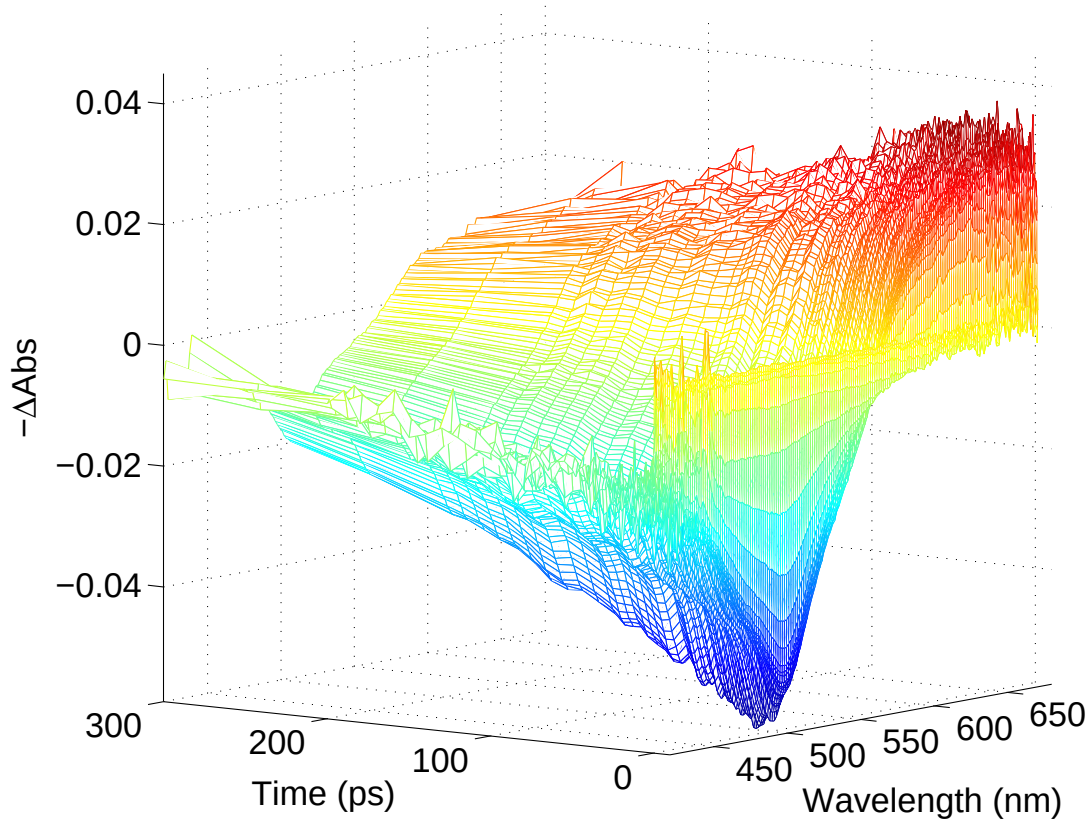

Figure 4.20: 2metO-1HAQ magic-angle transient spectra: The first three-hundred picoseconds.

matrix U) are shown below:

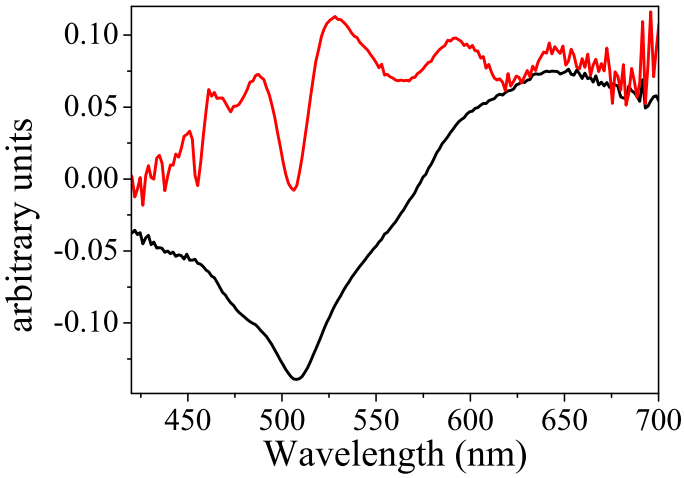

Figure 4.21: Normalized basis spectra U_1 (*black*) and U_2 (*red*).

As stressed in section A.0.4.3, the columns of U are pure mathematical objects, without any physical sense. The *decay associated difference spectra* (*DADS*) are, instead, obtained by a suitable linear combination of the two basis spectra. The coefficients of the linear combination (matrix $\mathbb{A}$, section A.0.4.3) can be obtained by the target analysis of the temporal evolution profile of the two basis vectors. The temporal evolution of the basis U_1 and U_2 is given by the first two columns of the matrix V. Hence we performed the target analysis on the columns V_1 and V_2 scaled by the their singular values S_1 and S_2. We assumed a bi-exponential kinetic model for the molecular response function $R(t)$:

$$R_l(t) = A_{l1}\, e^{-t/\tau 1} + A_{l2}\, e^{-t/\tau 2} \qquad l = 1, 2 \tag{4.27}$$

Where the subscript l indicates the column of V. The evolution of V_1 and V_2, along with their fitting curves, are shown in Figure 4.22. Because of the presence of a strong *XPM* artefact during the first hundreds of femtoseconds, we did not discuss the evolution within this time interval. The instrumental function was determined

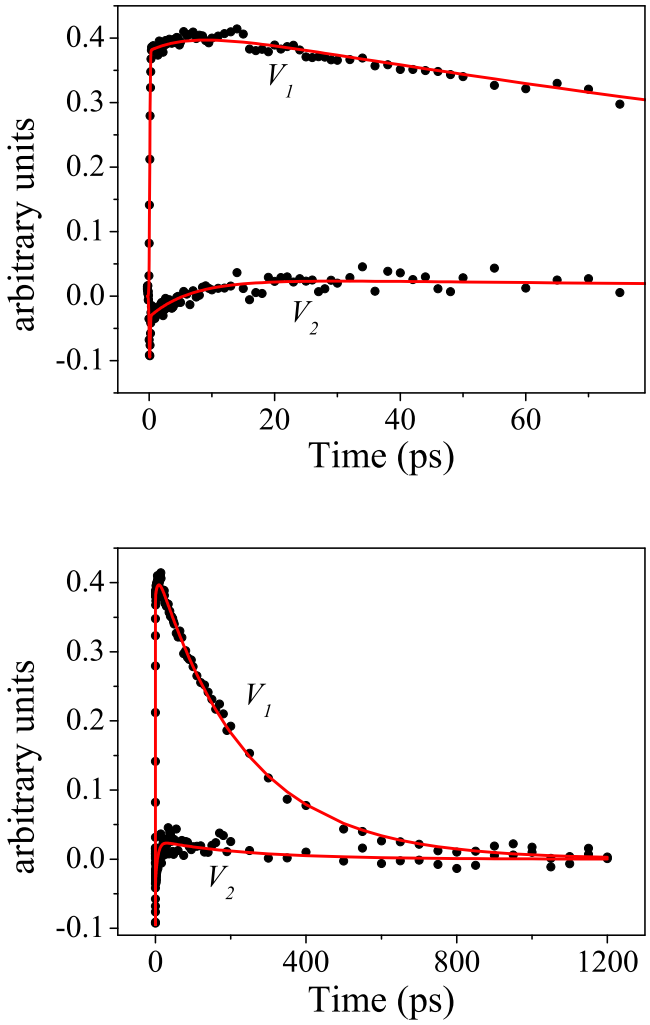

Figure 4.22: Vectors (amplitude versus time) V_1 and V_2 (•), and fitting curves (*red*).

following the procedure described in section 2.4.3, obtaining a gaussian-shape function with $\sim$ 200 fs FWHM. We simulated the coherent effect (XPM) by the convolution of the instrumental function with a δ-type function. Instead, the evolution of V_1 and V_2 was simulated by the convolution of the instrumental function with a bi-exponential kinetic model. The parameters of the model function was simultaneously optimized on V_1 and V_2 kinetic traces by means of a home-developed global

fitting program. The results of the fitting procedure are collected in table 4.3.

Table 4.3: Parameters for simultaneous fit of singular value decomposition components to a biexponential model.

component	$A_{n1} * 10^{-2}$	τ_1 *(ps)*	$A_{n2} * 10^{-2}$	τ_2 *(ps)*
V_1	-4.4 ± 0.4 (10%)	7 ± 2	42 ± 4 (90%)	238 ± 5
V_2	-5.9 ± 0.7 (69%)		2.7 ± 0.3 (31%)	

The *DADS* were obtained from the linear combination

$$(DADS)_m = \sum_{n=1}^{2} (A_{nm} \cdot U_n); \tag{4.28}$$

the two *DADS* are shown in Figure 4.23. The SVD method is extremely useful for the analysis of two-way matrix data (wavelength/time in transient absorption experiments) in which the the acquired spectra are given by the sum of more than one component (Equations A.7 and A.8). Matrix decomposition allows to identify the principal components and to isolate their spectra (columns of matrix U) and their temporal evolution (columns of matrix V). These components can be related to "true" molecular species, each characterized by its own spectrum and temporal evolution, or to a single molecular species characterized by, at least, two different spectra during the temporal evolution. This last condition can occur, for example, when the ground state recovery of a photoexcited molecule involves an intermediate electronic excited state. If the intermediate state is characterized by a transient spectrum which is different from the one associated to the state directly populated by the pump pulse, then *SVD* will identify two distinct components. This is the typical two-compartment kinetic model of type II described in section A.0.3.2. This is a rather simple example, *SVD* method is usually employed to analyze matrix data associated to much more complex spectral and temporal evolutions. An important

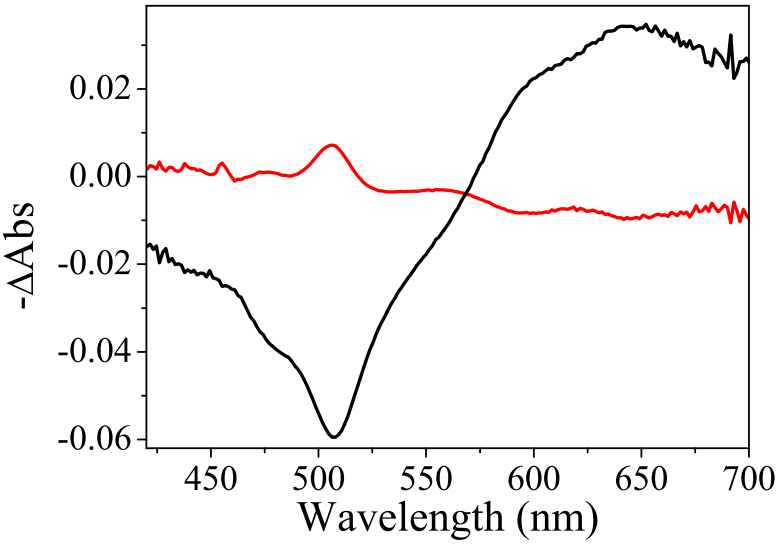

Figure 4.23: Spectral components of the biexponential kinetic model employed for the simulation of (scaled) V_1 and V_2: $DADS_1$ (*red* spectrum) and $DADS_2$ (*black* spectrum).

example is the use of *SVD* in the analysis of CO recombination kinetics and *Soret* band shifts of proteins containing Heme group.[115–119] These works showed that *SVD* is extremely useful in extracting the main spectral and temporal components if the photoexcited species are characterized by similar spectra.

The *SVD* allowed to discriminate also the effect of a spectral and temporal "perturbation" on the main component. In our case, we used the *SVD* to characterize the vibrational contribution on the transient spectrum of the photoexcited 2metO-1HAQ molecule.

The spectrum associated to this temporal component (*DADS*) is shown in figure 4.23 (*red* spectrum). As the effect of the vibrational relaxation can be assimilated to a "perturbation" of the spectrum associated to the main component (electronic relaxation of 2metO-1HAQ), the decomposition does not result in a neat separation of the two components. Indeed the temporal evolution of each basis vector is characterized by the vibrational relaxation (τ_1) and by the electronic relaxation

(τ_2) components. However the results of the global fitting (table 4.3) show that the evolution of V_1 is dominated by the electronic relaxation ($A_{12} = 90\%$), while the evolution of V_2 is mainly related to the vibrational relaxation ($A_{21} = 71\%$).

4.4.1.4 Conclusions

We isolated the rotational contribution by means of equations 4.1 and 4.2 and we fitted the anisotropy evolution by a single exponential. We approximated the molecular shape as a *prolate* ellipsoid and we calculated the theoretical friction coefficients by means of the hydrodynamic theory. The "slip" boundary conditions were then applied to correct the *perpendicular* friction coefficient for the deviation from hydrodynamic rotational diffusion. According to the model of Dote and Kivelson[109] we applied the correction only to the "tumbling" friction coefficient. The evaluated correlation times are all similar: this is due to the low axial ratio of the ellipsoid ($\rho \sim 2$) and to the "slip" boundary condition for the pure "tumbling" rotational motion. In addition, we estimated the theoretical pre-exponential factors by means of an *ab initio TDDFT* calculation. The conclusion is that we can disregard the terms related to mixed "spinnig"-"tumbling" correlation time. The main contribution to the evolution of the anisotropy is due to a pure "tumbling" rotational motion, giving rise to a mono-exponential decay. The calculated correlation time ~ 16 ps is in good agreement with the experimental data (~ 18 ps) and also with a recently published work on a similar molecular system.[76]

As we emphasized in section 4.2 and as reported by several authors,[61–75] the large Stokes shift of the fluorescence emission in respect to the absorption band is the experimental evidence of the excited state intramolecular proton transfer reaction. This means that the observed *SE* band is associated to a transition from the state with the transferred proton: S_1'. Since the *SE* and *ESA* bands appear simultaneously, also the *ESA* is associated to a transition from S_1'. In addition, we do not observed any spectral or temporal dynamic related to the proton transfer process. This is in agreement with previous works[88,89,91–94] which reported an ultra-

fast (sub-100 fs) dynamic for the excited state proton transfer. In this sense we are limited by our instrumental function ($\sim$ 200 fs with 400 nm excitation) and by the marked coherent effect (*XPM*) observed at the temporal coincidence between pump and probe.

We conclude that the excitation of 2met-1HAQ at 400 nm results in the direct population of the S_1' state. This is confirmed by two experimental evidences:

- Contemporary presence of *SRG*, *ESA* and *SE* bands in the GVD-corrected spectra (figure 4.18 *left* panel).
- The rise time of the transient signal is given by the convolution of the instrumental function with a step function, as confirmed by the fitting of the components V_1 and V_2 reported in figure 4.22.

4.4.2 Excitation with 325 nm Wavelength

Transient spectra and single wavelength measurements of 2metO-1HAQ, following 325 nm pump excitation, were obtained by means of the experimental configurations described in section 2.1 and 2.1.2. The excitation wavelength was obtained by *FHG* of the output of a BBO-based OPA (section 2.1), setting the angle between the polarization directions of pump and probe to 54.7°.

The transient spectra are shown in figures 4.24 and 4.25, not corrected for the *group velocity dispersion*. The spectra are characterized by the stimulated emission (*SE*) band, centered around 650 nm, and by an excited state absorption band (*ESA*), centered around 508 nm. The shape of *ESA* band is affected, on the high frequency side, by the presence of the *ground state bleaching* (*GSB*) spectrum. This modification is particularly evident in figure 4.24 where the profile of the ground state absorption band (related to the $S_0 \rightarrow S_1$ transition) is recognizable. The position and the shape of the main spectral components are the same as those observed after the excitation at 400 nm of 2metO-1HAQ. Also the spectral evolution during the first 30 picoseconds strongly resembles the evolution observed when the transition

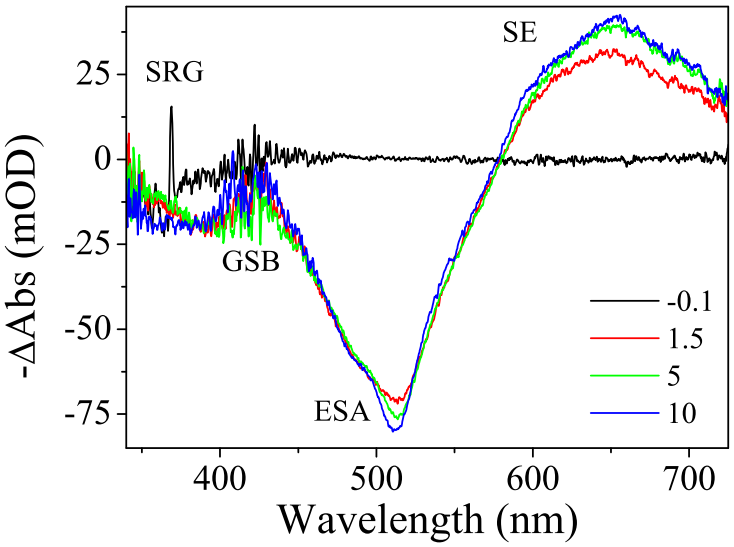

Figure 4.24: Transient spectra (first ten picoseconds) recorded after 325 nm pump excitation ($\sim$ 0.8 μJ pulse) of a solution of 2metO-1HAQ (*solvent*=CH_3CN, $Abs_{325nm} \simeq 0.9$).

$S_0 \rightarrow S_1$ of 2metO-1HAQ is directly promoted. Indeed, in figure 4.24 the increase of intensity of the maximum of the *ESA* band is particularly evident, while in figure 4.25 we can observe a small ($\sim$ 2nm) *blue* shift of the *ESA* band maximum between the 10 ps and the 30 ps spectra. This effect is due to the vibrational cooling process that take place in the excited state potential well.

We measured the transient absorption spectra up to 1.5 ns delay (figure 4.25); in this temporal interval we observed a monotonous decrease of the signal's intensity, which becomes negligible 1 ns after excitation. We inspected in detail the temporal evolution of the *ESA* and *SE* bands obtained from the single wavelength measurements (section 2.1.2) reported in Figures 4.26 and 4.27. We decided to record the kinetics on the maximum (λ=508 nm) and on both the low (λ=530 nm) and high (λ=482 nm) frequency side of the *ESA* band, in order to characterize the dynamics related to the vibrational cooling process. The evolution of the *SE* was monitored at 635 nm. The instrumental function at various wavelength was obtained by means

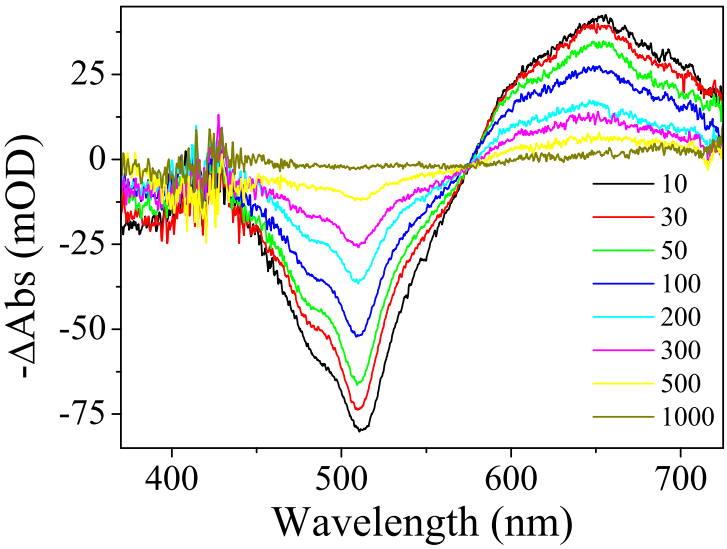

Figure 4.25: Transient spectra (evolution during the first nanosecond) recorded after 325 nm pump excitation ($\sim$ 0.8 μJ pulse) of a solution of 2metO-1HAQ (*solvent*=CH_3CN, $Abs_{325nm} \simeq 0.9$).

of an Optical Kerr Effect OHD-OKE experiment (section 2.4.1), and the data fitted with gaussians, obtaining an average FWHM of $\sim$ 500 fs.

Table 4.4: Fitting results of single wavelength measurements.

λ_{probe} *(nm)*	$A_2 * 10^{-3}$	τ_2 *(ps)*	$A_3 * 10^{-3}$	τ_3 *(ps)*
482	-4.3 ± 0.5 (7%)	8 ± 2	58 ± 6 (93%)	240 ± 5
508	8.6 ± 0.7 (9%)		84 ± 8 (91%)	
530	-17 ± 2 (27%)		47 ± 5 (73%)	
635	7.7 ± 7 (16%)		40 ± 4 (84%)	

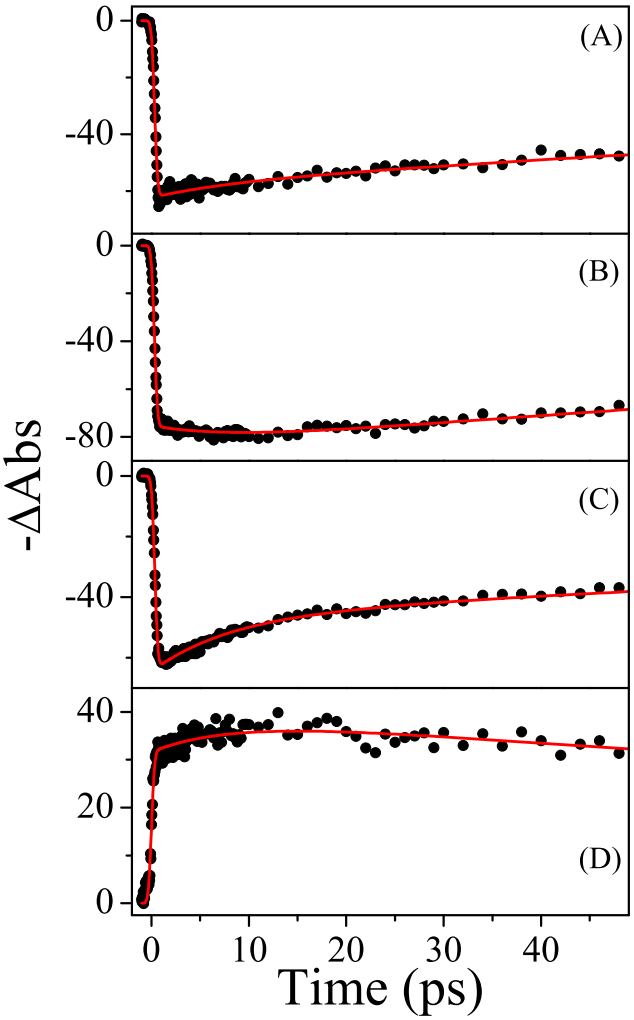

Figure 4.26: Evolution during the first 50 picoseconds of the kinetics recorded after 325 nm pump excitation ($\sim$ 0.8 μJ pulse) of a solution of 2metO-1HAQ (*solvent*=CH_3CN, $Abs_{325nm} \simeq 0.9$): (A) λ_{probe}= 482 nm; (B) λ_{probe}= 508 nm; (C) λ_{probe}= 530 nm; (D) λ_{probe}= 635nm.

Then the kinetic traces weer simulated by convoluting the instrumental function $g(t)$ with a biexponential molecular response function $R(t)$. The parameters of the model function were optimized on the basis of the four kinetic traces by means of a home-developed global fitting program. The results of the fitting are collected in

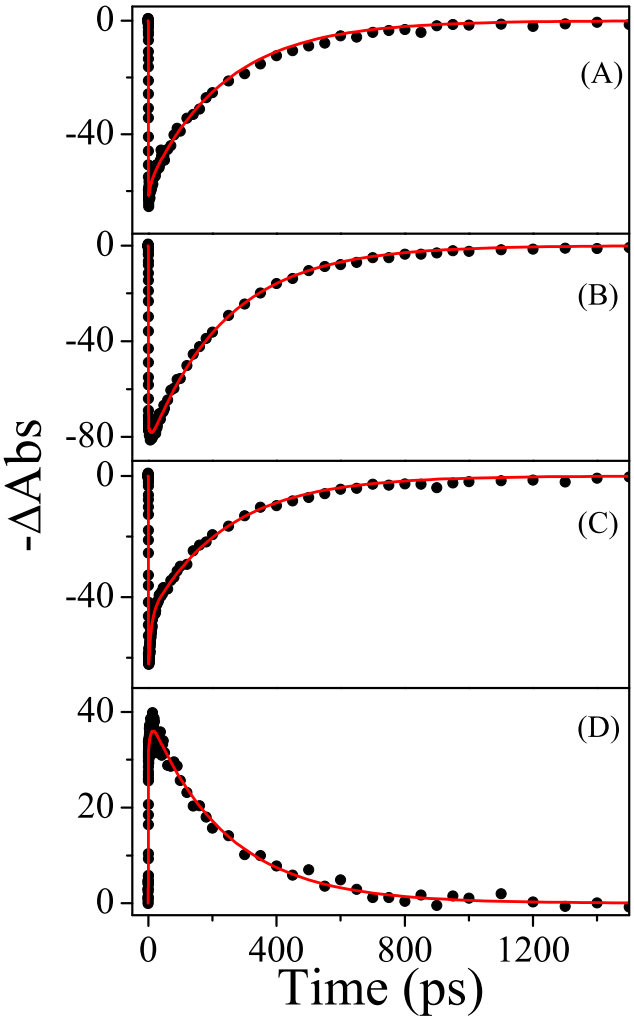

Figure 4.27: Complete evolution of the kinetics recorded after 325 nm pump excitation ($\sim$ 0.8 μJ pulse) of a solution of 2metO-1HAQ (*solvent*=CH_3CN, $Abs_{325nm} \simeq 0.9$): (A) λ_{probe}= 482 nm; (B) λ_{probe}= 508 nm; (C) λ_{probe}= 530 nm; (D) λ_{probe}= 635nm..

table 4.4.

4.4.3 Conclusions

The qualitative similarity of the transient spectra measured for excitation at 400 and 325 nm, is confirmed by the fitting of the single wavelength time profile. The biexponential kinetic model, with τ_1= 8 ps associated to the vibrational cooling process and τ_2= 240 ps associated to the ground state recovery, reproduces very well the experimental data.

Particular attention should be payed to the signal evolution during the first picoseconds. Upon applying the correction for the group velocity dispersion, we observed that the growth of *SE* and *ESA* bands is comparable with the evolution of the *SRG* band. In addition, the growth of the signal of the kinetics measurements is very well reproduced by the convolution of the instrumental function with a *step* function whose amplitude is given, for each inspected wavelength, by the sum of the pre-exponential factors of table 4.4. This means that, on our temporal resolution, *ESA* and *SE* appear immediately after the pulse excitation and then that the state S_1 is directly populated also by excitation at 325 nm . The ground state absorption spectrum (section 4.2) is characterized, in the region between 315 nm and 350 nm, by a weak absorption band. The nature of this absorption is not completely clear at the moment. The results obtained by a *TDDFT* calculation (at the B3LYP 6-31+G(d,p) level of theory) on the 2met-1HAQ molecule (section 4.3) indicate that this band could be related to a transition towards an excited electronic state located at higher energy in respect to the S_1 state. However, in the whole relaxation process, we do not observe any spectral or temporal dynamic associated to transitions from this excited state. This behavior can be interpreted with two fundamental hypothesis:

- The state is a *silent* state, i.e. it is not characterized by any transient absorption or the transient absorption features are located in an experimentally not accessible spectral region.

- The electronic population evolves, from this state, towards the state S_1 with an ultra-fast process whose duration is inferior to the width of our instrumental

function.

We conclude that the excitation of 2metO-1HAQ with 325 nm wavelength results in a direct population of the S_1 state. Any decrease of the rise time of the transient signal associated to *SE* or *ESA* can not be related to internal conversion processes of the isolated molecule.

Chapter 5

Time Resolved Characterization of Umbelliferone - 2metO-1HAQ Bichromophoric Molecular System

In this section we present the results, obtained for the chacaterization of the *Intramolecular Electronic Energy Transfer* (IEET) process in Umbelliferone - 2metO-1HAQ bichromophoric (Bi) molecular system.

5.1 Intramolecular Electronic Energy Transfer

The process of electronic energy transfer (EET) is ubiquitous in natural and artificial photochemically active systems. It is present in the antenna systems of photosynthetic organisms, in photodynamic therapy, in multichromophoric β-cyclodextrins, in photomolecular devices an in photochemical synthesis. EET processes occur at distances ranging from 1 Å to more than 50 Å, and on time scales from femtoseconds to milliseconds. When a donor and an acceptor are parts of the same compound, the EET is intramolecular (intra-EET), otherwise the EET is intermolecular (inter-EET). Inter-EET and Intra-EET are special cases of non-radiative processes contributing to the decay of electronically excited molecular systems. Depending

on the relative magnitude of the electronic coupling between donor and acceptor (V_{Dn-Ac}) and on the donor vibronic bandwidth, two limiting cases of EET can be distinguished which are referred to as strong and weak coupling mechanisms respectively. In the strong coupling case, the excitation is delocalized on both the donor and the acceptor. Within the weak coupling regime, the rate for energy transfer K_{ET} between an excited donor and a ground state acceptor can be derived from the time-dependent perturbation theory and the Fermi Golden Rule as

$$K_{ET} = \frac{2\pi}{\eta}|V_{Dn-Ac}|^2\,(FCWD) \tag{5.1}$$

where the *FCWD* represents the Franck-Condon weighted density of states, corresponding to the product of the density of vibrational states in the initial and final states and their spectral overlap. In general, the effective electronic coupling matrix element V_{Dn-Ac} can be expressed as a sum of electronic coupling terms

$$V_{Dn-Ac} = u^{Coulombic} + u^{short-range} + u^{bridge} \tag{5.2}$$

where $u^{Coulombic}$ represents through-space acting Coulombic interaction between dipoles and/or higher multipoles; $u^{short-range}$ depends upon the interchromophore orbital overlap and consists of a term accounting for the interpretation of the charge density centered on one molecule with that of the other molecule and of an exchange term defining the quantum mechanical two-electron exchange interaction; u^{bridge} accounts for the transfer of energy from the donor to the acceptor via intermediate moieties or connecting bridges.

Understanding the mechanism of EET between two chromophores is the key for the design and construction of efficient photonic devices, artificial energy harvesting systems, and it is of interest in optical computing and molecular electronics.

Bichromophore molecules, containing two or more distinguishable molecular units separated by bridges of controllable length, are ideal systems for investigating intra-EET processes. The property of the bridge determines the degree of flexibility of the whole structure and the basic electronic structure of the chromophore. On the

other hand, if the bridges induces reciprocal interaction of the two chromophores, the optical properties of the bichromophoric species result "non-additive".

5.2 Absorption Spectra

The ground state absorption spectrum of bichromophore was measured in acetonitrile solution and at room temperature. The molar extinction coefficients of bichromophore *Bi*, of isolated donor *Dn* (Umbelliferone) and of isolated Acceptor *Ac* (2metO-1HAQ) are reported in Figure 5.1.

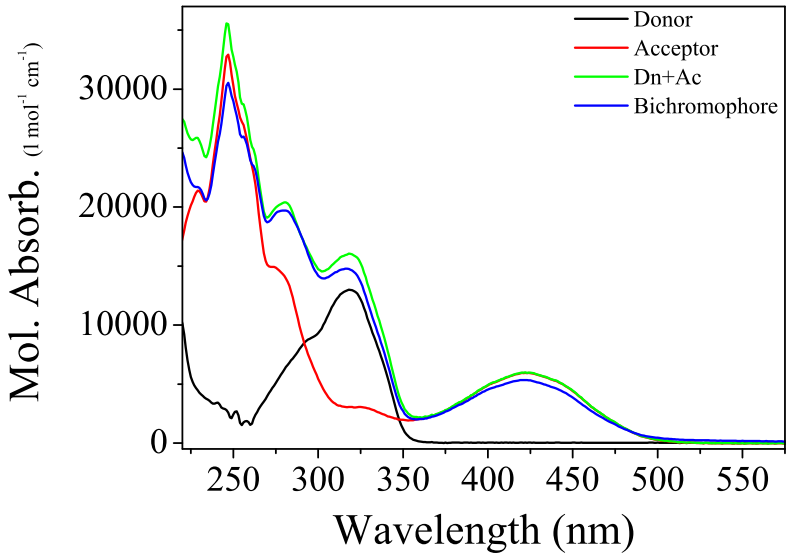

Figure 5.1: Ground state molar extinction coefficients of Umbelliferone (*Dn*), 2metO-1HAQ (*Ac*), bichromophore (*Bi*), and of the sum (*Dn*)+(*Ac*) .

In bichromophoric systems, the role of the molecular bridge between *Dn* and *Ac* is of primary importance in relation to the efficiency of the energy transfer process. Interchromophore bridge should act as an inert spacer, minimizing any coupling between the ground electronic states of the two chromophores.

The molecular bridge of Umbelliferone-Alizarine bichromophore is characterized by a triazole ring, linked to *Dn* and *Ac* with two single methylene groups (figure

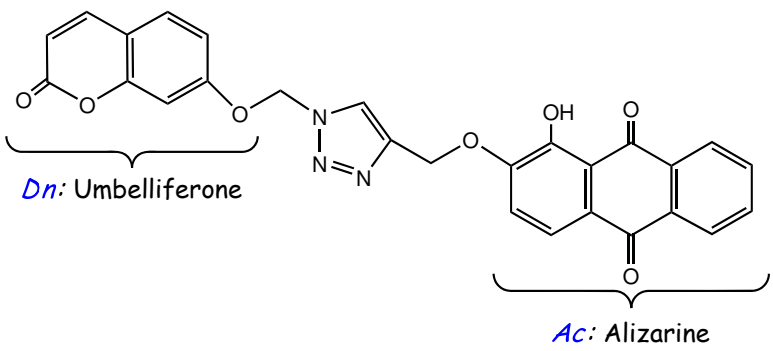

Figure 5.2: Umbelliferone-Alizarine bichromophoric molecular system.

5.2). A qualitative estimate of the coupling between the two chromophore units through the molecular bridge can be obtained from the ground state absorption spectra. As shown in Figure 5.1, the bichromophore absorption spectrum is close to the sum of the spectra of the *Dn* and *Ac* units. This means that the energy levels involved in the electronic transitions are weakly perturbed by the triazole ring. Furthermore, particular attention has been payed to the choice of the two

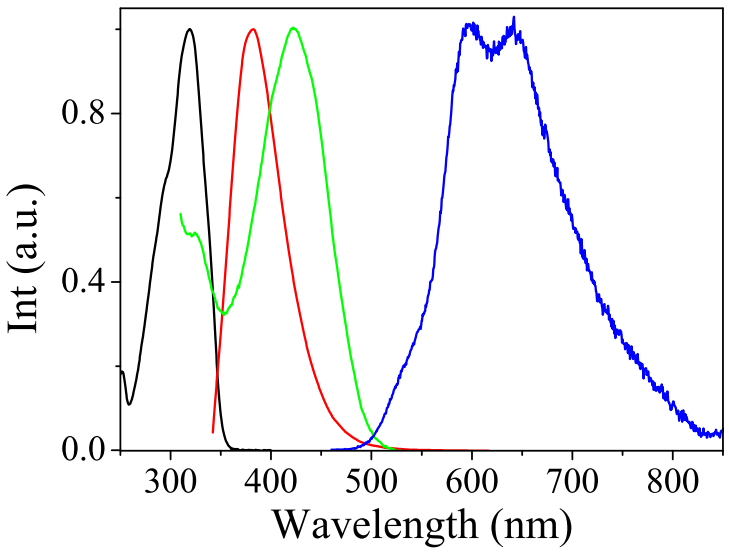

Figure 5.3: (*black*)Donor absorption band; (*red*)Donor emission band;(*green*)Acceptor absorption band;(*blue*)Acceptor emission band;.

chromophores. Indeed, the second fundamental requirement, for an efficient intra-EET, is the largest spectral overlap between the emission band of the donor unit and the absorption band of the acceptor chromophore. At the same time, the absorption band of the donor chromophore should be in a spectral region where the acceptor chromophore does not absorb or, at least, the ratio between the molar extinction coefficients $\varepsilon(Dn)/\varepsilon(Ac)$ should be as high as possible. This latter condition is crucial in order to prevent the direct excitation of the acceptor unit, which would give rise to two different mechanisms of population of the excite state of the acceptor and would complicate the analysis of intra-EET dynamic. In practice, this two conditions can be hardly satisfied at the same time; we choose to maximize the ratio $\varepsilon_{Dn}/\varepsilon(Ac)$ to the expense of a better spectral overlap (Figure 5.3).

The peculiarity of the investigated system is, by the way, due to the large Stokes shift between the absorption and the emission band of the acceptor. As we stated in section 4.1, this characteristic of alizarine is related to the excited state intramolecular proton transfer process. Hence, this system is a prototype for studying the indirect activation of an excited state reaction.

5.3 Transient Absorption Spectra

Transient spectra and single wavelength measurements of the bichromophore, following 325 nm pump excitation, were obtained using the experimental configuration described in section 2.1 and 2.1.2. The excitation wavelength was obtained by *FHG* of the output of a BBO-based OPA (section 2.1), setting the angle between the polarization directions of pump and probe to 54.7°. Due to the low solubility of the compounds, we were not able to fulfill the optimal condition of Abs $\simeq$ 1 at the excitation wavelength, and we performed transient spectra and single wavelength measurements with Abs(λ=325 nm)$\simeq$ 0.5.

Transient spectra are shown in figure 5.4, 5.5 and figure 5.6, without any correction for the *group velocity dispersion*. They are characterized by an excited state

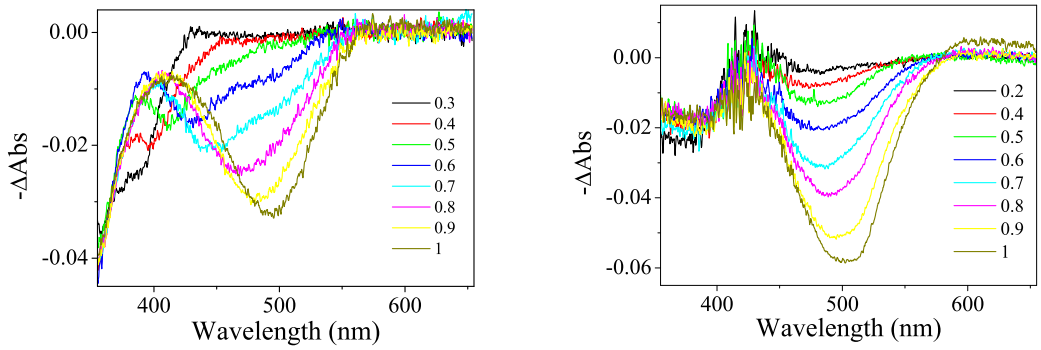

Figure 5.4: Transient spectra (delays in ps) recorded after 325 nm pump excitation ($\sim$ 0.8 μJ pulse) of: (a) (*left*) solution of Bichromophore (*solvent*=CH_3CN, $Abs_{325nm} \simeq 0.5$), (b) (*right*) a solution of 2metO-1HAQ (*solvent*=CH_3CN, $Abs_{325nm} \simeq 0.9$)

absorption band *ESA* centered around 508 nm, and a stimulated emission *SE* band centered at 650 nm. The spectral features are virtually identical to those of the isolated *Ac*. However, the shape of the *ESA* band, on the high frequency side, differs with respect to the isolated acceptor. As we showed in section 3.5, the spectra of Umbelliferone are characterized by the *SE* band and, on its high frequency side, by an intense *ESA* band centered around 350 nm. Hence, in the spectral region between 350 and 420 nm (hereafter we will call this spectral region the *blue region*), the transient spectra of the bichromophore are given by the sum of more than one contributions: the residual transient absorption and stimulated emission of *Dn*, plus the broad *ESA* band of *Ac*. This effect is particularly evident in the spectra shown in the left panel of Figure 5.4. The spectra are clearly not corrected for the *GVD*, but, limiting our analysis to the *blue region* and for delays greater than 0.3 ps, we can disregard this effect. Then, the difference between the spectra of the isolated *Ac* and of the bichromophore is not fictitious, due to the uncorrected dispersion. The isolated *Ac* is characterized only by the *GSB* superimposed onto the broad *ESA* (centered at 508 nm), while in the bichromophore's spectra the *ESA* peaked at 350 nm is evident.

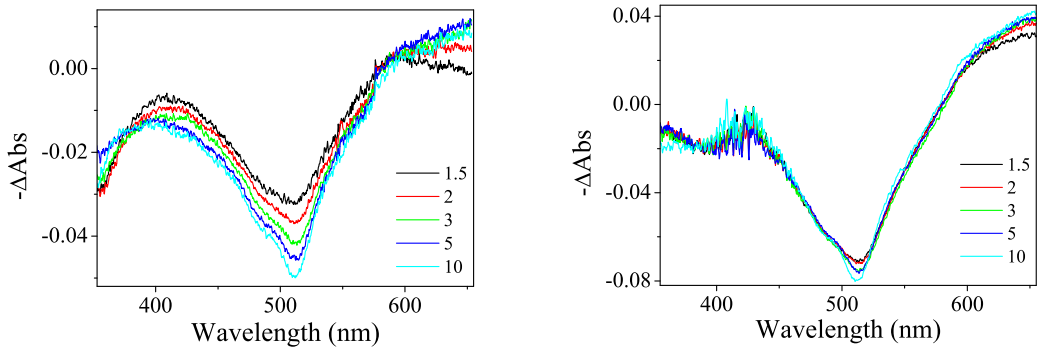

Figure 5.5: Transient spectra (delays in ps) recorded after 325 nm pump excitation ($\sim$ 0.8 μJ pulse) of: (a) (*left*) solution of Bichromophore (*solvent*=CH_3CN, $Abs_{325nm} \simeq 0.5$), (b) (*right*) a solution of 2metO-1HAQ (*solvent*=CH_3CN, $Abs_{325nm} \simeq 0.9$).

The effect of the donor's *ESA* band is evident also in Figure 5.5, where we show the evolution during the first ten picosecond of the bichromophore (*left* panel) and of the isolated acceptor (*right* panel). These spectra show the decay of the transient signal in the spectral region between 350 and 380 nm for the bichromophore, while this signal's decrease is not observed in the isolated acceptor.

The isolated donor is characterized by a decay time, from the state S_1, of $\simeq$ 30 ps, meaning that 10 picoseconds after pulse excitation the signal's decay is already appreciable. The decrease of bichromophore's transient signal can then be related to this effect.

Further evidence of the presence of at least two spectral contributions in the *blue region* is given by the existence of an isosbestic point located at around 380 nm; approximatively at the same wavelength of the isosbestic point observed in the isolated donor's transient spectra.

This spectral region is clearly not suited for the characterization of the dynamic related to the energy transfer process. Indeed, to have the best estimation for the kinetic constant and, then, for the efficiency of the transfer, we have to monitor the transient signal related to the acceptor unit only.

The bichromophore's spectra reported in Figure 5.2 show also a different temporal evolution in the region between 450 and 650 nm with respect to the isolated acceptor. In particular, it is evident a slower rise-time of the whole *ESA* and *SE* bichromophoric bands, while the spectra of the isolated acceptor show only an increase and a slight blue shift of of the *ESA* band maximum. As we emphasized in section 4.4.2, the latter effect is due to the vibrational cooling process, while on the basis of the conclusions derived in section 4.4.3 the former effect can only be related to the energy transfer process between donor and acceptor units.

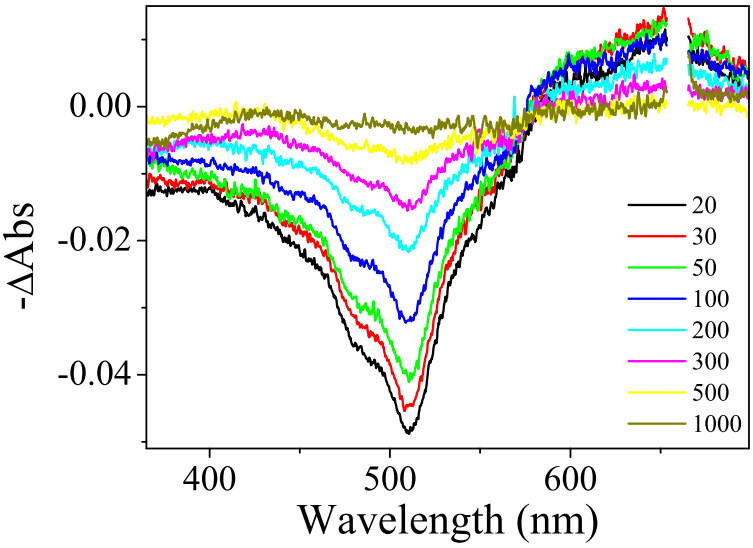

Figure 5.6: Transient spectra (delays in ps) recorded after 325 nm pump excitation ($\sim 0.8\ \mu$J pulse) of a solution of Bichromophore (*solvent*=CH_3CN, $Abs_{325nm} \simeq 0.5$).

The evolution on long time scale (till 1 ns) is shown in Figure 5.6 and is characterized by the decay of the whole transient signal.

5.4 Single Wavelength Measurements and Conclusions

In order to have quantitative information about the dynamic of the energy transfer process, we performed single wavelength measurements by means of the experimental set-up described in section 2.1.2.

As we discussed in the former section, we have to monitor the transient signal of the acceptor unit in a spectral region where the contributions of donor's spectral components are negligible. for that reason, we choose to perform single wavelength measurements at 635 nm only, where the intensity of the *SE* band and the absorption from the triplet state of the donor can be disregarded.

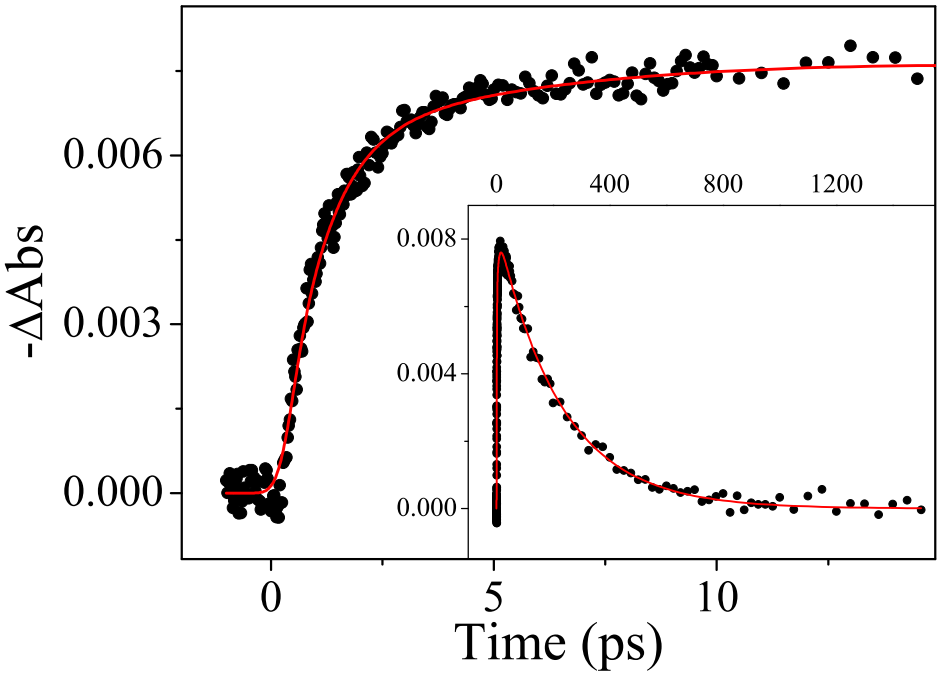

Figure 5.7: single wavelength measurement (λ_{probe}=635 nm) recorded after 325 nm pump excitation ($\sim$ 0.8 μJ pulse) of a solution of Bichromophore (*solvent*=CH_3CN, $Abs_{325nm} \simeq 0.5$).

The kinetic trace is reported in figure 5.7, along with the fitting curve. The first part of the kinetic trace has been reproduced by the convolution of the instrumental function (gaussian-type function with 500 fs FWHM) with the molecular response function given by:

$$R(t) = A_0 + A_{ET}\left(1 - e^{-t/\tau_{ET}}\right) \tag{5.3}$$

where A_0 accounts for the amount of direct excitation of the acceptor unit (at this wavelength we have $\varepsilon_D/\varepsilon_A \simeq 4$), while A_{ET} is associated to the energy transfer component. The fitting procedure gave us A_0=0.021 ± 0.003 A_{ET}= 0.092 ± 0.003 and τ_{ET} = 1.1 ± 0.3 ps. The decay part were fitted with a biexponential kinetic model:

$$R(t) = A_1 \exp(-t/\tau_1) + A_2 \exp(-t/\tau_2) \tag{5.4}$$

and from the fitting procedure we obtained A_1 =-0.017 ± 0.003, τ_1= 8 ± 2 ps, A_2 =0.067 ± 0.005 and τ_2= 225 ± 15 ps. As described in section 4.4.3, the time constant τ_1 is related to the vibrational cooling, while the longer decay time τ_2 is due to the electronic relaxation. We can now calculate the efficiency of the energy transfer Q, which is given by

$$Q = \frac{K_{ET}}{K_{ET} + (K_f + K_{IC} + K_{ISC})_D} \tag{5.5}$$

where $K_{ET} = 1/\tau_{ET}$ is the kinetic constant for the energy transfer process and $1/(K_f + K_{IC} + K_{ISC})_D = 1/\tau_D)$ is the deactivation time of the S_1 donor state measured experimentally. From equation 5.5, and knowing that τ_D= 27 ± 3 ps we obtain Q=0.961

The data discussed above highlight a very fast and efficient intramolecular electronic energy transfer process. It is important to model the mechanism responsible of the intra-EET, in other words, how *Dn* and *Ac* interact. Since *Dn* and *Ac* are linked each other by saturated σ bonds, we can assume that the energy transfer process is due to the Coulomb interaction described in section 5.1. We can then assume that the transfer process is of the Förster type; apparently the *through-bond* transfer mechanism, plays a negligible role, as well as any possible Triplet-Singlet exchange

interaction. According to the Förster theory, we can estimate the distance between the two interacting dipole, that is, the distance between the center of mass of the two chromophore. The transfer rate constant is related to the interchromophoric distance by

$$K_{ET} = \frac{9000 \ln 10 \, k^2 \, \Phi_{Dn}}{128 \, \pi^5 \, n^4 \, N_A \, \tau_{Dn} \, R^6} \, J_{res} \tag{5.6}$$

$$J_{res} = \int_0^\infty \frac{F_D(\nu)\varepsilon(\nu)}{\nu^4} \, d\nu \tag{5.7}$$

where k^2 is the orientational factor, Φ_{Dn} and τ_{Dn} are the fluorescence quantum yield and the lifetime of the isolated donor Dn respectively, n is the refractive index of the solvent, N_A is the Avogadro's number, R is the interchromophoric distance and $Jres$ is the spectral overlap integral. In equation 5.7, $F_D(\nu)$ is the normalized emission spectrum of Dn and $\varepsilon(\nu)$ is the molar extinction coefficient of isolated Ac (It should be note that if the wavenumbers are expressed in cm^{-1}, then the distance R is expressed in cm). Making use of equation 5.7, and considering the orientational factor equal to 2/3 (random orientation), we obtained for $R \simeq$=7.5 Å. Considering the flexible molecular bridge, this distance can be the real distance between the two chromophore, only assuming a "cofacial" conformation.

Chapter 6

Sub-picosecond Optically Induced Valence Tautomeric Interconversion of a Manganese-Dioxolene Adduct

Photoinduced electron transfer is the phenomenon characterising any potential application of the conversion of photon energy into chemical potential energy.[120,121] The modified charge distribution of the chromophore, consequent to the absorption of a photon, can be exploited in turn as a memory bit of information or for creating the primary reaction trigger and establishing an useful potential gradient. Examples are transmembrane potential differences in biological systems[122,123] or the electric potential associated to electron-hole pairs when the chromophore is anchored to a semiconductor material.[124–126] The possible application of the photon absorption event is however intrinsically dependent on the time scale of the processes determining the relaxation to the ground state of the excited chromophore. The relaxation from the excited state to lower energy states involves several mechanisms usually indicated as internal conversion, intersystem crossing, vibrational relaxation, and so on. Quantum mechanics predict that in the intersystem crossing the electron transfer process can be treated as an activated radiationless transition between different

electronic states ψ_i and ψ_j of the chromophore. The rate constant k of the process is given by the relationship[127]

$$k = \frac{2\pi}{\hbar} |V|^2 G \tag{6.1}$$

where V is the electronic coupling matrix element including spin-orbit coupling, and G is the thermally averaged nuclear Franck-Condon vibrational overlap factor. The value of V depends on the overlap of the ψ_i and ψ_j wave functions. As a general expectation, it can be predicted that this value is large if the two wave functions have the same multiplicity, while it is small when their character is different. For this reason, in order to obtain optically induced long-lived charge separations to be exploited in chemical applications, it is generally believed necessary to populate low-lying excited states having different spin multiplicity from that of the electronic ground state of the chromophore. The spin-forbidden character of the transition slow down the relaxation of the excited state back to the ground state. However if the electron transfer process involves states with the same spin multiplicities, the recovery rate constant is presumed to be so large that any wished interaction with the chemical environment is precluded.

6.1 Introduction

Few years ago it has been demonstrated that dioxolene adducts of a manganese-tetraazamacrocycle acceptor can be isolated with two different charge distributions.[128] It was found that the complexes of general formula Mn(CTH)(diox)Y (*CTH*=*dl*-5,7,7,12,14,14-hexamethyl-1,4,8,11-tetraazacyclotetradecane, *diox*=semiquinonato (DBSQ) or catecholato (DBCat) forms of 3,5-di-*tert*-butyl-o- benzoquinone) can be isolated at room temperature as *green* Mn^{II}(CTH)(DBSQ)ClO_4 and *yellow-brown* Mn^{III}(CTH)(DBCat)PF_6 (or BPh_4) redox isomers. In the solid state these complexes undergo entropy driven valence tautomeric inter-conversion

$$Mn^{III}(CTH)(DBCat)Y \rightleftarrows Mn^{II}(CTH)(DBSQ)Y \tag{6.2}$$

involving an intramolecular electron transfer between the dioxolene ligand and the metal ion. Temperature dependent magnetic susceptibility studies showed that the two complexes are characterised by quintet electronic ground states. For the *yellow-brown* derivatives this is consistent with the Mn^{III}-DBCat charge distribution (the metal ion being $hs - d^4$).

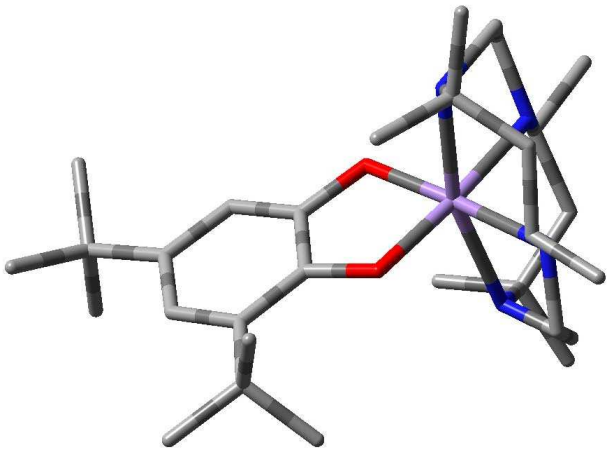

Figure 6.1: X-Ray Schematic structure of Mn(CTH)(diox).

X-ray structural data well support this suggestion. For the *green* derivative the observed magnetic data (Figure 6.2) are strongly in favor of the existence of a large anti-ferromagnetic coupling interactions between the *hs*-manganese(II) ion ($t_2g^3e_g^2, S = 5/2$) and one semiquinonato ligand ($\pi^{*1}, S = 1/2$), as theoretically predicted.

These adducts exist in the two different charge distributions in solution. Indeed electronic spectra showed (Figure 6.3) that they exist as Mn^{II}-DBSQ in low-donor solvents (acetone, 1,2-dichloroethane, toluene), whereas in high-donor solvents, like DMSO and methanol, the Mn^{III}-DBCat redox isomer dominates. In acetonitrile the two redox isomers coexist, the Mn^{III}-DBCat being predominant at room temperature and the Mn^{II}-SQ one at higher temperature. Previous studies suggested that this behavior should be due to the difference in solvation enthalpy of the two species in the different solvents.[129]

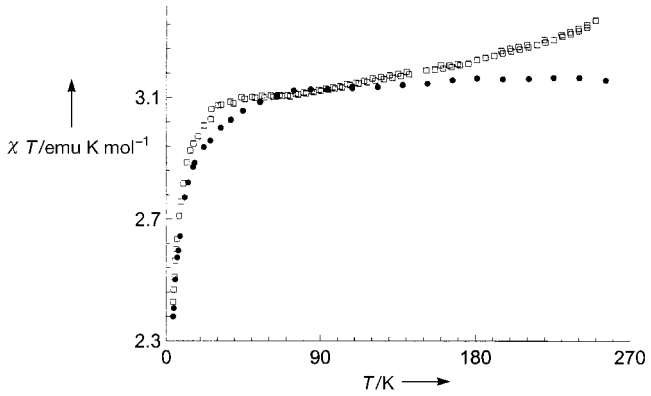

Figure 6.2: Change in χT as a function of temperature T for Mn^{III}(CTH)(DBCat) (•) and for Mn^{II}(CTH)(DBSQ) (□).

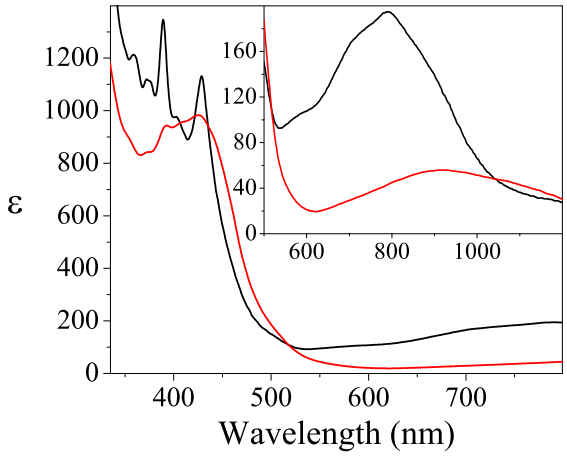

Figure 6.3: Electronic spectra of [Mn(cth)(dtbcat)]BPh_4 in acetone (*black curve*) and DMSO (*red curve*).

Several reports on manganese and cobalt dioxolene complexes undergoing valence tautomerism,[130–136] suggest that, also in this case, the observed inter-conversion is associated to a substantial variation of the Mn-O coordination bond length (tentatively from 1.9 in Mn^{III}-DBCat species to 2.1 in the Mn^{II}-DBSQ one). This can be mainly attributed to the change in the σ^* orbital population, from e_g^1 in the Mn^{III} complex to e_g^2 in the Mn^{II} one. In the present work we performed a time

resolved spectroscopic study of this Manganese complex, to the purpose of clarifying the details of the electron transfer and energy relaxation processes occurring a typical valence tautomeric interconversion[137–140]. It is well known that the tautomeric equilibrium is influenced by the solvent, in particular *Dei et al.*[129] showed that high-donor solvent were able to stabilize the Mn(III) while low-donor solvent stabilize Mn(II); this indicates that the solvent plays a crucial role in determining the entity of the free energy of conversion. For that reason we decided to performed experiments in a solvent with intermediate donor characteristics, with the purpose of modulate the conversion free energy to increase the transfer probability.

6.2 Results and Discussion

Transient spectra were obtained following the 400 nm excitation of the acetonitrile solution containing $Mn^{III}(CTH)$(DBCat)PF_6. The 400 nm pump wavelength was obtained by frequency doubling the amplified output (duration $\sim$ 100 fs at 800 nm, repetition rate 1 kHz, energy 700 μ J/pulse) produced by a regenerative amplified Ti:Sapphire laser system. The solution was prepared under nitrogen atmosphere and the residual oxygen contained in the solution was eliminated by means of a vacuum pump. The Absorbance of the sample around 1 OD, thus fulfilling the condition of maximum excitation efficiency within the optical path. The irradiated volume is refreshed by stirring the sample with a micro magnet inside the cell and transient absorption spectra were recorded reducing the repetition rate from 1KHz to 100 Hz to avoid photo-damage of the sample. Transient absorption spectra and single wavelength measurements were done at room temperature, keeping the sample under vacuum, to prevent oxidation due to air exposure.

The acquired transient spectra, for delay times greater than 10 ps and till 1.2 ns (the maximum delay on our experimental setup), are characterized by a spectral feature which corresponds to the the difference between the static spectra of the two tautomers (Figure 6.4).

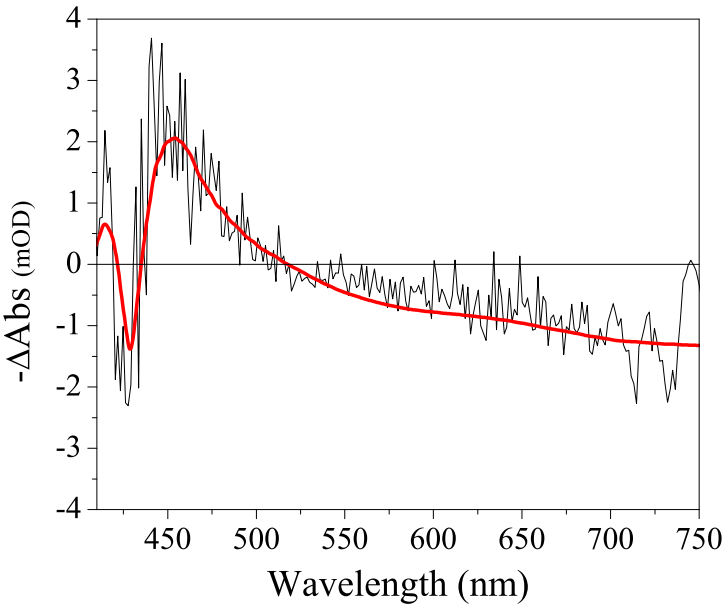

Figure 6.4: (*black*) Transient spectrum recorded 100 ps after 400 nm pump excitation ($\sim$ 0.8 μJ pulse) of a solution of $Mn^{III}(CTH)(DBCat)PF_6$ (*solvent*=CH_3CN, $Abs_{400nm} \simeq 1$). (*red*) Ground state difference spectrum of the two tautomeric form.

This means that 10 ps after excitation we observe the presence of the Mn^{II}-DBSQ form. The excited species is characterized by a very long lifetime, eceeding the detectable time window of our set-up (1.8 ns).

In order to obtain detailed information on the temporal dynamics within the first 10 picoseconds we performed single wavelength measurements. This technique allowed us to increase the sampling frequency of the transient signal without increase the global time of the experiment. In single wavelength measurements (Figure 6.5) we used 400 nm pump pulses, and 575 nm probe wavelength. The analysis of these data shows that three distinct components are needed to reproduce the experimental data, by convolution of the instrumental function with a decay function model:

- A very fast temporal component. This is due to the cross-phase modulation effect, and can be reproduced by the convolution of the instrumental function

(250 fs FWHM) with a delta-type function.

- The second component is related to the vibrational rearrangement in the excited state an is characterized by a decay time $\sim$ 1 ps.

- The third component is associated to the decay of the ESA band centered at $\sim$600 nm; the time scale of this process is too long to be measured with our apparatus (its contribution appears as a flat line).

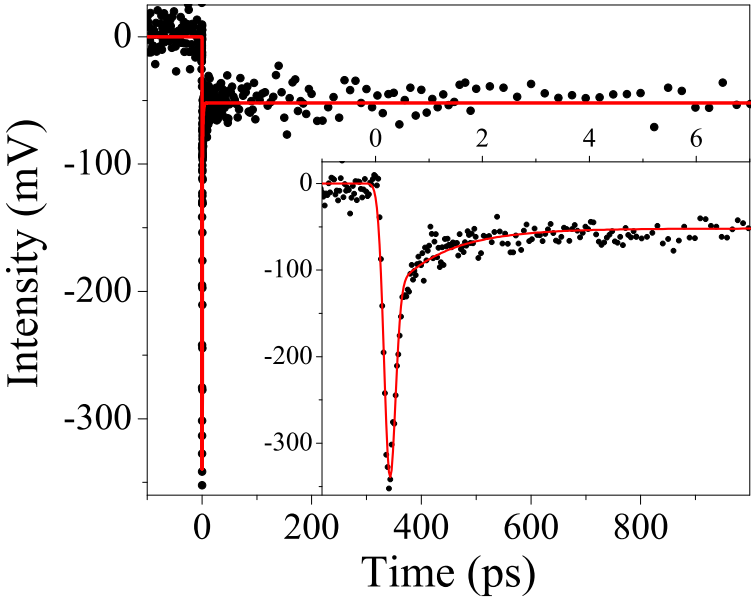

Figure 6.5: (•) Experimental single wavelength measure with $\lambda_{probe} = 525nm$ obtained after 400 nm pump excitation ($\sim$ 0.8 μJ pulse) of a solution of $Mn^{III}(CTH)(DBCat)PF_6$ (*solvent*=CH_3CN, $Abs_{400nm} \simeq 1$). (*red*) Fitting curve.

Previous studies reported on cobalt-dioxolene derivatives suggested that the optically induced valence tautomeric inter-conversion is virtually complete within 1 ps.[137,138]. The recovery time to the ground state occurs on the nanosecond time scale (1-100 ns).[139,140] The relatively large lifetime was explained by considering the different spin multiplicity character existing between the low-lying excited state

and the ground state. The results we report here confirm that the primary interconversion following photon absorption occurs within less than 1 ps. We are here arguing the existence of the orthogonality between the acceptor and donor orbitals involved in the electron transfer. Equilibrium 6.2 involves a formal electron transfer between the HOMO orbital of the catecholato moiety (π^* in character) and the e_g orbital of the metal ion (σ^* in character). The forbidden character of this process does not seem to constitute a severe constraint. The electron transfer process may involve firstly an orbital of the metal ion, with subsequent evolution on the ligand field manifold. Although the detailed mechanism is not well understood, it has been suggested that the evolution of the charge transfer state coupled to ligand field states consist of a barrier less inter conversion between highly mixed states, eventually leading to the population of the low-lying excited state. This result well agrees with those obtained in investigations concerning the optical interconversions of iron(II) spin crossover derivatives and ruthenium bipyridine complexes.[141–145] The most relevant result in our data is given by the unexpected large lifetime of the low-lying excited state, which well compares with those observed for different iron(II) spin crossover complexes and for cobalt-dioxolene undergoing valence tautomeric inter-conversion. In contrast to the present case, in those compunds the back relaxation involves states of different multiplicity, and this has been proposed as the explanation for the long lifetime of the low-lying excited state. The fact that a similar behavior has been demonstrated for the Manganese complex discussed here, for which no multiplicity difference can be invoked, leads us to conclude that the wave function multiplicity cannot be the determining factor in the relaxation process. It is probably very important to focus the attention on the role of the geometrical changes as reflected by the G factor. In the present case in fact this displacement is large; we can tentatively conclude that this point should be highly considered in the time dependent evolution dynamics of the chromophores which follow the photon absorption event.

Appendix A

Data analysis methods

A time resolved spectrum is the most well-known example of two-way data. These data are a collection of measurements in two dimensions (ways). The first dimension is the independent experimental spectral variable: wavelength λ or wave number $\overline{\nu}$. The second dimension is an independent experimental variable to monitor spectral change: time t after excitation, temperature T, polarization dependence or excitation wavelength. To understand the processes underlying the observable spectroscopic changes a model-based analysis is mandatory. From an analysis perspective two problems can be distinguished:

- when a parameterized model of the observations is available, the parameters have to be estimated in a statistical way
- when only a class of models is known, in addition the "best" model needs to be determined.

Several methodological reviews have been written on *global* and *target* analysis by Beechem[146–148] and coworkers, Ameloot[149] et al. Holtzwarth[150] and Dioumaev[151]. These reviews demonstrate the importance of simultaneous (*global*) analysis of multiple decay traces. The combination of global analysis with testing of a photophysical or photochemical model is often called target analysis. The word *model* can be used in two different ways.

One the one hand, a model for the observations is formulated in a mathematical-statistical terms. Thereby the measurements are described stochastically, since taking into account the noise properties is essential for precise parameters estimation.

On the other hand, the experimentalist is studying a complex system, generating a huge amount of observations. The goal of the experiments is to arrive at a simplified description of the system and estimate the essential physicochemical parameters with the help of a parameterized model. Most often such a model consist of a kinetic scheme containing transitions between states, which is also called compartmental model.

A.0.1 Model for the Observations

A time-resolved spectrum is a collection of measurements done at different (distinct) times and wavelengths. Two measurement sequences can be distinguished in a pump and probe experiment:

a. Measurements can be done simultaneously at a great number of wavelengths and at a certain time delay with respect to the exciting pulse. This is called a time gated spectrum. A collection of such time gated spectra at different time delays constitutes a time-resolved spectrum. With pump-probe spectroscopy, a time gated spectrum is susceptible to baseline fluctuations.

b. Alternatively, at a particular wavelength, a decay trace is measured as a function of time in respect to the exciting pulse: a collection of such decay traces measured at different wavelengths constitutes a time-resolved spectrum.

A.0.1.1 Instrumental Function

Usually the system is excited by a short laser pulse of a certain energy. The convolution of the shape of this exciting pulse and the detector response is called the *impulse response function* IRF and it limits the fastest response observable in the

experiment. In a sub-picosecond pump probe experiment, as described in the introduction of section A, the detector response can be obviously neglected and the IRF is given by the convolution of pump and probe pulses (Equation 2.12). Ideally the IRF width should be shorter than the shortest time scale under study. This is impossible when studying ultrafast phenomena and then on a (sub)picosecond time scale, the shape of the IRF as well as its timing precision become important.

A.0.1.2 Stochastics

The stochastic properties of pump-probe types of measurements are not easy to handle. The observations are assumed to contain additive normally distributed noise. In general these observations are also assumed to be statistically independent, which seems justified because the measurements are done sequentially. There is one exception: with time gated spectra a whole spectrum is observed simultaneously, and in principle the responses measured at different wavelengths could be statistically dependent with (unknown) covariance matrix Σ (independent of time).[152] With independent measurements there are several possible cases for the usually unknown variance σ^2 which may in principle depend upon time t and wavelength λ: (a) constant variance $\sigma^2(t, \lambda) = \sigma^2$ which is the most common assumption; (b) wavelength-dependent variance $\sigma^2(t, \lambda) = \sigma^2(\lambda)$ which is appropriate with difference absorption measurements. In general, $\sigma^2(\lambda)$ needs to be estimated as well. This procedure is called *iteratively reweighted least squares*.

A.0.2 Model Assumption

A.0.2.1 Homogeneity

A classical problem in describing reaction dynamics is (in)homogeneity. The common assumption is that the properties of the system under study are homogeneous, which means that a discrete set of parameters describes the whole system. The observed dynamics of the ensemble can be ascribed to the dynamics of each individual

member of that ensemble.

A.0.2.2 Separability

The spectroscopic properties of a mixture of components are a superposition of the spectroscopic properties of the components weighted by their concentration. In the case of absorption this is known as the Beer-Lambert law. Thus, the noise-free, time-resolved spectrum $\psi(t, \lambda)$ is a superposition of the contributions of the n_{comp} different components:

$$\psi(t, \lambda) = \sum_{l=1}^{n_{comp}} c_l(t)\, \varepsilon_l(\lambda) \tag{A.1}$$

where $c_l(t)$ and $\varepsilon_l(\lambda)$ denote, respectively, the concentration and spectrum of component l.

Note that according to Equation A.1, a separability of time and wavelength properties is possible. However, with ultrafast measurements there is a caveat: the properties of the detector system are in general wavelength-dependent on a (sub)picosecond time scale, thus with wavelength-dependent parameters $\theta(\lambda)$ the model for the concentration reads $c_l(t, \theta(\lambda))$. Regarding Equation A.1, we note that the quantity which will be estimated is the product $c_l \cdot \varepsilon_l$ which in itself is insufficient for the determination of the absolute values of c_l and ε_l. Thus, when we have, e.g. a kinetic model for c_l and no additional information, we can only identify the parameters which determine the shapes of c_l and ε_l.

A.0.3 Kinetics Models

In this section We will describe the schematic procedure to analyze a multi-traces set of data and the models to interpret the *molecular response function* $R(t)$ of Equation 2.13. A first distinction to be made is the order of the kinetics. In case the concentrations are described by linear differential equations, we are dealing with first order kinetics. The solution of a system of linear differential equations is given by a sum of exponential decays convolved with the IRF. When the differential

equations contain product of concentrations terms we are dealing with second order kinetics . In the following, we will restrict ourselves to first order kinetics, but many aspects of these methods are also applicable to more complex kinetics.

A.0.3.1 Global Analysis

Without "a priori" knowledge about a detailed kinetic model, the first step is the data fitting with a sufficient number of exponential decays and their amplitudes which constitute the *Decay Associated Spectra* (DAS). Note that this number can be larger than the number of spectrally different components present. Subsequently, the DAS can be fitted with a spectral model. With *difference* absorption spectroscopy (such as transient absorption technique) the amplitudes associated with exponential decays are termed *Decay Associated Difference Spectra* (DADS).

A.0.3.2 Compartmental Models

When "a priori" knowledge about a detailed kinetic model is available, a linear time-invariant compartmental model can be used. Because in contrast with global analysis, a specific kinetic model is tested, this is often termed *target analysis*. The target here is to describe the real concentrations of the components. Note that the global analysis is equivalent to a number of noninteracting, parallelly decaying compartments.

An important question is whether all unknown kinetic parameters can be estimated from the data. To answer this, a first step is of course detection of structural (un) identifiability, which is caused by incomplete information on the system. When different compartmental schemes result in the same model output, the system is structurally unidentifiable.

Transitions between compartments are described by microscopic rate constants which constitute the off diagonal elements of the transfer matrix K. The diagonal elements of K contain the total decay rates of each compartment. The concentrations of each compartment are described by a vector $c(t) = [c_1(t) \ \ldots \ c_{n_{comp}}(t)]^T$. Thus, a

linear compartmental model with n_{comp} compartments is described by a differential equation for these concentrations:

$$\frac{d}{dt}\, c(t) = K\, c(t) + j(t) \tag{A.2}$$

where the input to the system is described by a vector $j(t) = g(t)\,[1\, x_2\, \ldots\, x_{n_{comp}}]^T$, with $g(t)$ the IRF and x_l representing a possible extra input to compartment l. Equation A.2 can be solved analytically, which is important for both insight into the problem and for computational speed.

We assume that all eigenvalues of the transfer matrix K are different, and that $c(-\infty) = 0$. The solution of Equation A.2 is then given by $c(t) = g(t) \otimes e^{Kt}$ where $\otimes$ indicates convolution. We can distinguish two different cases:

1. For a diagonal K-matrix ($K = \mathrm{diag}(-k_1\,, \ldots\,, -k_{n_{comp}})$) with all inputs x_l equal to 1, the concentration matrix C consists of elements $[C_I]_{pq} = c_q^I(t_p, k_q) = g(t) \otimes exp(-k_q t_p)$. The *sub* or *super*script I indicates that this is Model I comprising independently decaying compartments, also called *parallel model*.

2. For the evaluation of the exponential of a non-diagonal K matrix and with all inputs x_l different to 1, we use the eigenvector-eigenvalue decomposition $K = U\Lambda U^{-1}$. With $K = \mathrm{diag}(-k_1\,, \ldots\,, -k_{n_{comp}})$ we have $e^{Kt} = U e^{Kt} U^{-1}$ and

$$\begin{aligned} e^{Kt} =& U\, diag\big(U^{-1}[1\, x_2\, \ldots\, x_{n_{comp}}]^T\big) \\ & \times \left[g(t) \otimes e^{-k_1 t}\, \ldots\, g(t) \otimes e^{-k_{n_{comp}} t}\right]^T \equiv A_{II}^T\, C_I^T \end{aligned} \tag{A.3}$$

Thus, the solution of the general compartmental model is a linear combination of the c_l^I and thus a transformation of C_I (derived from the eigenvalues of the transfer matrix K) for which we can write

$$C_{II} = C_I\, A_{II} \tag{A.4}$$

with $A_{II}^T = U\, diag\big(U^{-1}[1\, x_2\, \ldots\, x_{n_{comp}}]^T\big)$. Note that a compartmental model is closely related to the state space representation in mathematical systems theory, with the vector of concentrations of compartments being the state vector.

A.0.3.3 The Unbranched, Unidirectional Model

Apart from the global analysis with independent decays $(1|\,2|\,\ldots\,|\,n_{comp})$, the simplest kinetic scheme is the unbranched, unidirectional model $(1 \rightarrow 2 \rightarrow \cdots \rightarrow n_{comp})$. These models are also termed *parallel* and *sequential*, and correspond to the generalization of the models I and II of the previous section.

In the sequential model back-reactions are ignored on the assumption that the energy losses are large enough that the reverse reaction rates are negligible. Note the assumption that there are no losses in the chain $1 \rightarrow 2 \rightarrow \cdots \rightarrow n_{comp}$. The compartmental model can be solved to yield

$$c_l(t) = \sum_{j=1}^{l} b_{j,l} \exp(-k_j t) \otimes g(t) \tag{A.5}$$

where k_j is the decay rate of compartment j and the amplitudes b_{jl} of the (convolved) exponential decays are defined by $b_{11} = 1$ and for $j \leq l$:

$$b_{jl} = \prod_{m=1}^{l-1} k_m / \prod_{n=1}^{l} (k_n - k_j)_{n \neq j} \tag{A.6}$$

In particular, for $j < l$, $b_{j,l} = b_{j,l-1}\, k_{l-1}/(k_l - k_j)$. Of course, hybrids of the generalized models I and II, containing a mixture of parallelly and sequentially decaying compartments, can also easily be solved.

A.0.4 Model for the Observations in Matrix Notation

In many cases the data can be collected in a matrix Ψ of dimensions $m \times n$, where m and n are, respectively, wavelengths and the number of different time instants. The matrix element ψ_{ij} then contains the measurement at time instant t_j and wavelength λ_i. The use of matrix notation greatly simplifies the description of the model for the

observations and allows the use of matrix reduction techniques. The basic model which describes the time evolution of spectra is the following

$$\psi_{\lambda_i t_j} = \sum_{l=1}^{n_{comp}} c_{lt_j}\{\theta\}\, \varepsilon_{l\lambda_i}\{\gamma\} \tag{A.7}$$

where c_{lt_j} denotes the concentration of component l at time t_j, $\varepsilon_{l\lambda_i}$ denotes the contribution of component l at wavelength λ_i, $\{\gamma\}$ and $\{\theta\}$ are the set of parameters employed in the model for the representation of component's spectra and for the representation of the concentration's evolution. The $\varepsilon_{l\lambda_i}$ and c_{lt_j} are collated in the matrices E and C, of dimension $m \times n_{comp}$ and $n \times n_{comp}$, respectively. The columns of E are the component spectra, whereas the columns of C are the concentration profiles of the components. Hence we can write

$$\Psi = E\{\gamma\}\, C\{\theta\}^T \tag{A.8}$$

In this framework of general matrix representation of the transient two-way data, two problems come out: the estimation of the number of components and the fitting of the data matrix with a suitable model (for example a kinetic model) which means, in principle, the simultaneous adjustment of a huge number of $\{\gamma\}$ and $\{\theta\}$ model parameters.

Indeed, assuming time t as the experimental evolution variable, i.e. the two-way data are collected in the matrix Ψ as expressed before and no temperature or other parameters dependencies are considered, the general modeling problem can be expressed as a least-square interpretation of Equation A.8.

$$\Psi \approx E\{\gamma\}\, C\{\theta\}^T \tag{A.9}$$

The optimization implied by Equation A.9 will most often be taken as the minimization of a sum of un-weighted squared residuals, and the relation "$\approx$" will imply such simple least-squares optimization unless otherwise noted. Equation A.9 involves the minimization of the residual expressed by Equation A.10, in respect to some chosen set of adjustable spectral amplitudes $E_{\lambda_i l}(\gamma)$ and parameters (amplitude and/or

time constants) $\{\theta\}$ of the kinetic model.

$$\delta^2 \equiv \sum_{\lambda_i}^{n_\lambda} \sum_{t_j}^{n_t} \left[\psi_{\lambda_i t_j} - \left(\sum_{l=1}^{n_{comp}} E_{\lambda_i l}\, C^T_{l t_j} \right) \right]^2 \tag{A.10}$$

One approach is to minimize this expression directly using some appropriate multi-parameter minimization algorithm, while treating each of the unknown spectral amplitudes and model parameters as nominally independent adjustable parameters. The resulting large number of adjustable parameters and its possible impact on the performance (and even the choice) of the minimization algorithm is the principal disadvantage of this approach. On the other hand, the direct minimization of δ^2 in Eq. A.10 also retains a complete flexibility in specifying the spectroscopic features of the problem, which is often reduced or lost in more efficient or "elegant" procedures. Of course, the complete flexibility of this direct analysis may not be especially helpful for many problems, but procedures that retain some of its flexibility while eliminating the more serious of its inefficiencies are often desirable.

A.0.4.1 Singular Value Decomposition

The analysis of the modeling problem in Eq. A.10 may often be facilitated by simplifying the data matrix Ψ in some way that does not compromise its essential information content. Beyond the obvious simplifications designed merely to reduce the size of the data matrix (e.g., truncation and/or re-sampling of the data on a coarser grid of spectroscopic parameters λ) are more sophisticated rank-reduction procedures that attempt to extract minimal descriptions of the "meaningful" content of a data set. Methods based on *singular value decomposition* (SVD) have become increasingly popular in recent years.[153]

The *Singular Value Decomposition* of an arbitrary $m \times n \quad (m > n)$ matrix Ψ allows the expression of this matrix as the product

$$\Psi = U\, S\, V^T \tag{A.11}$$

where U is a $m \times n$ matrix and V is a $n \times n$ matrix. The columns of each matrix comprise orthonormal sets of vectors (i.e., $U^T U = V^T V = I$, the $n \times n$ identity matrix), and S is a $n \times n$ diagonal matrix with nonnegative diagonal elements s_i called the *singular values* of Ψ. When Ψ is a $n_\lambda \times n_p$ (where p is the *evolution variable of the experiment*, i.e t in our case) matrix of spectroscopic data arranged as matrix Ψ in Eqs. A.7 and A.8, the columns of U are themselves spectra of the same type, the normalized *basis spectra* of Ψ. The contribution of a specified basis spectrum to each of the measured spectra (columns of Ψ) is given by the elements of the corresponding row of V^T (column of V), scaled by the corresponding singular value. The s_i, along with the corresponding columns of U and V, may always be ordered so that $s_1 \geq s_2 \geq \ldots \geq s_n \geq 0$. With this ordering, the *rank* r of Ψ is the index of the last (and smallest) nonzero singular value. Moreover, for any $q \leq r$, the truncated matrices U_q and V_q (consisting, respectively, of the first q columns of U and V) and S_q (the diagonal matrix containing the q largest singular values) provide the best possible least-squares approximation of *rank* q of the matrix Ψ, $\Psi \cong \Psi_q = U_q S_q V_q^T$. The residual of this approximation is given by

$$|\Psi - \Psi_q|^2 = \sum_{i=q+1}^{r} s_i^2 \tag{A.12}$$

This last property motivates an overall strategy for the use of SVD in reducing spectroscopic data sets: By considering the distribution of singular values, a "truncated SVD" consisting of a (generally small) subset of the basis spectra and corresponding amplitude vectors is selected that represents the original data matrix within some acceptable tolerance. Additional processing of these retained vectors may be done, including linear combination and further screening based on signal-to-noise considerations. The final result is a pair of matrices U' and V' of basis spectra and vectors of amplitude-versus-experimental parameter (into which singular values have been absorbed), respectively, all of which are of acceptable quality for further analysis, such that the product $\Psi' \equiv U' V'^T$ remains close to Ψ.

Of course, any procedure that satisfactorily produces such a minimal product

representation would serve, but the SVD provides an especially convenient mathematical framework for the analysis.

A.0.4.2 Estimation of the Number of Components

When there are no linear dependencies between the component spectra, and thus no linear relationships between the columns of E, the matrix E is of *full rank*. Analogously, when there are no linear dependencies between the concentrations of the components, and thus no linear relationships between the columns of C, the matrix C is also of *full rank*. This rank is equal to the number of components. Consequently, when $rank(C) = rank(E) = n_{comp}$ and with noise-free data , we have $rank(C) = rank(EC^T) = n_{comp}$. Thus, with experimental data of which we do not know the number of components, we can estimate this number by estimating the *rank* of Ψ using the *Singular Value Decomposition* of Ψ

$$\Psi = U\,S\,V^T \tag{A.13}$$

With n_{comp} components and noise-free (Equation A.11) data we have exactly n_{comp} significant singular values: $s_1 \geq s_2 \geq \ldots \geq s_{n_{comp}} > s_{n_{comp}} + 1 = \cdots = 0$.

A.0.4.3 Projecting the Data upon Singular Vectors

Next to the use of SVD for *rank* estimation, an important application is data reduction and noise suppression. Assuming the noise is small, the Singular Value Decomposition results can be used to project the data upon the first n_{comp} singular vectors.

It must be emphasized that the matrices U' and V' described in section A.0.4.1 are still purely mathematical objects at this stage, but they provide a useful starting point for the model-based synthesis of components spectra and populations. Within this reduced representation (of *rank* q) of the data set, all measured spectra are linear combinations of the columns of U'. Moreover, a basic assumption of the modeling is that all spectra are linear combinations of the components spectra in E (Equation

A.8). Therefore, we can say that the components spectra are linear combinations of the columns of U', i.e., $E = U'\mathbb{A}$ for some matrix of coefficients $\mathbb{A}$. We then have a representation of the data matrix in the form

$$\Psi \simeq \ \Psi' = U'\,V'^{\,T} \ \approx EC^T = U'\,\mathbb{A}\,C^T \tag{A.14}$$

Therefore, within our chosen basis U' for all spectra, we can re-cast the least-squares problem in Equations A.9 and A.10 as a search for a set of model parameters $\{\theta'\}$ (time constants) and a matrix of coefficients $\mathbb{A}$ (amplitudes) such that the relation

$$V'^{\,T} \approx \mathbb{A}\,C^T\{\theta'\} \tag{A.15}$$

is optimally satisfied, thereby removing direct reference to the components spectra from the problem. The obvious advantage of the SVD-based analysis is that the matrices involved are generally much smaller: $V'^{\,T}$ is $q \times n_p$ and $\mathbb{A}$ is $q \times n'_{comp}$ (where n'_{comp} is the number of effective components), whereas Ψ and E are $n_\lambda \times n_p$ and $n_\lambda \times n'_{comp}$, respectively. In many modeling situations the consequent reduction in computational effort required may be sufficient justification for choosing this method. After the optimization of the least square problem of Equation A.15, the *Decay Associated Spectra* DAS or the *Decay Associated Difference Spectra* DADS, which in principle constitute the column of matrix E, can be obtained as $\mathbf{DADS} = U'\,\mathbb{A}$.

Appendix B

Anisotropy in Time Resolved Fluorescence and Transient Absorption experiments

In this chapter we will derive the fundamental relations that allows to extrapolate the rotational contribution from the transient absorption signal. A great part of the concepts that we'll describe derives directly from static and time resolved fluorescence theory, but can be applied also to transient absorption spectroscopy. In fluorescence anisotropy measurements (static or time-resolved), the spontaneous emission is the monitored photophysical process. In *TAS* experiments, the signal is acquired after the interaction of the probe beam's photons with the excited sample, and it is defined by the changes introduced by this interaction on the probe beam itself (see section.....experimental....). The observed photophysical processes are then (excluding vibrational relaxation and multiphoton absorption) the stimulated emission (*SE*)and the excited state absorption (*ESA*) and, from this point of view, the two experiments are very different. Nevertheless, if we consider the evolution of the excited state population we obtain the same results. The decay profile that is obtained by monitoring the intensity of the *SE* band with a *TAS* experiment is the

same as the one obtained by time resolved fluorescence experiment. This is because the pump and probe experiments allow, during the delay between pump and probe pulse, the unperturbed relaxation of the molecular system.

B.1 Introduction

Upon excitation with polarized light, the emission from many samples is also polarized. The extent of polarization of the emission is described in terms of the anisotropy (r). Samples exhibiting nonzero anisotropies are said to display polarized emission. The origin of these phenomena is based on the existence of transition moments for absorption and emission which lie along specific directions within the chromophore structure. In homogeneous solution the ground-state chromophores are all randomly oriented. When exposed to polarized light, those chromophores which have their absorption transition moments oriented along the electric vector of the incident light are preferentially excited. Hence, the excited-state population is not randomly oriented. Instead, there is a somewhat larger number of excited molecules having their transition moments oriented along the electric vector of the polarized exciting light (see section B.2.3).

Depolarization of the emission can be caused by a number of phenomena, the relative importance of which depends upon the sample under investigation. Rotational diffusion of chromophores is one common cause of depolarization. The anisotropy measurements reveal the average angular displacement of the chromophore that occurs between absorption and subsequent emission of a photon. This angular displacement is dependent upon the rate and extent of rotational diffusion during the lifetime of the excited state. These diffusive motions, depend, in turn, upon the viscosity of the solvent and the size and shape of the rotating molecule. For chromophores in solution, the rotational rate of the chromophore is dependent upon the viscous drag imposed by the solvent. As a result, a change in solvent viscosity will result in a change in fluorescence anisotropy. For small chromophores in solutions

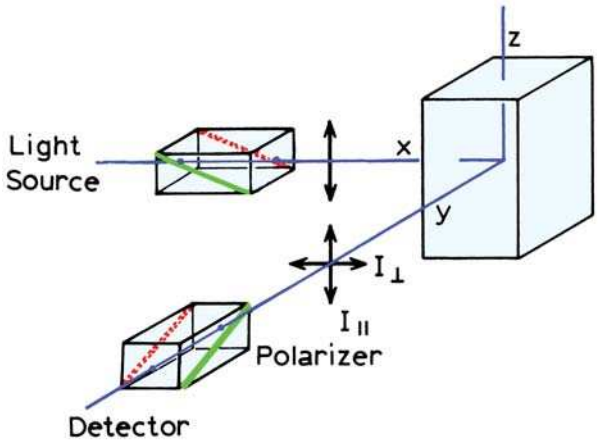

Figure B.1: Schematic diagram for measurement of fluorescence anisotropies.

of low viscosity, the rate of rotational diffusion is typically faster than the rate of emission. Under these conditions, the emission is depolarized and the anisotropy is close to zero.

This is the point of view of static anisotropy measurements; in time-resolved experiments, such as transient absorption or time resolved fluorescence with hundred femtoseconds of time resolution , the approach is opposite: we are able to reveal anisotropy changes only when the molecular rotations are faster than the excited state lifetime. This is the key point which distinguish static and time resolved measurements.

The measurement of fluorescence anisotropy is illustrated in Figure B.1. The sample is excited with vertically polarized light. The electric vector of the excitation light is oriented parallel to the vertical or z-axis. One then measures the intensity of the emission through a polarizer. When the emission polarizer is oriented parallel ($\|$) to the direction of the polarized excitation, the observed intensity is called $I_\|$. Likewise, when the polarizer is perpendicular ($\perp$) to the excitation, the intensity is called $I_\perp$. These values are used to calculate the anisotropy:

$$r = \frac{I_\| - I_\perp}{I_\| + 2I_\perp} \tag{B.1}$$

The anisotropy is a dimensionless quantity which is independent of the total intensity of the sample. This is because the difference $(I_{\parallel} - I_{\perp})$ is normalized by the total intensity, which is $I_T = I_{\parallel} + 2I_{\perp}$.

In earlier publications one frequently encounters the term polarization, which is given by

$$P = \frac{I_{\parallel} - I_{\perp}}{I_{\parallel} + I_{\perp}} \tag{B.2}$$

The polarization and anisotropy values can be interchanged using

$$P = \frac{3r}{2 + r} \tag{B.3}$$

$$r = \frac{2P}{3 - P} \tag{B.4}$$

Although there is nothing incorrect about the notion of polarization, its use should be discouraged. Anisotropy is preferred because most theoretical expressions are considerably simpler when expressed in terms of this parameter, an observation first made by Alexander Jablonski. As an example of this simplification, consider a mixture of chromophores, each with polarization P_i and a fractional fluorescence intensity f_i. The polarization of this mixture $(\overline{P})$ is given by

$$\left(\frac{1}{P} - \frac{1}{3}\right)^{-1} = \sum_i {f_i}^{-1} \left(\frac{1}{P_i} - \frac{1}{3}\right) \tag{B.5}$$

In contrast, the average anisotropy $(\overline{r})$ is given by

$$\overline{r} = \sum_i f_i r_i \tag{B.6}$$

where r_i indicate the anisotropies of the individual species. The latter expression is clearly preferable. Furthermore, following pulse excitation, the decay of fluorescence anisotropy $[r(t)]$ of a sphere is given by

$$r(t) = r_0 e^{-t/\theta} \tag{B.7}$$

where r_0 is the anisotropy at $t = 0$, and θ is the rotational correlation time of the sphere. The decay of polarization is not a single exponential, even for a spherical molecule. Suppose that the light observed through the emission polarizer is

completely polarized. Then $I_\perp = 0$, and $P = r = 1.0$. This value can be observed for scattered light from an optically dilute scatterer. Completely polarized emission is never observed for fluorescence from homogeneous unoriented samples. The measured values of P or r are smaller due to the angular dependence of photoselection (Section B.2.2). Completely polarized emission can be observed for oriented samples. Now suppose that the emission is completely depolarized. In this case, $I_\parallel = I_\perp$ and $P = r = 0$. However, it is important to note that P and r are not equal for intermediate values. For the moment, we have assumed that these intensities could be measured without artifacts due to the polarizing properties of the optical components, especially the emission monochromator.

Transient Absorption Spectroscopy *(TAS)* is a pump and probe experiment in which both pump and probe laser beams are linearly polarized. The mutual orientation between pump and probe beams is achieved by the help of a broad-band wavelength rotator. As stated before, transient signal is acquired after the interaction of the probe beam's photons with the excited sample, and it is defined by the changes introduced by this interaction on the probe beam itself. Therefore in this kind of experiment the polarization of pump and probe beams acts as selection element on the polarization of the acquired signal: they have the same function as the above mentioned polarizers.

B.2 Theory of Anisotropy

B.2.1 Origin of the Definition of the Anisotropy

Consider partially polarized light traveling along the x-axis (Figure B.2), and assume that one measures the intensities I_z and I_y with the detector and polarizer positioned on the x-axis. The polarization of this light is defined as the fraction of the light that is linearly polarized.

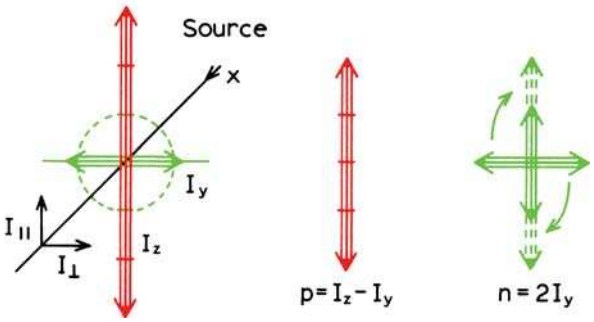

Figure B.2: Polarization of a ray of light.

Specifically,

$$P = \frac{p}{p+n} \tag{B.8}$$

where p is the intensity of the polarized component, and n is the intensity of the natural component. The intensity of the natural component is given by $n = 2I_y$. The remaining intensity is the polarized component, which is given by $p = I_z - I_y$. For vertically polarized excitation, $I_z = I_{\|}$ and $I_y = I_\perp$.

The anisotropy (r) of a light source is defined as the ratio of the polarized component to the total intensity (I_T),

$$r = \frac{I_z - I_y}{I_x + I_y + I_z} = \frac{I_z - I_y}{I_T} \tag{B.9}$$

When the excitation is polarized along the z-axis, dipolar radiation from the chromophores is also symmetric around the z-axis. Hence, $I_x = I_y$. Recalling that $I_y = I_\perp$ and $I_z = I_{\|}$, one obtains Eq. (B.1).

The polarization is an appropriate parameter for describing a light source when a light ray is directed along a particular axis. In this case, $p + n$ is the total intensity, and P is the ratio of the excess intensity along the z-axis divided by the total intensity. In contrast, the radiation emitted by a chromophore is symmetrically distributed about the z-axis.

This distribution of radiated intensity is shown in Figure B.3 for a dipole oriented along the z-axis. The intensity of the radiated light is proportional to $\cos^2\zeta$, where

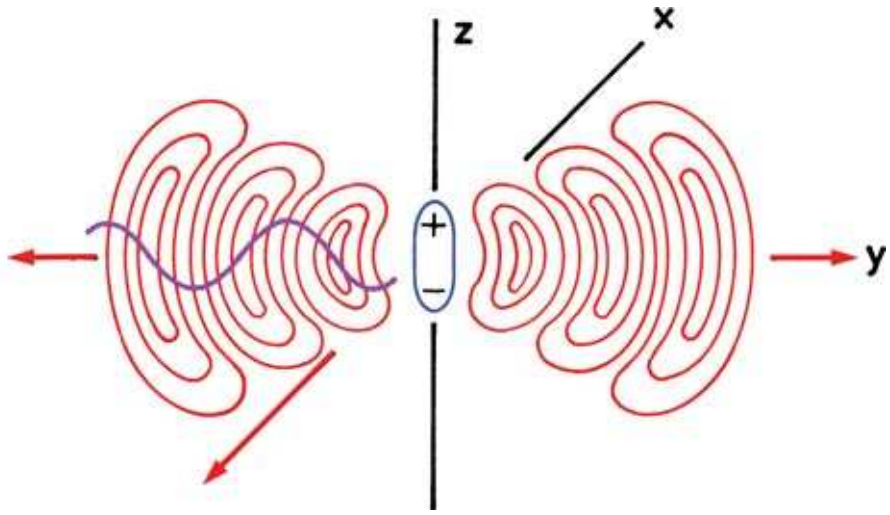

Figure B.3: Radiating dipole in a coordinate system. The dipole is oriented along the z-axis, and the intensity $I(\zeta)$ of the emission in any direction is proportional to $\cos^2\zeta$, where ζ is the angle from the $x-y$ plane. The thin arrows on the lines indicate the direction of the electric field E. The wide arrows indicate the direction of energy migration, which is symmetrical around the z-axis.

ζ is the angle above or below the $x-y$ plane. It is for this reason that, for excitation polarized along the z-axis, the total intensity is not given by $I_{\parallel}+I_{\perp}$, but rather by $I_T = I_{\parallel}+2I_{\perp}$. Hence, the anisotropy is the ratio of the excess intensity that is parallel to the z-axis to the total intensity. It is interesting to notice that a dipole oriented along the z-axis does not radiate along this axis and cannot be observed with a detector on the z-axis.

B.2.1.1 Origin of $I_T = I_{\parallel}+2I_{\perp}$

It is widely known that the total intensity is given by $I_{\parallel}+2I_{\perp}$, but the origin of this result is less widely understood. This relationship is the result of the transmission properties of polarizers, in particular, the dependence of the intensity on $\cos^2\alpha$, where α is the angle between the transition moment and the transmitting direction of the polarizer or the mutual angle between pump and probe beams in *TAS* exper-

iments. Consider a collection of chromophores, each emitting an intensity I_i. The total intensity is given by

$$I_T = \sum_{i=1}^{n} I_i \tag{B.10}$$

When the intensity is observed through a polarizer (I_p) oriented along an axis p, the intensity is given by

$$I_P = \sum_{i=1}^{n} I_i \cos^2 \alpha_{pi} \tag{B.11}$$

where α_{pi} is the angle between the direction of the ith emission dipole and the axis of the polarizer. One can choose to measure the intensity along the three Cartesian axes

$$I_x = \sum_{i=1}^{n} I_i \cos^2 \alpha_{xi} \tag{B.12}$$

$$I_y = \sum_{i=1}^{n} I_i \cos^2 \alpha_{yi} \tag{B.13}$$

$$I_z = \sum_{i=1}^{n} I_i \cos^2 \alpha_{zi} \tag{B.14}$$

where the α_{pi} are the angles between the ith dipole and the representative axis (Figure B.4).

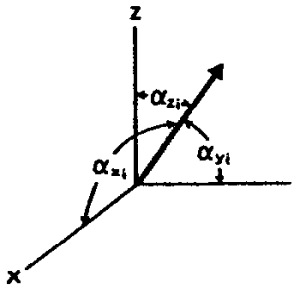

Figure B.4: Cromophore at an arbitrary orientation in the Cartesian coordinate system.

It is easy to see that

$$I_x + I_y + I_z = \sum_{i=1}^{n} I_i = I_T \tag{B.15}$$

Equation B.15 is correct because

$$\cos^2 \alpha_{xi} + \cos^2 \alpha_{yi} + \cos^2 \alpha_{zi} = 1 \tag{B.16}$$

is always true. Because $I_x = I_y$ for vertically polarized excitation, $I_T = I_\parallel + 2I_\perp$. It is interesting to note that this relationship would not be correct if the transmission of polarizers depended on some other function of α_{pi}.

B.2.2 Fundamental Equations

The theory for fluorescence anisotropy can be derived by consideration of a single molecule.

B.2.2.1 Instantaneous Anisotropy

Following an infinitely short pulse of light, the total fluorescence intensity at time t is $I(t) = I_\parallel(t) + 2I_\perp(t)$, and the instantaneous emission anisotropy at that time is

$$r(t) = \frac{I_\parallel(t) - I_\perp(t)}{I_\parallel(t) + 2I_\perp(t)} = \frac{I_\parallel(t) - I_\perp(t)}{I(t)} \tag{B.17}$$

Each polarized component evolves according to

$$I_\parallel = \frac{1}{3} I(t)[1 + 2r(t)] \tag{B.18}$$

$$I_\perp = \frac{1}{3} I(t)[1 - r(t)] \tag{B.19}$$

After recording $I_\parallel(t)$ and $I_\perp(t)$, the emission anisotropy can be calculated by means of Eq. (B.67), provided that the light pulse is very short with respect to the fluorescence decay. Otherwise, we should take into account the fact that the measured polarized components are the convolution products of the δ-pulse responses (B.64) by the instrument response.

B.2.2.2 Steady-state Anisotropy

On continuous illumination (i.e. when the incident light intensity is constant), the measured anisotropy is called steady-state anisotropy $\overline{r}$. Using the general definition

of an averaged quantity, with the total normalized fluorescence intensity as the probability law, we obtain

$$\overline{r} = \frac{\int_0^\infty I(t)r(t)\,dt}{\int_0^\infty I(t)\,dt} \tag{B.20}$$

In the case of a single exponential decay with time constant τ (excited-state lifetime), the steady-state anisotropy is given by

$$\overline{r} = \frac{1}{\tau}\int_0^\infty r(t)\exp(-t/\tau)\,dt \tag{B.21}$$

B.2.2.3 Anisotropy from emitting dipoles

Assume for the moment that the absorption and emission transition moments are parallel. This is equivalent to say that that no rearrangement of the molecular geometry between the ground and the emitting excited state is considered: we assume to work in a fixed nuclear configuration. Assume that a single molecule is oriented with angles θ relative to the z-axis and ϕ relative to the y-axis (Figure B.5). Of course, the ground-state DPH molecules will be randomly oriented in an isotropic solvent.

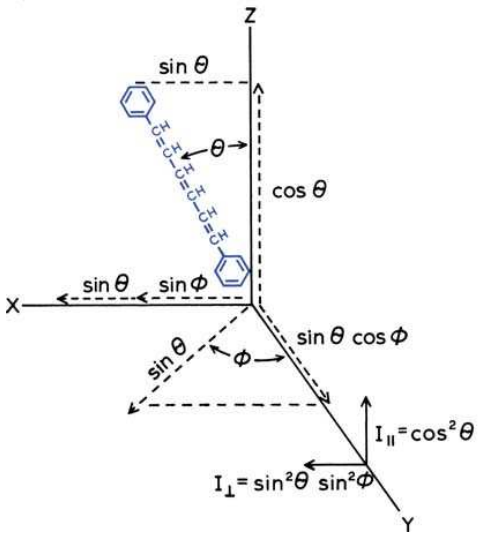

Figure B.5: Emission intensities for a single chromophore (DPH)in a coordinate system.

Our goal is to calculate the anisotropy that would be observed for this oriented molecule in the absence of rotational diffusion. The conditions of parallel dipoles, immobility, and random ground-state orientation simplify the derivation. It is known that fluorescing chromophores behave like radiating dipoles. The intensity of light radiated from a dipole is proportional to the square of its vector projected onto the axis of observation. One can also reason that the emission is polarized along the transition moment. The intensity observed through a polarizer is proportional to the square of the projection of the electric field of the radiating dipole onto the transmission axis of the polarizer. These projections are given by

$$I_{\parallel}(\theta, \phi) = \cos^2 \theta \tag{B.22}$$

$$I_{\perp}(\theta, \phi) = \sin^2 \theta \sin^2 \phi \tag{B.23}$$

In an actual experiment the solution will contain many chromophores with a random distribution. The anisotropy is calculated by performing the appropriate *ensemble average* based on excitation photoselection (section B.2.3) and how the selected molecules contribute to the measured intensity. First, consider excitation polarized along the z-axis. Such excitation must excite all molecules having an angle ϕ with respect to the y-axis with equal probability. That is, the population of excited chromophores will be symmetrically distributed around the z-axis. Any experimentally accessible population of molecules will be oriented with values of ϕ from 0 to 2π with equal probability. Hence, we can eliminate the ϕ dependence in Eq. (B.23). The average value of $\sin^2 \phi$ is given by

$$\langle \sin^2 \phi \rangle = \frac{\int_0^{2\pi} \sin^2 \phi \, d\phi}{\int_0^{2\pi} d\phi} \tag{B.24}$$

and therefore

$$I_{\parallel}(\theta) = \cos^2 \theta \tag{B.25}$$

$$I_{\perp}(\theta) = \frac{1}{2} \sin^2 \theta \tag{B.26}$$

Now assume that we are observing a collection of chromophores which are oriented relative to the z-axis with a probability $f(\theta)$. In the following section we

will consider the form $f(\theta)$ expected for excitation photoselection. The measured fluorescence intensities for this collection of molecules are

$$I_{\parallel} = \int_0^{\pi} f(\theta) \cos^2\theta \, d\theta = k \langle \cos^2\theta \rangle \tag{B.27}$$

$$I_{\perp} = \frac{1}{2} \int_0^{\pi} f(\theta) \sin^2\theta \, d\theta = \frac{k}{2} \langle \sin^2\theta \rangle \tag{B.28}$$

where $f(\theta)\, d\theta$ is the probability that a chromophore is oriented between θ and $\theta + d\theta$, and k is an instrumental constant. Using Eq. (B.23) and the identity $\sin^2\theta = 1 - \cos^2\theta$, one finds that

$$r = \frac{3 \langle \cos^2\theta \rangle - 1}{2} \tag{B.29}$$

Hence, the anisotropy is determined by the average value of $\cos^2\theta$, where θ is the angle of the emission dipole relative to the z-axis. This is because the observed intensities $I_{\parallel}$ and $I_{\perp}$ are proportional to the square of the projection of the individual transition moments onto the x- and the z-axis (FigureB.5).

It is instructive to consider the relationship between r and θ. For a single chromophore oriented along the z-axis, with collinear transitions, $\theta = 0$ and $r = 1.0$. However, it is not possible to obtain a perfectly oriented excited-state population with optical excitation of homogeneous solutions. Hence, the anisotropies are always less than 1.0. Complete loss of anisotropy is equivalent to $\theta = 54.7°$. This does not mean that each chromophore is oriented at 54.7° or has rotated through 54.7°. Rather, it means that the average value of $\cos^2\theta$ is $\frac{1}{3}$, where θ is the angular displacement between the excitation and emission moments. Recall that in the derivation of Eq. (B.29) we assumed that these dipoles were collinear. A slightly more complex expression is necessary for almost all chromophores because the transition moments are rarely collinear. In addition, we have not yet considered the effects of photoselection on the anisotropy values.

B.2.3 Excitation Photoselection and transition dipole moments

Observation of fluorescence requires excitation of the chromophores. When a sample is illuminated with polarized light, those molecules with their absorption transition moments aligned parallel to the electric vector of the polarized excitation have the highest probability of absorption. The electric dipole of a chromophore need not be precisely aligned with the z-axis to absorb light polarized along this axis. The probability of absorption is proportional to $\cos^2\theta$, where θ is the angle the absorption dipole makes with the z-axis. Indeed, the transition dipole moment and so the transition probability rate, are proportional to the square of the scalar product between the molecular electric dipole moment and the electric filed associated to the electromagnetic radiation:

$$\dot{P}(t) = 2\pi\hbar|V_{fi}|^2\rho(E_{fi}) \tag{B.30}$$

where

$$|V_{fi}| = \langle\Psi_f|\overrightarrow{\mu}\cdot\overrightarrow{E}|\Psi_i\rangle \tag{B.31}$$

and where

$$\overrightarrow{\mu_{fi}} = \langle\psi_f|\,\overrightarrow{\mu}\,|\psi_i\rangle \tag{B.32}$$

is the *transition dipole moment*. Hence, excitation with polarized light results in a population of excited chromophores that is symmetrically distributed around the z-axis (Figure B.6). This phenomenon is called photoselection. Note that the excited-state population is symmetrical around the z-axis. Most of the excited chromophores are aligned close to the z-axis, and very few chromophores have their transition moments oriented in the $x-y$ plane.

B.2.3.1 Parallel Absorption and Emission transition Moments

For the random ground-state distribution, which must exist in a disordered solution, the number of molecules at an angle between θ and $\theta + d\theta$ and ϕ and $\phi + d\phi$

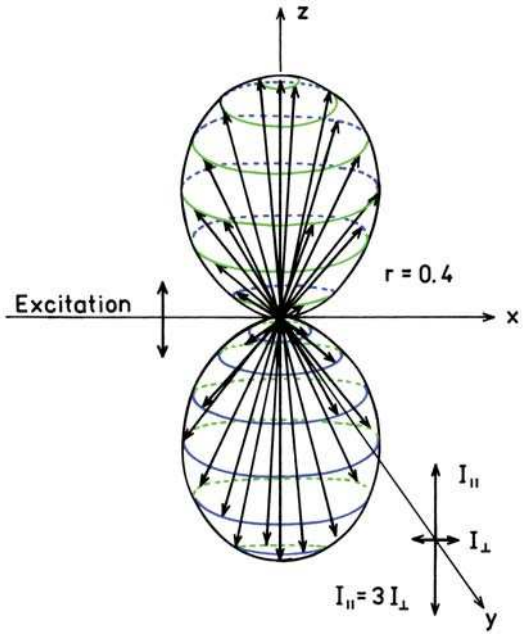

Figure B.6: Excited-state distribution for immobile chromophores with r_0=0.4.

is proportional to $2\pi \sin\theta d\theta\, d\phi$. This quantity is proportional to an elementary surface area on a sphere of unitary radius within the angles θ and $\theta + d\theta$. This is the directly consequence of the expression for an infinitesimal volume element in polar coordinate:

$$dV = r^2 \sin\theta\, dr\, d\theta\, d\phi \tag{B.33}$$

Taking into account the excitation probability, i.e. $\cos^2\theta$, the number of excited molecules whose transition moment is oriented within angles θ and $\theta + d\theta$, and ϕ and $\phi + d\phi$, is proportional to $\cos^2\theta \sin\theta\, d\theta\, d\phi$. Hence, the distribution of molecules excited by vertically polarized light is given by the fraction of molecules oriented in this direction:

$$f(\theta,\phi)\, d\theta\, d\phi = \frac{\cos^2\theta \sin\theta\, d\theta\, d\phi}{\int_0^{2\pi} d\phi \int_0^{\pi} \cos^2\theta \sin\theta\, d\theta\, d\phi} \tag{B.34}$$

obtaining

$$f(\theta,\phi)\, d\theta\, d\phi = \cos^2\theta \sin\theta\, d\theta\, d\phi \tag{B.35}$$

The probability distribution given by Eq. (B.35) determines the maximum photoselection that can be obtained using one-photon excitation of an isotropic solution. More highly oriented populations can be obtained using mul-tiphoton excitation. Recall that the anisotropy is a simple function of $\langle \cos^2 \theta \rangle$ (an *ensemble average* over all the possible values of $\cos^2 \theta$) (Eq. B.29), so calculation of $\langle \cos^2 \theta \rangle$ allows calculation of the anisotropy. For collinear absorption and emission dipoles, the maximum value of $\langle \cos^2 \theta \rangle$ is given by

$$\langle \cos^2 \theta \rangle = \int_0^{2\pi} d\phi \int_0^{\pi} \cos^2 \theta f(\theta, \phi)\, d\theta\, d\phi \tag{B.36}$$

Substitution of Eq. (B.35) into Eq. (B.36) yields $\langle \cos^2 \theta \rangle = \frac{3}{5}$. Recalling Eq. (B.29), one finds a maximum anisotropy of 0.4.

$$r_0 = \frac{3 \langle \cos^2 \theta \rangle - 1}{2} = 0.4 \tag{B.37}$$

This is the value which is observed when the absorption and emission dipoles are collinear, and when there are no processes which result in depolarization. It is called the *fundamental anisotropy*, i.e. the theoretical anisotropy in absence of any motion. Under these conditions, the excited-state population is preferentially oriented along the z-axis (Figure B.6), and the value of $I_\perp$ is one-third the value of $I_\parallel$ ($I_\parallel = 3I_\perp$). We note that this value ($r = 0.4$) is considerably smaller than that possible for a single chromophore oriented along the z-axis ($r = 1.0$) (see section B.2.2.3). In practice, rotational motions can be hindered in a rigid medium. The experimental value, called the *limiting anisotropy*, turns out to be always slightly smaller than the theoretical value. When the absorption and emission transition moments are parallel, i.e. when the molecules are excited to the first singlet state, the theoretical value of r_0 is 0.4, but the experimental value usually ranges from 0.32 to 0.39.

It is important to remember that there are other possible origins for polarized light. These include reflections and light scattered by the sample. For a dilute scattering solution, the anisotropy is close to 1.0. Scattered light can interfere with

anisotropy measurements. If the measured anisotropy for a randomly oriented sample is greater than 0.4, one can confidently infer the presence of scattered light in addition to fluorescence. The maximum anisotropy of 0.4 for collinear absorption and emission dipoles is a consequence of the $\cos^2\theta$ probability of light absorption. Anisotropy values can exceed 0.4 for multiphoton excitation.

B.2.3.2 Non-Parallel Absorption and Emission transition Moments

In the former discussion we assumed that the absorption and emission moments were collinear ($r_0 = 0.4$). Few chromophores display $r_0 = 0.4$. For most chromophores, the r_0 values are less than 0.4, and, in general, the anisotropy values depend on the excitation wavelength. This is explained in terms of the transition moments being

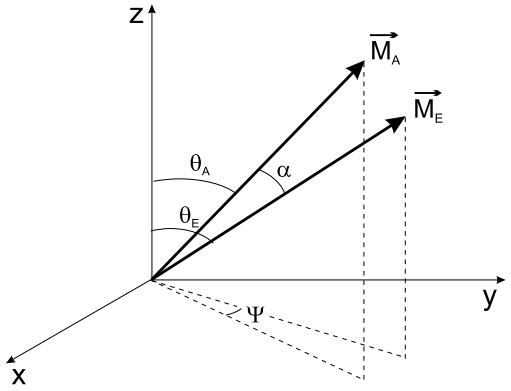

Figure B.7: Definition of angles α and ψ when the absorption and emission transition moments are not parallel.

displaced by an angle α (Figure B.7) relative to each other. In the previous section (Eqs. (B.22)-(B.29)), we demonstrated that displacement of the emission dipole by an angle θ from the z-axis resulted in a decrease in the anisotropy by a factor of $(3\cos^2\theta - 1)/2$. Similarly, the displacement of the absorption and emission dipoles by an angle α results in a further loss of anisotropy. Let α be the angle between the absorption and emission transition moments. The aim is to calculate $\cos\theta_E$ (where the subscript $_E$ means *emission*) and then to deduce r by means of Eq. (B.29).

According to the classical formula of spherical trigonometry, $\cos\theta_E$ can be written as

$$\cos\theta_E = \cos\theta_A \cos\alpha + \cos\psi \sin\theta_A \sin\alpha \tag{B.38}$$

where ψ denotes the angle between the planes $(Oz\mathbf{M}_A)$ and $(Oz\mathbf{M}_E)$ (Figure B.7). By taking the square of the two sides of Eq. (B.38) and taking into account the fact that all values of ψ are equiprobable ($\langle\cos\psi\rangle = 0$; $\langle\cos^2\psi\rangle = 1/2$), we obtain

$$\langle\cos^2\theta_E\rangle = \cos^2\alpha\langle\cos^2\theta_A\rangle + \frac{1}{2}\sin^2\alpha\langle\sin^2\theta_A\rangle \tag{B.39}$$

$$= \cos^2\alpha\langle\cos^2\theta_A\rangle + \frac{1}{2}(1-\cos^2\alpha)(1-\langle\cos^2\theta_A\rangle) \tag{B.40}$$

$$= \frac{3}{2}\cos^2\alpha\langle\cos^2\theta_A\rangle - \frac{1}{2}\langle\cos^2\theta_A\rangle - \frac{1}{2}\cos^2\alpha - \frac{1}{2} \tag{B.41}$$

Hence

$$r_0 = \frac{3\langle\cos^2\theta_E\rangle - 1}{2} = \frac{3\langle\cos^2\theta_A\rangle - 1}{2} \times \frac{3\langle\cos^2\alpha\rangle - 1}{2} \tag{B.42}$$

Because $\langle\cos^2\theta_A\rangle = 3/5$, the emission anisotropy is given by

$$r_0 = \frac{2}{5}\left(\frac{3\langle\cos^2\theta_A\rangle - 1}{2}\right) \tag{B.43}$$

Consequently, the theoretical values of r_0 range from $2/5$ $(= 0.4)$ for $\alpha = 0$ (parallel transition moments) and $-1/5$ $(= -0.2)$ for $\alpha = 90°$ (perpendicular transition moments). The observed anisotropy in a vitrified dilute solution is then the product of the loss of anisotropy due to photoselection (resulting in a reduction of the anisotropy by a factor of $\frac{2}{5}$) and that due to the angular displacement of the dipoles.

B.2.4 Magic-Angle Polarizer Conditions

This section describe the procedure of fluorescence magic-angle measurements, some of the concepts explained will be particularly useful when time resolved fluorescence and transient absorption experiments will be discussed.

The goal of intensity measurements is usually to measure a signal proportional to the total intensity (I_T), not one proportional to $I_\parallel$ or $I_\perp$. However, since the

transmission efficiency of the emission monochromators depends on polarization, the signal one observes is usually not proportional to $I_{\parallel} + 2I_{\perp}$, but rather to some other combination of $I_{\parallel}$ and $I_{\perp}$. With the use of polarizers, the measured intensity can be made proportional to the total intensity $I_T = I_{\parallel} + 2I_{\perp}$, irrespective of the degree of polarization of the sample. To accomplish this, the excitation polarizer is oriented in the vertical position and the emission polarizer is oriented 54.7° from the vertical. Since $\cos^2(54.7°)$ is 0.333 and $\sin^2(54.7°)$ is 0.667, these polarizer settings result in $I_{\perp}$ being selected twofold over $I_{\parallel}$, forming the correct sum for $I_T = I_{\parallel} + 2I_{\perp}$. The use of these magic-angle conditions is especially important for intensity decay measurements. The intensity decays of the vertically and horizontally polarized components are usually distinct. Hence, if $I_{\parallel}(t)$ and $I_{\perp}(t)$ are not properly weighted, then incorrect decay times are recovered. If the anisotropy is zero, then the correct intensity and intensity decay times are recovered independent of polarizer orientation.

B.3 Effects of Rotational Brownian motion

If excited molecules can rotate during the excited-state lifetime, the emitted fluorescence is partially (or totally) depolarized (Figure B.9). The preferred orientation of emitting molecules resulting from photoselection at time zero is indeed gradually affected as a function of time by the rotational Brownian motions. From the extent of fluorescence depolarization, we can obtain information on the molecular motions, which depend on the size and the shape of molecules, and on the fluidity of their microenvironment.

Quantitative information can be obtained only if the time-scale of rotational motions is of the order of the excited-state lifetime τ. In fact, if the motions are slow with respect to $\tau(r \approx r_0)$ or rapid $(r \approx 0)$, no information on motions can be obtained from emission anisotropy measurements because these motions occur out of the experimental time window.

A distinction should be made between free rotation and hindered rotation. In the case of free rotation, after a δ-pulse excitation the emission anisotropy decays from r_0 to 0 because the rotational motions of the molecules lead to a random orientation at long times. In the case of hindered rotations, the molecules cannot become randomly oriented at long times, and the emission anisotropy does not decay to zero but to a steady value, r (Figure B.8).

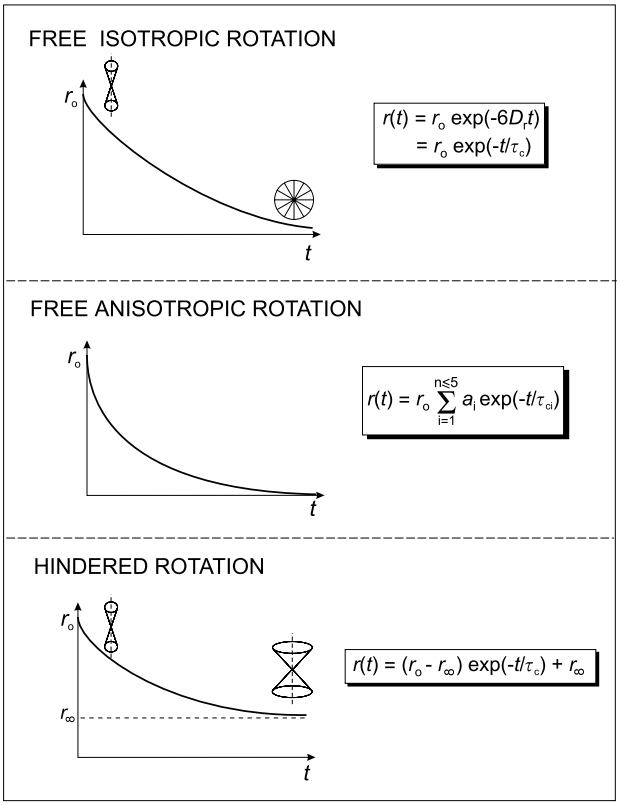

Figure B.8: Decay of emission anisotropy in the case of free and hindered rotations.

We can then anticipate that depending upon the size and shape of the chromophore, and its local environment, a wide variety of anisotropy decays are possible. A spherical molecule displays a single rotational correlation time. Anisotropy decays can be more complex if the chromophore is nonspherical, or if a spherical molecule is located in an anisotropic environment. Another origin of complex anisotropy decays

is internal flexibility of a chromophore within a larger molecule.

B.3.1 Free Rotation

The Brownian rotation of the emission transition moment is characterized by the angle $\omega(t)$ through which the molecule rotates between time zero (δ-pulse excitation) and time t, as shown in Figure B.10. Using the same method that led to Eq. (B.42), it is easy to establish the rule of multiplication of depolarization factors: when several processes inducing successive rotations of the transition moments (each being characterized by $\langle\cos^2\zeta_i\rangle$ are independent random relative azimuths, the emission anisotropy is the product of the depolarization factors $(3\langle\cos^2\zeta_i\rangle - 1)/2$:

$$r(t) = \frac{(3\langle\cos^2\theta_E\rangle - 1)}{2} = \prod_i \frac{(3\langle\cos^2\zeta_i\rangle - 1)}{2} \tag{B.44}$$

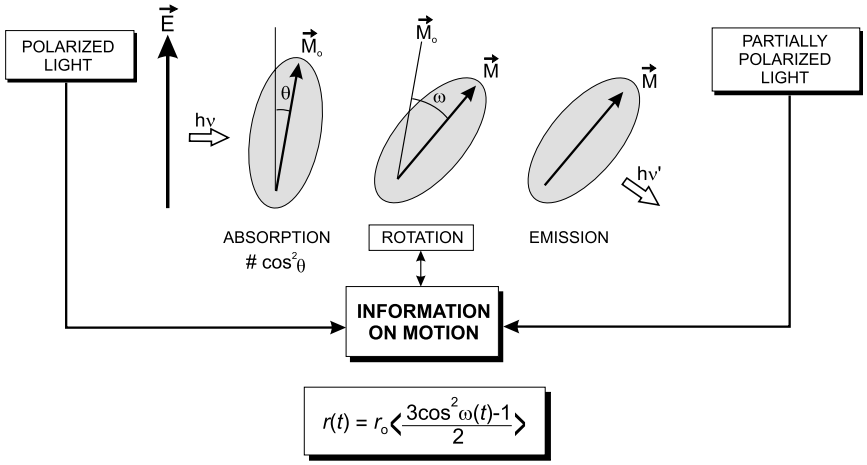

Figure B.9: Rotational motions inducing depolarization of fluorescence. The absorption and emission transition moments are assumed to be parallel.

The effect of Brownian rotation is thus simply expressed by multiplying the second member of Eq. (B.42) by $(3\langle\cos^2\omega(t)\rangle - 1)/2$:

$$r(t) = \frac{(3\langle\cos^2\theta_E\rangle - 1)}{2} = \frac{(3\langle\cos^2\theta_A\rangle - 1)}{2} \times \frac{(3\langle\cos^2\alpha\rangle - 1)}{2} \times \frac{(3\langle\cos^2\omega(t)\rangle - 1)}{2} \tag{B.45}$$

$$r(t) = r_0 \frac{(3\langle \cos^2 \omega(t) \rangle - 1)}{2} \tag{B.46}$$

The quantity $(3\langle \cos^2 \omega(t) \rangle - 1)/2$ is the *orientation autocorrelation function*: it represents the probability that a molecule having a certain orientation at time zero is oriented at ω with respect to its initial orientation. The quantity $(3x - 1)/2$ is the Legendre polynomial of order 2, $P_2(x)$, and Eq. (B.46) is sometimes written in the following form

$$r(t) = r_0 \langle P_2[\cos(\omega(t)] \rangle \tag{B.47}$$

The angled brackets $\langle\rangle$ indicate an average over all excited molecules.

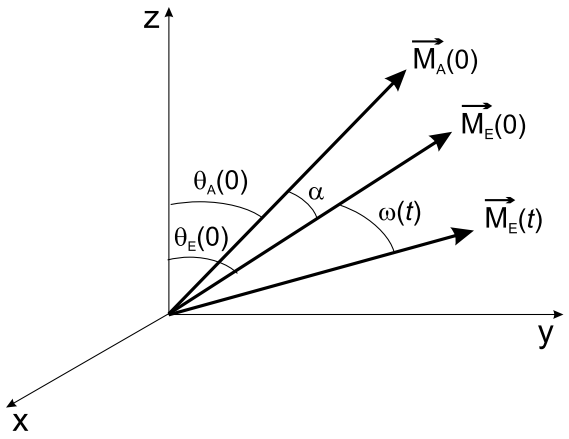

Figure B.10: Brownian rotation characterized by $\omega(t)$.

B.3.1.1 Isotropic Rotations

Let us consider first the case of spherical molecules. Their rotations are isotropic and the average of $\cos^2 \omega(t)$ can be calculated by the integral:

$$\langle \cos^2 \omega(t) \rangle = \int_0^\infty \cos^2 \omega \, f(\omega, t) \sin \omega \, d\omega \tag{B.48}$$

where $f(\omega, t)$ represents the orientation distribution function expressing the probability that a molecule has an orientation ω at time t, taking into account that $\omega = 0$ at time zero. This function must fulfill the following conditions and equations:

- initial condition: $f(0,0) = 1$
- normalization condition

$$2\pi \int_0^\pi f(\omega, t) \sin\omega \, d\omega = 1 \tag{B.49}$$

- Brownian diffusion equation for a spherical particle

$$\frac{\partial f(\omega, t)}{\partial t} = D_r \nabla^2 f(\omega, t) \tag{B.50}$$

where D_r is the rotation diffusion coefficient. In spherical coordinates, Eq. (B.50) can be rewritten as

$$\frac{\partial f}{\partial t} = D_r \frac{1}{\sin\omega} \frac{\partial}{\partial \omega} \left(\sin\omega \frac{\partial f}{\partial \omega} \right) \tag{B.51}$$

by setting $\langle \cos^2 \omega(t) \rangle = u$ the above equations lead to

$$\frac{du}{dt} = 2D_r - 6D_r u \tag{B.52}$$

Taking into account the initial condition $\cos^2 \omega(0) = 1$, the solution of this equation is

$$u = \frac{1}{3}[1 + 2\exp(-6D_r t)] \tag{B.53}$$

The autocorrelation function $(3u - 1)/2$ is then a single exponential

$$\langle P_2[\cos(\omega(t)]\rangle = \exp(-6D_r t) \tag{B.54}$$

Hence

$$r(t) = r_0 \exp(-6D_r t) \tag{B.55}$$

D_r can be determined by time-resolved fluorescence polarization measurements, either by pulse fluorometry from the recorded decays of the polarized components $I_\parallel$ and $I_\perp$, or by phase fluorometry from the variations in the phase shift between $I_\parallel$ and $I_\perp$ as a function of frequency. If the excited-state lifetime is unique and determined separately, steady-state anisotropy measurements allow us to determine D_r from the following equation, which results from Eqs (B.21) and (B.55):

$$\frac{1}{\overline{r}} = \frac{1}{r_0}(1 + 6D_r \, \tau) \tag{B.56}$$

This relationship is called *Perrin equation*, because it was established for the first time by Francis Perrin; it was written at that time with polarization ratios

$$\left(\frac{1}{p}-\frac{1}{3}\right)=\left(\frac{1}{p_0}-\frac{1}{3}\right)(1+6D_r\,\tau) \tag{B.57}$$

Once D_r is determined by fluorescence polarization measurements, the Stokes-Einstein relation can be used:

$$(6D_r)^{-1}=\frac{\eta V}{RT} \tag{B.58}$$

where V is the hydrodynamic molecular volume of the chromophore, η is the viscosity of the medium, T is the absolute temperature and R is the gas constant.

Equations (B.55) and (B.56) are often written with the rotational correlation time:

$$\tau_c=(6D_r)^{-1} \tag{B.59}$$

$$r(t)=r_0\exp(-t/\tau_c) \tag{B.60}$$

$$\frac{1}{\overline{r}}=\frac{1}{r_0}\left(1+\frac{\tau}{\tau_c}\right) \tag{B.61}$$

We have considered spherical molecules so far, but it should be noted that isotropic rotations can also be observed in the case of molecules with cylindrical symmetry and whose absorption and emission transition moments are parallel and oriented along the symmetry axis. In fact, any rotation around this axis has no effect on the fluorescence polarization. Only rotations perpendicular to this axis have an effect. A typical example is diphenylhexatriene whose transition moment is very close to the molecular axis

B.3.1.2 Anisotropic rotations

One origin of multiple correlation times is a nonspherical shape. If a molecule is not spherical, one can imagine different rotational rates around each axis. For instance, perylene is a disklike molecule, and the in-plane rotations are expected to be more rapid than the out-of-plane rotations. The out-of-plane motion requires

the displacement of solvent molecules. The in-plane rotations probably require less displacement of solvent and are thus expected to be more rapid. Such a molecule is referred to as an anisotropic rotor. Generally, macromolecules are nonsymmetric, and one expects different rotational diffusion rates about each axis.

The theory for rotational diffusion of anisotropic rotors is complex. Considerable controversy has surrounded the predicted time-resolved decays for anisotropic molecules. It is now agreed that the anisotropy is expected to decay as a sum of exponentials:

$$r(t) = \sum_{j=1}^{5} r_{0j}\, e^{-t/\tau_{cj}} \tag{B.62}$$

There may be as many as five exponential terms for an asymmetric body, but in practice only three correlation times are expected to be distinguishable. For ellipsoids of revolution, which are elongated (*prolate*) or flattened (*oblate*) molecules with two equal axes, the anisotropy decay can display only three correlation times. The values of r_{0j} and τ_{cj} are complex functions of the rates of rotation around the molecular axes of the nonsymmetric body and the orientation of the absorption and emission dipoles relative to these axes. In practice, one rarely resolves more than two exponentials, but it is important to recognize that such anisotropic rotations can result in multiexponential decays of anisotropy. For small molecules in solution, the rotational rates around the different axes are rarely different by more than a factor of 10.

B.3.2 "Stick" and "Slip" boundary Conditions

The theory described above for rotation of ellipsoids applies only to the "stick" boundary condition. The term "stick" boundary condition refers to rotational diffusion in which the first solvent layer moves with the rotating species, so that rotation is governed by the viscosity of the solvent. Macromolecules and most chromophores in polar solvents are well described by the stick diffusion. However, small molecules in non-polar solvents can often display slip rotational diffusion. As an example,

perylene in a solvent like hexane can rotate in-plane without significant displacement of solvent. When this occurs, the molecule rotates as if it were in a vacuum, and not affected by solvent viscosity. The theory of slip rotational diffusion is rather complex, and the results are often presented numerically.[105] The important point is that the possibility of slip diffusion results in a failure of the theory described above to predict the correlation times of molecules. Stated alternatively, one can recover multiple correlation times for small molecules, but these values cannot always be interpreted in terms of the correlation times predicted from the hydrodynamic theory.

B.4 Analysis of Time-Domain Anisotropy Decays

Suppose that a chromophore is excited with a pulse of vertically polarized light and that it rotates with a single correlation time. The anisotropy decay is determined by measuring the decay of the vertically ($\|$) and horizontally ($\perp$) polarized components of the emission. If the absorption and emission transition moments are collinear, the time-zero anisotropy is 0.4. In this case the initial intensity of the parallel component is threefold larger than that of the perpendicular component (Figure B.11, *left*). Assuming that the fundamental anisotropy is greater than zero ($r_0 > 0$), the vertically polarized excitation pulse results in an initial population of chromophores that is enriched in the parallel orientation. The decay of the difference between $I_{\|}(t)$ and $I_{\perp}(t)$. when properly normalized by the total intensity, is the anisotropy decay (Figure B.11, *right*).

Examination of the left panel in Figure B.11 reveals that the parallel component initially decays more rapidly than the horizontal component. This occurs because the vertically oriented chromophores are decaying by two processes, the intensity decay with decay time τ and rotation out of the vertical orientation with a correlation time τ_c. The horizontal component initially decays more slowly because it is repopulated by rotation from the excess vertically oriented population.

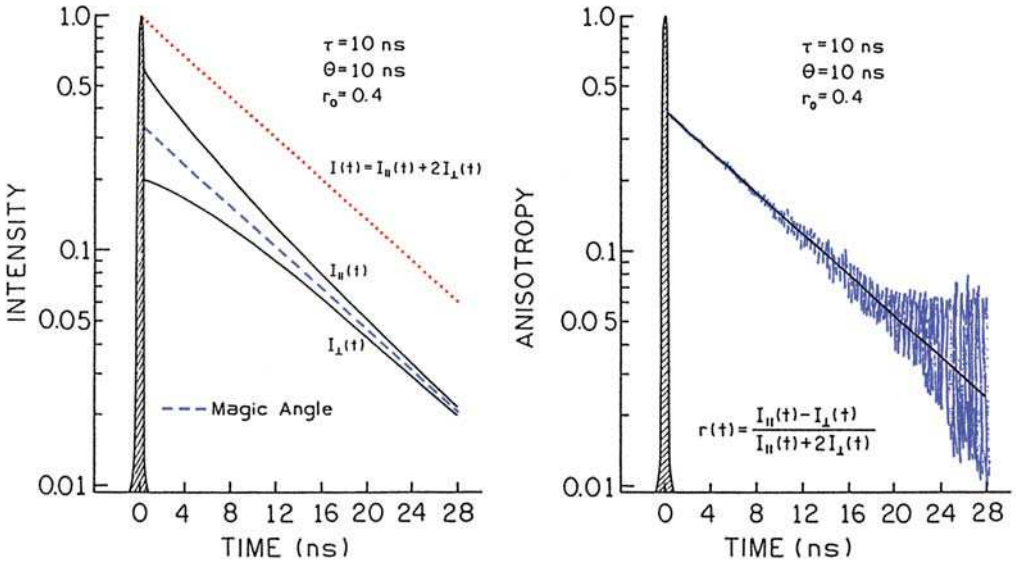

Figure B.11: Time-dependent polarized decays (*left*) and the calculated anisotropy decay (*right*).

Interpretation of anisotropy decays is best understood in terms of the individual components. The decays of the parallel ($\|$) and perpendicular ($\perp$) components of the emission are given by

$$I_{\|} = \frac{1}{3} I(t)[1 + 2r(t)] \tag{B.63}$$

$$I_{\perp} = \frac{1}{3} I(t)[1 - r(t)] \tag{B.64}$$

where $r(t)$ is the time-resolved anisotropy. Generally, $r(t)$ can be described as a multiexponential decay.

$$r(t) = r_0 \sum_j g_j \exp(-t/\tau_{cj}) = \sum_j r_{0j} \exp(-t/\tau_{cj}) \tag{B.65}$$

where $r_0 = \sum_j r_{0j}$ is the limiting anisotropy in the absence of rotational diffusion, the θ_j are the individual correlation times, and the g_j, are the associated fractional amplitudes in the anisotropy decay ($\sum g_j = 1.0$). Depending on the circumstances, r_0 may be a known parameter, perhaps from a frozen solution measurement. Alternatively, all the amplitudes (r_{0j}) can be considered to be experimental

variables. As shown in the previous chapter, the total intensity for a sample is given by $I_T = I_\parallel + 2I_\perp$. Similarly, the total (rotation-free) intensity decay is given by

$$I(t) = I_\parallel(t) + 2I_\perp(t) \tag{B.66}$$

In the time domain, one measures the time-dependent decays of the polarized components of the emission (Eqs. B.64). The polarized intensity decays are used to calculate the time-dependent anisotropy,

$$r(t) = \frac{I_\parallel(t) - I_\perp(t)}{I_\parallel(t) + 2I_\perp(t)} \tag{B.67}$$

The time-dependent anisotropy decay is then analyzed to determine which model is most consistent with the data.

B.4.1 Values of r_0

In the anisotropy decay analysis, the value of r_0 can be considered to be a known or an unknown value. If the value of in is known, the anisotropy decay law can be written as

$$r(t) = r_0 \sum_j g_j \exp(-t/\tau_{cj}) \tag{B.68}$$

where the g_j are the fractional amplitudes which decay wit the correlation times θ_j. Since $\sum g_j = 1.0$, the use of a known r_0 value reduces by one the number of variable parameters. In this type of analysis, the time-zero anisotropy is forced to be equal to r_0.

Alternatively, the total anisotropy can be a variable parameter. In this case,

$$r(t) = \sum_j r_{0j} \exp(-t/\tau_{cj}) \tag{B.69}$$

where the $r_0 j$ are the fractional anisotropies which decay with the correlation times θ_j. When using this type of analysis, we will refer to the time-zero anisotropy as $r(0)$. If the anisotropy decay contains fast components which are not resolved by the instrument, one usually finds that $\sum r_{0j} = r(0)$ is less than the fundamental anisotropy r_0.

Bibliography

[1] Feringa, B. L. *Molecular Switches*; Wiley-VCH: Weinheim, Germany, 2001.

[2] de Silva, A. P.; McClenaghan, N. D. *Chem. Eur. J.* **2004**, *10*, 574.

[3] Neuwhal, F. V. R.; Bussotti, L.; Foggi, P. *Adv. Photochem. Photobiol.* **2000**, *1*, 77.

[4] Foggi, P.; Bussotti, L.; Neuwhal, F. V. R. *Int. J. Photoenergy* **2001**, *3*, 103.

[5] Diels, J. C.; Rudolph, W. *Ultrashort Laser Pulse Phenomena*; Academic Press, 1996.

[6] Shen, Y. R. *The Principles of Nonlinear Optics*; Wiley: New York, 1984.

[7] Barcewell, R. N. *The Fouruier Transform and its Applications 3rd edition*; McGraw-Hill: Singapore, 2000.

[8] Dean, F. M. *Naturally Occurring Oxygen Ring Compounds*; Butterworths: London, 1963.

[9] Joule, J. A.; Mills, K. *Heterocyclic Chemistry,4th edition*; Blackwell Science: Oxford, UK, 2000.

[10] Barton, D. H. R.; Nakanishi, K.; Meth-Cohn, O. In *Comprehensive Natural Products Chemistry, Volume 2*; Meth-Cohn, O., Ed.; Elsevier: Oxford UK, 1999; p 677.

[11] Wheelock, C. E. *J. Am. Chem. Soc.* **1959**, *81*, 1348.

[12] Ichimura, Y. *Yakugaku-zasshi* **1960**, *80*, 771.

[13] Crosby, D. G.; Berthold, R. V. *Anal. Biochem.* **1962**, *4*, 349.

[14] Sherman, W. R.; Robins, E. *Anal. Chem* **1968**, *48*, 803.

[15] Kirkiacharian, B. S.; Ptak, M.; HÃ©lÃ¨ne, C. *C. R. Seances Acad. Sci. Ser. C* **1968**, *266*, 1548.

[16] Fink, D. W.; Koehler, W. R. *Anal. Chem.* **1970**, *42*, 990.

[17] Yakatan, G. J.; Juneau, R. J.; Schulman, S. G. *Anal. Chem.* **1972**, *44*, 1044.

[18] Mantulin, W. W.; Song, P. S. *J. Am. Chem. Soc.* **1973**, *95*, 5122.

[19] Trozzolo, A. M.; Dienes, A.; Shank, C. V. *J. Am. Chem. Soc.* **1974**, *96*, 4699.

[20] Fedorin, G. F.; Georgievskii, V. P. *Zh. Prikl. Spektrosk.* **1974**, *20*, 153.

[21] Wolfbeis, O. S.; Uray, G. *Monatsch. Chem.* **1978**, *109*, 123.

[22] Georgiyevsky, V. P. *Farm. Zh. (Kiev)* **1978**, *3*, 65.

[23] Schulman, S. G.; Rosenberg, L. S. *J. Phys. Chem.* **1979**, *83*, 447.

[24] Colombano, C. G.; Troccoli, O. E. *Anal. Chem.* **1985**, *57*, 1907.

[25] Moriya, T. *Bull. Chem. Soc. Jpn.* **1988**, *61*, 1873.

[26] Chou, P.-T.; Martinez, M. L.; Studer, S. L. *Chem. Phys. Lett.* **1992**, *188*, 49.

[27] Bardez, E.; Boutin, P.; Valeur, B. *Chem. Phys. Lett.* **1992**, *191*, 142.

[28] Heldt, J. R.; Heldt, J.; Stofi, M.; Diehl, H. A. *Spectrochimica Acta Part A* **1995**, *51*, 1549.

[29] Aaron, J. J.; Buna, M.; Parkanyi, C.; Antonious, M. S.; Tine, A. T.; ; L.Cisse, *J. Fluoresc* **1995**, *5*, 337.

[30] Hoshiyama, M.; Kubo, K.; Igarashi, T.; Sakurai, T. *J. Photechem. Phobiol. A* **2001**, *138*, 227.

[31] Kumar, S.; Rao, V.; Rastogi, R. *Spectrochimica Acta part A* **2001**, *57*, 41.

[32] Azuma, K.; Suzuki, S.; Uchiyama, S.; Kajiro, T.; Santa, T.; ; Imai, K. *Photochem. Photobiol. Sci.* **2003**, *2*, 443.

[33] Nizomov, N.; Kholov, A. U.; Ishchenko, A. A.; Ishchenko, V. V.; Khilya, V. P. *Journal of Applied Spectroscopy* **2007**, *74*, 626.

[34] de Melo, J. S.; Macanita, A. L. *Chem. Phys. Lett.* **1993**, *204*, 556.

[35] de Melo, J. S.; Fernandes, P. *J. mol. struct.* **2001**, *565-566*, 69.

[36] Mizoguchi, H.; Kubo, K.; Sakurai, T.; Inoue, H. *Ber. Bunsenges. Phys. Chem.* **1997**, *101*, 1914.

[37] Georgieva, I.; Mihaylov, T.; Bauer, G.; Trendafilova, N. *Chem. Phys.* **2004**, *300*, 119.

[38] Georgieva, I.; Trendafilova, N.; Aquino, A.; Lischka, H. *J. Phys. Chem. A* **2005**, *109*, 11860.

[39] Georgieva, I.; Trendafilova, N.; Aquino, A. J. A.; Lischka, H. *J. Phys. Chem. A* **2007**, *111*, 127.

[40] Jacquemina, D.; PerpÃ¨te, E. A.; Scalmani, G.; Frisch, M. J.; Assfeld, X.; Ciofini, I.; Adamo, C. *J. Chem. Phys* **2006**, *125*, 164324.

[41] Jacquemin, D.; PerpÃ¨te, E. A.; Assfeld, X.; Scalmani, G.; Frisch, M. J.; Adamo, C. *Chem. Phys. Lett.* **2007**, *438*, 208.

[42] Frisch, M. J. et al. *Gaussian 03, Revision C.02*; Gaussian, Inc.: Wallingford CT, 2004.

[43] Lee, C.; Yang, W.; Parr, R. *Phys. Rev. B* **1988**, *37*, 785.

[44] Becke, A. *J. Chem. Phys.* **1993**, *98*, 5648.

[45] Tomasi, J.; Mennucci, B.; Cammi, R. *Chem. Rev* **2005**, *105*, 2999.

[46] Cossi, M.; Barone, V. *J. Chem. Phys.* **2001**, *115*, 4708.

[47] Ueno, K. *Acta Cryst. C.* **1985**, *41*, 1786.

[48] Afrawal, G. P.; Baldeck, P.; Alfano, R. *Phys. Rev. A* **1989**, *40*, 5063.

[49] Kovalenko, S. A.; Dobryakov, A. L.; Ruthmann, J.; ; Ernsting, N. P. *Phys. Rev. A* **1999**, *59*, 2369.

[50] Lorenc, M.; Ziolek, M.; Naskrecki, R.; Karolczak, J.; Kubicki, J.; Maciejewski, A. *Appl. Phys. B* **2002**, *79*, 19.

[51] Remers, W. A. *The Chemistry of Antitumor Antibiotics*; Wiley: New York, 1979.

[52] Arcamone, F. *Doxorubicin Anticancer Antiboitics*; Academic Press: New York, 1982.

[53] Arcamone, F.; Penco, S. *Molecular Mechanisms of Carcinogenic and Antitumor Activity*; Adenine: New York, 1987.

[54] Lown, J. *Anthracycline and Anthracenedione-based Anticancer Agents*; Elsevier: Amsterdam, 1988.

[55] Fain, V.; Zaitsev, B.; Ryabov, M. *Russ. J. Gen. Chem.* **2004**, *10*, 1558.

[56] Huber, R.; Moser, J. E.; Grätzel, M.; Wachtveitl, J. *Chem. Phys.* **2002**, *285*, 39.

[57] Duncan, W. R.; Prezhdo, O. V. *J. Phys. Chem. B* **2005**, *109*, 365.

[58] Duncan, W. R.; Stier, W. M.; Prezhdo, O. V. *J. Am. Chem. Soc.* **2005**, *127*, 7941.

[59] Weller, A. *Z. Elektrochem* **1956**, *60*, 1144.

[60] Weller, A. *Prog. React. Kinet.* **1961**, *1*, 187.

[61] Smulevich, G.; Amirav, A.; Even, U.; ; Jortner, J. *Chem. Phys* **1982**, *73*, 1.

[62] Smulevich, G.; Angeloni, L.; Giovannardi, S.; ; Marzocchi, M. P. *Chem. Phys.* **1982**, *65*, 313.

[63] Smulevich, G. *J. Chem. Phys.* **1985**, *82*, 14.

[64] Smulevich, G.; Marzocchi, M. *Chem. Phys.* **1985**, *94*, 99.

[65] Smulevich, G.; Marzocchi, M. *Chem. Phys.* **1986**, *105*, 159.

[66] Smulevich, G.; Foggi, P.; Feis, A.; Marzocchi, M. P. *J. Chem. Phys* **1987**, *87*, 5664.

[67] Smulevich, G.; Foggi, P. *J. Chem. Phys* **1987**, *87*, 5657.

[68] Marzocchi, M. P.; Mantini, A.; Casu, M.; Smulevich, G. *J. Chem. Phys.* **1998**, *108*, 534.

[69] Carter, T. P.; Gillispie, G. D.; Connolly, M. A. *J. Phys. Chem.* **1982**, *86*, 192.

[70] Benthem, M. H. V.; Gillispie, G. D. *J. Phys. Chem.* **1984**, *88*, 2954.

[71] Gillispie, G.; Balakrishnan, N.; Vangsness, M. *Chem. Phys.* **1989**, *136*, 259.

[72] Dutta, P. K.; Lee, P. S. *J. Raman Spectrosc.* **1987**, *18*, 339.

[73] Dutta, P. K.; Lee, P. S. *J. Am. Chem. Soc.* **1988**, *19*, 175.

[74] Subbi, J. *Chem. Phys. Lett.* **1984**, *109*, 1.

[75] Madsen, F.; Terpager, I.; Olskaer, K.; ; Spanget-Larsen, J. *Chem. Phys.* **1992**, *165*, 351.

[76] Choi, J. R.; Jeoung, S. C.; Cho, D. W. *Chem. Phys. Lett.* **2004**, *385*, 384.

[77] Cho, S. H.; Huh, H.; Kim, H. M.; Kim, C. I.; Kim, N. J.; Kim, S. K. *J. Chem. Phys.* **2005**, *122*, 34304.

[78] Mahanta, S.; Singh, R. B.; Kar, S.; Guchhait, N. *Chemical Physics* **2006**, *324*, 742.

[79] Schriever, C.; Barbatti, M.; Stock, K.; Aquino, A. J.; Tunega, D.; Lochbrunner, S.; Riedle, E.; de Vivie-Riedle, R.; Lischka, H. *Chemical Physics* **2008**, *347*, 446.

[80] Scheiner, S. *J. Phys. Chem. A* **2000**, *104*, 5898.

[81] Aquino, A. J. A.; Lischka, H.; Hättig, C. *J. Phys. Chem. A* **2005**, *109*, 3201.

[82] Ortiz-Sánchez, J. M.; Gelabert, R.; Moreno, M.; Lluch, J. M. *J. Phys. Chem. A* **2006**, *110*, 4469.

[83] Catalán, J.; de Paz, J. L. G. *J. Phys. Chem. A* **2008**, *112*, 904.

[84] De, S. P.; Ash, S.; Dalai, S.; Misra, A. *Journal of Molecular Structure: THEOCHEM* **2007**, *807*, 33.

[85] De, S. P.; Ash, S.; Bar, H.; Bhui, D. K.; Dalai, S.; Misra, A. *Journal of Molecular Structure: THEOCHEM* **2007**, *824*, 8.

[86] Sobolewski, A. L.; Domckea, W. *Phys. Chem. Chem. Phys.* **1999**, *1*, 3065.

[87] Yi, P. G.; Liang, Y. H. *Chemical Physics* **2006**, *322*, 382.

[88] Arzhantsev, S.; Takeuchi, S.; Tahara, T. *Chem. Phys. Lett.* **2000**, *330*, 83.

[89] Ameer-Beg, S.; Ormson, S.; Brown, R.; Matousek, P.; Towrie, M.; Nibbering, E.; Foggi, P.; Neuwahl, F. *J. Phys. Chem. A* **2001**, *105*, 3709.

[90] Diaz, A. N. *J. Photochem. Photobiol., A* **1990**, *53*, 141.

[91] Lochbrunner, S.; Wurzer, A.; Riedle, E. *J. Chem. Phys.* **2000**, *112*, 10699.

[92] Marks, D.; Prosposito, P.; Zhang, H.; Glasbeek, M. *Chem. Phys. Lett.* **1998**, *289*, 535.

[93] Rini, M.; Kummrow, A.; Dreyer, J.; Nibbering, E.; Elsaesser, T. *Farad. Discuss* **2002**, *122*, 27.

[94] Chou, P.-T.; Chen, Y.-C.; Yu, W.-S.; Cheng, Y.-M. *Chem. Phys. Lett.* **2001**, *340*, 89.

[95] Tethwa, J.; Ouw, D.; Winkler, K.; Hartmann, N.; Vohringer, P. *Zeitschrift Fur Physikalische Chemie* **2000**, *214*, 1367.

[96] Wang, H.; Zhang, H.; Abou-Zied, O.; Yu, C.; Romesberg, F.; Glasbeek, M. *Chem. Phys. Lett* **2003**, *367*, 599.

[97] Fujino, T.; Tahara, T. *J. Phys. Chem. A* **2000**, *104*, 4203.

[98] Owrutsky, J.; Raftery, D.; Hochstrasser, R. *Ann. Rev. Phys. Chem.* **1994**, *45*, 519.

[99] Elsaesser, T.; Kaiser, W. *Ann. Rev. Phys. Chem.* **1991**, *42*, 83.

[100] Rini, M.; Dreyer, J.; Nibbering, E.; Elsaesser, T. *Chem. Phys. Lett.* **2003**, *374*, 13.

[101] Hamm, P.; Ohline, S.; Zinth, W. *J. Chem. Phys.* **1997**, *106*, 519.

[102] Mizutani, Y.; Uesugi, Y.; Kitakawa, T. *J. Chem. Phys.* **1999**, *111*, 8950.

[103] Perrin, F. *J. Phys. Radium.* **1934**, *5*, 479.

[104] Fleming, G. H. *Chemical Application of Ultrafast Spectroscopy*; Oxford University: Oxford, 1986.

[105] Hu, C.; Zwanzig, R. *J. Chem. Phys.* **1974**, *60*, 4354.

[106] Alms, G. R.; Gierke, T. D.; Patterson, T. D. *J. Chem. Phys.* **1977**, *67*, 5779.

[107] Alms, G. R.; Bauer, D. R.; Brauman, J. I.; Pecora, R. *J. Chem. Phys.* **1973**, *59*, 5310.

[108] Dote, J. L.; Kivelson, D.; Schwartz, N. *J. Phys. Chem.* **1981**, *85*, 2169.

[109] Dote, J. L.; Kivelson, D. *J. Phys. Chem.* **1983**, *87*, 3889.

[110] Ricci, M.; Torre, R.; Foggi, P.; Kamalov, V.; Righini, R. *J. Chem. Phys.* **1995**, *24*, 9357.

[111] Bartolini, P.; Ricci, M.; Torre, R.; Righini, R. *J. Chem. Phys.* **1999**, *110*, 8653.

[112] Lakowicz, J. R. *Principle of fluorescence spectroscopy. second ed.*; Kluwer Academic/Plenum Publishers: New York, 1999.

[113] Perrin, F. *J. Phys. Radium V* **1926**, *7*, 390.

[114] Perrin, F. *Ann. Phys. Ser.* **1929**, *12*, 169.

[115] J., H.; Sommer, J. H.; Henry, E. R.; Eaton., W. A. *Proc. Natl. Acad. Sci.* **1983**, *80*, 2235.

[116] Petrich, J. W.; Poyart, C.; Martin., J. L. *Biochemistry* **1988**, *27*, 4049.

[117] A., A.; Jones, C. M.; Henry, E. R.; Hofrichter, J.; Eaton., W. A. *Science.* **1992**, *256*, 1796.

[118] Lambright, D. G.; Balasubramanian, S.; Boxer., S. G. *Chem. Phys.* **1991**, *158*, 249.

[119] Franzen, S.; Kiger, L.; Poyart, C.; Martin, J.-L. *Biophysical Journal* **2001**, *80*, 2372.

[120] Wishart, J. F.; Nocera, D. *Photochemistry and Radiation Chemistry: Complementary Methods for the Study of Electron Transfer*; ACS Advances in Chemistry Series 254 American Chemical Society: : Whashington, DC, 1998.

[121] Kalyanasundaram, K.; Grätzel, M. *Coord. Chem. Rev.* **1998**, *177*, 347.

[122] Marchi, M.; Gehlen, J. N.; Chandler, D. *J. Am. Chem. Soc.* **1993**, *115*, 4178.

[123] Connolly, J. S.; Bolton, J. R. In *Photoinduced Electron Transfer*; Fox, M. A., Channon, M., Eds.; Elsevier: Amsterdam, 1988; Chapter D, p 303.

[124] Regan, B. O.; Grätzel, M. *Nature.* **1991**, *353*, 738.

[125] McCusker, J. K. *Acc. Chem. Res.* **2003**, *36*, 876.

[126] Argazzi, R.; Yha, N. H. M.; Zabri, H.; Odobel, F.; Bignozzi, C. A. *Coord. Chem. Rev.* **2004**, *248*, 1999.

[127] Marcus, R. A.; Sutin, N. *Biochim. Biophys. Acta. (Reviews on Bioenergetics)* **1985**, *811*, 265.

[128] Caneschi, A.; Dei, A. *Angew. Chem. Int. Ed.* **1998**, *37*, 3005.

[129] Dei, A. *Inorg. Chem.* **1993**, *32*, 5730.

[130] Sato, O.; Tao, J.; Zhang, Y.-Z. *Angew. Chem. Int. Ed.* **2007**, *46*, 2152.

[131] Sato, O.; Cui, A.; Matsuda, R.; Tao, J.; Hayami, S. *Acc. Chem. Res.* **2007**, *40*, 361.

[132] Dei, A.; Gatteschi, D.; Sangregorio, C.; Sorace, L. *Acc. Chem. Res.* **2004**, *37*, 827.

[133] Evangelio, E.; Ruiz-Molina, D. *J. Inorg. Chem.* **2005**, *15*, 2945.

[134] Hendrickson, D. N.; Pierpont, C. G. *Top. Curr. Chem.* **2004**, *234*, 63.

[135] Pierpont, C. G. *Coord. Chem. Rev.* **2001**, *219*, 99.

[136] Gütlich, P.; Dei, A. *Angew. Chem. Int. Ed.* **1997**, *36*, 2734.

[137] Neuwahl, F. V. R.; Righini, R.; Dei, A. *Chem Phys. Lett.* **2002**, *352*, 408.

[138] Gentili, P. L.; Bussotti, L.; Righini, R.; Beni, A.; Bogani, L.; Dei, A. *Chem. Phys.* **2005**, *314*, 9.

[139] Bencini, A.; Caneschi, A.; Carbonera, C.; Dei, A.; Gatteschi, D.; Righini, R.; Sangregorio, C.; Slageren, J. V. *Journal of Molecular Structure* **2003**, *656*, 141.

[140] Beni, A.; Carbonera, C.; Dei, A.; LÃ©tard, J.-F.; Righini, R.; Sangregorio, C.; Sorace, L. *J. Braz. Chem. Soc.* **2006**, *17*, 1522.

[141] Brady, C.; McGarvey, J. J.; McCusker, J. K.; Toflund, H.; Hendrickson, D. N. *Topic. Curr. Chem.* **2004**, *235*, 1.

[142] Hauser, A. *Topic. Curr. Chem.* **2004**, *235*, 155.

[143] Monat, J. E.; McCusker, J. K. *J. Am. Chem. Soc.* **2000**, *122*, 4092.

[144] Cannizzo, A.; Mourik, F. V.; Gawelda, W.; Zgrablic, G.; Bressler, C.; Chergui, M. *Angew. Chem. Int. Ed.* **2006**, *45*, 3174.

[145] Gawelda, W.; Cannizzo, A.; Pham, V.; Mourik, F. V.; Bressler, C.; Chergui, M. *J. Am. Chem. Soc.* **2007**, *129*, 8199.

[146] Beechem, J.; Ameloot, M.; Brand, L. *Anal. Instrum.* **1985**, *14*, 379.

[147] Beechem, J. *Chem. Phys. Lipids* **1989**, *50*, 237.

[148] Beechem, J. *Methods Enzymol.* **1992**, *210*, 37.

[149] Ameloot, M.; Boens, N.; Andriesen, R.; van den Bergh, V.; de Schryver, F. *Methods Enzymol.* **1992**, *210*, 314.

[150] Holzwarth, A. In *Biophysical Techniques in Photosynthesis*; Amesz, J., Hoff, A., Eds.; Kluwer Academic Publishing: Dordrecht, the Netherlands,, 1996; Chapter Data analysis of time-resolved measurements, pp 75–92.

[151] Dioumaev, A. *Biophys. Chem.* **1997**, *67*, 1.

[152] van Stokkum, I.; Brouwer, A.; van Ramesdonk, H.; Scherer, T. *Proc. K. Ned. Akad. v. Wet.* **1993**, *96*, 43.

[153] Henry, E. R. *Biophysical Journal* **1997**, *72*, 652.